

# The Structure of Two-Dimensional Vitreous Silica



Dissertation  
eingereicht im Fachbereich Physik  
der Freien Universität Berlin

**Leonid Lichtenstein**

geboren am 21. Januar 1985 in Ekaterinburg

Berlin, Oktober 2012

angefertigt am Fritz-Haber-Institut

Diese Dissertation wurde von November 2009 bis Oktober 2012 in der Abteilung Chemische Physik am Fritz-Haber-Institut der Max-Planck-Gesellschaft unter der Anleitung von Herrn Professor Dr. Hans-Joachim Freund angefertigt.

Gutachter:

1. Prof. Dr. Hans-Joachim Freund, Fritz-Haber-Institut, MPG
2. Prof. Dr. Paul Fumagalli, Freie Universität Berlin

Datum der mündlichen Prüfung: 26. November 2012

**Für meine Familie.**



# Abstract

Glasses are ubiquitous in nature and technology. They are generally classified by a lack of periodicity and order. Therefore, it is a great challenge to investigate the atomic arrangement in a glass. Silica is the prototype glass network former. The corner-sharing interconnection of the tetrahedral building units provides high flexibility in its atomic configuration. Silica glass, also known as vitreous silica, has been studied by various techniques for more than 80 years. However, most methods fail to give a direct view on the atomic arrangement in glass. Scanning probe methods possess the potential to resolve atomic surface structures in real space. To study glasses by these methods, a new class of two-dimensional glassy structures had to be designed.

In this work, we address a metal-supported silica bilayer at the atomic level. A combination of low energy electron diffraction, Auger electron spectroscopy, low temperature scanning tunneling microscopy and noncontact atomic force microscopy was applied in ultrahigh vacuum. The growth mode of the thin silica films was characterized. Local measurements revealed crystalline and vitreous regions in the silica bilayer film. We analyzed high resolution images of the vitreous bilayer at different ranges of order yielding a better understanding of vitreous structures in general. In addition, the atomic arrangement in crystalline and vitreous bilayer areas was resolved and thoroughly compared to each other. Ultimately, we unraveled the crystalline–vitreous interface in the two-dimensional silica film. The presented results show that the vitreous silica bilayer qualifies for a versatile glass model system.

**Keywords:** STM, AFM, silica, glass, 2D random network



# Zusammenfassung

Gläser sind allgegenwärtig in Natur und Technik. Sie werden im Allgemeinen durch fehlende Periodizität und Ordnung beschrieben. Deswegen ist es eine große Herausforderung, die atomare Struktur von Glas zu untersuchen. Silika ist das Musterbeispiel eines Glasnetzwerkbildners. Die eckenverknüpfte Verbindung der tetraedrischen Baueinheiten sorgt für eine hohe Flexibilität der atomaren Konfiguration. Seit über 80 Jahren wurde Silikaglas mittels verschiedener Techniken untersucht. Die meisten Methoden sind nicht im Stande einen direkten Einblick in die atomare Anordnung in Gläsern zu gewähren. Rastersondenmethoden besitzen das Potential, die atomare Oberflächenstruktur im Realraum aufzulösen. Um Gläser mit diesen Methoden untersuchen zu können, musste eine neue Klasse an zweidimensionalen glasartigen Strukturen entwickelt werden.

Die vorliegende Arbeit behandelt eine auf einem Metallsubstrat präparierte Silikadoppellage auf der atomaren Ebene. Eine Kombination aus niederenergetischer Elektronenbeugung, Auger-Elektronenspektroskopie, Tieftemperaturrastertunnel- und -rasterkraftmikroskopie wurde im Ultrahochvakuum angewandt. Das Wachstum der dünnen Silikafilme wurde charakterisiert. Lokale Messungen zeigen, dass es kristalline und glasartige Bereiche in der Silikadoppellage gibt. Hochaufgelöste Aufnahmen der glasartigen Doppellage wurden auf unterschiedlichen Längenskalen ausgewertet und führten zu einem besseren Verständnis von amorphen Strukturen im Allgemeinen. Zusätzlich wurde die atomare Anordnung des kristallinen und glasartigen Silikafilms aufgelöst und miteinander verglichen. Schlussendlich wurde die Grenzfläche zwischen der kristallinen und glasartigen Silikadoppellage entschlüsselt. Die vorgestellten Ergebnisse zeigen, dass sich die Silikadoppellage als vielfältiges Modellsystem für Gläser eignet.

**Schlagwörter:** STM, AFM, Silika, Glas, 2D Netzwerk





# Contents

Abstract . . . . .	v
Zusammenfassung . . . . .	vii
Contents . . . . .	ix
List of Figures . . . . .	xi
List of Tables . . . . .	xiii
List of Acronyms . . . . .	xv
<b>Introduction</b>	<b>1</b>
<b>1 The Structure of Glass</b>	<b>3</b>
1.1 Definition of “Glass” . . . . .	3
1.2 Continuous Random Network . . . . .	5
1.3 Pair Correlation Function . . . . .	7
1.4 Ranges of Order . . . . .	9
1.5 Methods for Glass Studies . . . . .	11
1.5.1 Experimental Methods . . . . .	11
1.5.2 Theoretical Methods . . . . .	13
<b>2 Methods and Experimental Implementation</b>	<b>15</b>
2.1 Low Energy Electron Diffraction . . . . .	15
2.2 Auger Electron Spectroscopy . . . . .	17
2.3 Tuning Fork Microscope . . . . .	18
2.3.1 Low Temperature Ultrahigh Vacuum Setup . . . . .	18
2.3.2 Tuning Fork Sensor . . . . .	19
2.3.3 Imaging Modes . . . . .	23
<b>3 Precharacterization of Thin Silica Films on Ru(0001)</b>	<b>25</b>
3.1 Preparation Procedure . . . . .	25
3.2 Growth Study . . . . .	29
3.3 Summary . . . . .	37

---

<b>4</b>	<b>The Atomic Structure of a Thin Vitreous Silica Film</b>	<b>39</b>
4.1	Assignment of Atomic Positions . . . . .	39
4.2	Range I: The Structural Unit . . . . .	41
4.3	Range II: Interconnection of Adjacent Structural Units . . . . .	43
4.4	Range III: Network Topology . . . . .	46
4.4.1	Pair Correlation Function . . . . .	46
4.4.2	Ring Size Distribution . . . . .	48
4.4.3	Si–Si–Si Angle Distribution . . . . .	51
4.4.4	Fourier Transformation . . . . .	51
4.5	Range IV: Longer Range Density Fluctuations . . . . .	53
4.6	Summary . . . . .	54
<b>5</b>	<b>Comparison of Crystalline and Vitreous Phases</b>	<b>57</b>
5.1	Atomic Structure . . . . .	57
5.2	Directed Distance Orientations . . . . .	59
5.3	Distances and Angles . . . . .	62
5.4	Pair Distance Histograms . . . . .	65
5.5	Summary . . . . .	66
<b>6</b>	<b>Crystalline–Vitreous Interface in Two-Dimensional Silica</b>	<b>67</b>
6.1	Motivation . . . . .	67
6.2	Atomic Structure . . . . .	68
6.3	Atomic Distances and 2D Mass Density . . . . .	70
6.4	Directed Distance Orientations . . . . .	72
6.5	Ring Size Distribution and Crystallinity . . . . .	73
6.6	Summary . . . . .	76
	<b>Conclusion and Outlook</b>	<b>77</b>
	<b>A Supporting Information for Chapter 5</b>	<b>79</b>
	<b>Bibliography</b>	<b>85</b>
	<b>Résumé</b>	<b>105</b>
	<b>List of Publications</b>	<b>107</b>
	<b>Danksagung</b>	<b>109</b>
	<b>Selbständigkeitserklärung</b>	<b>111</b>

# List of Figures

1.1	Phase diagram of two different cooling paths along which a liquid can solidify. . . . .	4
1.2	Zachariasen's schematics of the atomic arrangement in a crystal and in a glass. . . . .	6
1.3	Schematic illustration of the pair correlation function. . . . .	7
1.4	Correlation between atomic positions and the pair correlation function. . . . .	8
1.5	Ranges of order in network solids as proposed by Wright. . . . .	10
1.6	Schematic representation of a diffraction experiment. . . . .	11
1.7	X-ray diffraction patterns of crystalline and vitreous silica forms. . . . .	12
2.1	Low energy electron diffraction. . . . .	16
2.2	Auger Electron Spectroscopy. . . . .	17
2.3	Schematic overview of the low temperature ultrahigh vacuum setup. . . . .	19
2.4	Schematic of the tuning fork sensor head. . . . .	20
2.5	Schematic graphs demonstrating the dependences of the two interaction signals. . . . .	21
2.6	Overview of the different operation modes of the tuning fork microscope. . . . .	23
3.1	The Ru substrate and its O overlayer. . . . .	27
3.2	AES spectra of different preparations. . . . .	28
3.3	Growth of silica films on Ru(0001). . . . .	30
3.4	Low coverages of silica on Ru. . . . .	31
3.5	Apparent height of silica patches. . . . .	33
3.6	High coverages of silica on Ru. . . . .	36
4.1	Assignment of atomic positions. . . . .	40
4.2	Structural elements of the vitreous silica bilayer. . . . .	41
4.3	Characterization of range I order in the vitreous silica film. . . . .	42

---

4.4	Characterization of range II order in the vitreous silica film. . .	44
4.5	Comparison of Si–O–Si angles in 2D and 3D vitreous networks.	45
4.6	Evaluation of pair distances in the experimental atomic model.	46
4.7	Comparison of pair correlation functions. . . . .	47
4.8	The ring size distribution in 2D vitreous silica. . . . .	49
4.9	Log-normal plots of ring size distributions from different studies.	50
4.10	Histograms of Si–Si–Si angles. . . . .	52
4.11	Fourier analysis of an STM image of vitreous silica. . . . .	53
4.12	Analysis of the silica film’s 2D mass density. . . . .	54
5.1	Atomic structure of crystalline and vitreous regions. . . . .	58
5.2	Analysis of the O–O directed distance orientations. . . . .	60
5.3	PDHs of crystalline and vitreous phases of the silica film. . . .	65
6.1	Atomically resolved STM image of the crystalline–vitreous in- terface in the silica film. . . . .	69
6.2	Evaluation of the Si–Si distances and the two-dimensional mass density. . . . .	71
6.3	Evaluation of Si–Si nearest neighbor directed distance orien- tations. . . . .	72
6.4	Analysis of the rings at the crystalline–vitreous interface of the silica film. . . . .	74
A.1	Characterization of the error of manual evaluation of atomic positions and its influence on DDOs. . . . .	80
A.2	Characterization of the error of manual evaluation of atomic positions and its influence on the pair distance histogram. . . .	81
A.3	Evaluation of O–O nearest neighbor orientations from different images. . . . .	82
A.4	Pair distance histogram of Shackelford’s extended 2D Zachari- asen scheme. . . . .	82

# List of Tables

3.1	The preparation steps of thin silica films on Ru(0001). . . . .	26
5.1	Overview of characteristic distances determining structural order of range I, II and III. . . . .	63



# List of Acronyms

1D	one-dimensional
2D	two-dimensional
3D	three-dimensional
AES	Auger electron spectroscopy
AFM	atomic force microscopy
AT	annealing temperature
DDO	directed distance orientation
DFT	density functional theory
FFT	fast Fourier transformation
FM-DFM	frequency modulation dynamic force microscopy
LCPD	local contact potential difference
LDOS	local density of states
LEED	low energy electron diffraction
MD	molecular dynamics
MLs	monolayers
nc-AFM	noncontact atomic force microscopy
ND	neutron diffraction
NN	nearest neighbor
PCF	pair correlation function
PDH	pair distance histogram

PVD	physical vapor deposition
RMC	reverse Monte Carlo
SD	standard deviation
SPM	scanning probe microscopy
STM	scanning tunneling microscopy
TFM	tuning fork microscope
UHV	ultrahigh vacuum
XRD	X-ray diffraction



# Introduction

Over the past few decades, the technological importance of glass has been constantly increasing. Properties like optical transparency, mechanical durability and thermal stability make it a very versatile material which has an enormous number of applications. Although glasses have been produced for several thousand years, it is surprising how little we know about amorphous materials at the atomic scale. Richard Zallen, a renowned glass scientist, once declared [1]: “The atomic structure of an amorphous solid is one of its key mysteries, and structural information must be won with great effort.” The presented thesis aims to tackle the puzzling nature of glasses by investigating two-dimensional vitreous silica at the atomic level.

Exactly one century ago, Max von Laue’s discovery of X-ray diffraction (XRD) ushered in a new era in the structural analysis of condensed matter. For the first time, information on the atomic arrangement in materials could be gained. However, XRD measurements are not limited to crystals. Soon, scientists started to investigate glasses using XRD (see, e.g., Ref. [2]). The absence of sharp diffraction peaks led to the conclusion that glasses are noncrystalline—i.e. amorphous—materials. Nevertheless, a comprehensive picture of the glass structure was absent, until William H. Zachariasen published his postulates on “The Atomic Arrangement in Glass” in 1932 [3]. These ideas were able to explain XRD experiments [4] and his hypothesis is commonly referred to as the “random network theory”. A tremendous amount of work has been invested in measuring the exact atomic structure of glasses by diffraction methods [5, 6]. Although these techniques are able to yield very high resolution data, they average over a large sample area and initially probe the reciprocal space. To study noncrystalline materials in more detail, it is necessary to resolve their atomic structure in real space.

The invention of scanning tunneling microscopy (STM) [7, 8] and atomic force microscopy (AFM) [9] opened up another era in materials research. These techniques allowed atomic scale investigations and were successfully applied to a large variety of crystalline surfaces. Many surface structures and reconstructions had been known before the rise of scanning probe microscopy

(SPM). The strength of SPM lies in its high local resolution in real space, enabling the investigation of single adsorbates, molecules, and defects on the surface. Is it possible to resolve the local atomic structure of an amorphous system? The application of SPM to cleaved glass surfaces [10–15] and to glassy metals [16] has been shown. However, a detailed and unambiguous atomistic assignment of the observed structures was not possible because of rough surfaces and large corrugations. Therefore, to investigate the atomic structure of amorphous materials by SPM, an atomically flat glass is required.

Silica is the prototype network former and the basis of many glasses. It is relevant in various branches of modern technologies, e.g., in semiconductor devices, optical fibers and as a support in industrial catalysts.

Crystalline monolayer silica films on Mo(112) have been investigated in the Chemical Physics department of the Fritz-Haber-Institute for over a decade [17]. Structural [18], electronic [19, 20], vibrational [21] and adsorption properties [22–26] of these films were studied. To mimic bulk silica materials, scientists attempted to grow thicker silica films on Mo(112). The atomic structure of these films could not be resolved due to three-dimensional growth of silica clusters on the surface [27]. Therefore, we prepared silica films on a different metal support—Ru(0001). We explored the atomic structure of these films by applying a combination of STM and AFM at low temperatures in ultrahigh vacuum. We found that, depending on the preparation parameters, a silica bilayer could be grown exhibiting crystalline and vitreous regions [28–34]. For the first time, it was possible to study a vitreous material in real space at the atomic scale. Shortly after our discovery, a similar silica bilayer film was observed on graphene by scanning transmission electron microscopy [35] and on Pt(111) by STM [36]. These findings prove the existence of a new class of materials: two-dimensional glasses.

This work is outlined as follows. In chapter 1, basic concepts about the structure of glasses are described. Chapter 2 focuses on the experimental techniques used in this work. In chapter 3, results from a growth study of silica on Ru(0001) are presented. Chapters 4, 5 and 6 address the atomic structure of the silica bilayer films. The atomic arrangement in the vitreous silica bilayer is thoroughly evaluated in chapter 4. Chapter 5 compares atomically resolved crystalline and vitreous regions of the film. In chapter 6, the crystalline–vitreous interface is examined. Finally, the work is summarized and an outlook on future research is given.

# Chapter 1

## The Structure of Glass

In this chapter, basic concepts about the properties of glasses are presented. First, the term “glass” is defined. In the second section, we introduce the continuous random network as postulated by Zachariassen followed by the concept of the pair correlation function. Afterwards, Wright’s classification of order in random networks is explained. In the end, methods are listed that have been used to investigate the structure of glasses.

### 1.1 Definition of “Glass”

A glass can be defined either in terms of its thermodynamic history or its atomic structure. Figure 1.1 helps us describe the first definition. The graph shows a typical volume ( $V$ ) vs. temperature ( $T$ ) diagram of a liquid’s cooling process. In general, a liquid may take two different routes to solidify (denoted 1 and 2 in the  $V(T)$  plot). As soon as the temperature of the liquid is lowered to the freezing point  $T_f$ , it may take route 1 to the solid state and crystallize. However, this process requires time. During this so-called nucleation process, crystalline centers must form and grow. If the liquid is cooled fast enough, it may proceed according to route 2 below  $T_f$ . Between  $T_f$  and the glass transition temperature  $T_g$ , the liquid is referred to as undercooled or supercooled liquid. It is, however, still in the liquid state. If the temperature is further lowered below  $T_g$ , and there is no time for the crystallization process to occur, the supercooled liquid solidifies as a glass. The glass transition is accompanied by a characteristic change of slope in the  $V(T)$  diagram, after which the curves for the glassy state and for the crystalline state run almost in parallel. The  $T_g$  value strongly depends on the composition of the liquid and the cooling rate (for silica,  $T_g$  is approximately 1470 K [37, 38]). For a fast cooling procedure,  $T_g$  is higher than for a slow

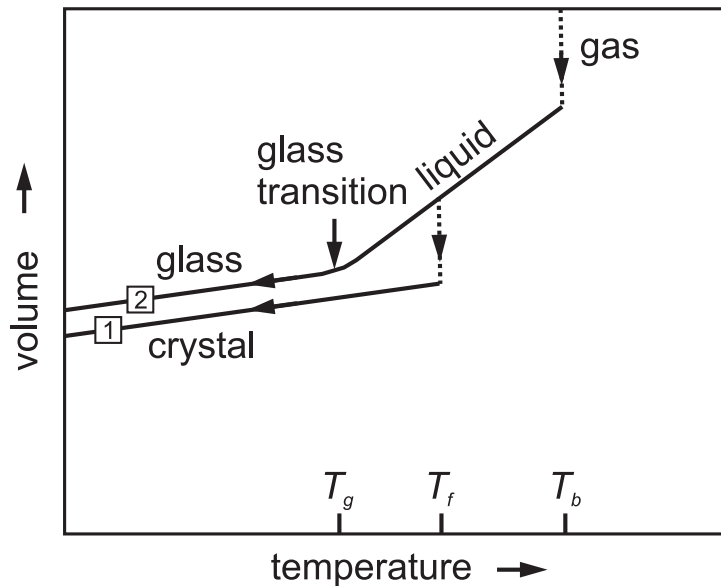


**Figure 1.1:** Phase diagram showing two different cooling paths along which a liquid can solidify. Route 1 shows the way to the crystalline state. Route 2 represents the rapid-quench path to the glassy state.  $T_g$ ,  $T_f$ , and  $T_b$  denote the temperatures of the glass transition, the freezing point and the boiling point, respectively. This figure has been retraced from Ref. [1].

process [39]. Below  $T_g$ , the glass is solid and has brittle-elastic mechanical properties. In summary, thermodynamically, a glass is a material that forms from a liquid that bypasses crystallization by a fast cooling process.

The transition from a liquid to a crystal is a first order phase transition, because the volume, which is the first derivative of the thermodynamic Gibbs function with respect to pressure, changes discontinuously, as it can be schematically seen in Figure 1.1. However, the volume changes continuously from a liquid to a glass. Thus, the glass transition is not a first order phase transition. Its behavior comes very close to a second order phase transition [40], because the specific heat changes its slope when going from liquid to glassy state. This change is, however, not very sharp, as required for a real phase transition. Therefore, the true nature of the glass transition is still debated [1, 41].

The second definition of glass involves its atomic structure. A glass is a material that lacks periodicity and long range order in its atomic arrangement. It has no sharp diffraction pattern (see also section 1.5) and its unit cell is infinitely large. In that sense, a glass is structurally very similar to a liquid, which has a random arrangement of atoms or molecules. It could

even be shown that the liquid and the glassy phase of a silica droplet have nearly the same pair correlation functions [42] (see also section 1.3).

Glasses and quasicrystals have related structural properties. Both material classes share the absence of periodicity; it is impossible to describe these structures with any Bravais lattice. However, a quasicrystal exhibits long range translational and orientational order and therefore produces a sharp diffraction pattern [43]. The first quasicrystal that was reported revealed a sharp fivefold diffraction pattern and could be assigned to the icosahedral point symmetry group [44].

Whereas metallic glasses are usually described in terms of random close packing of hard spheres [45], covalent glasses, such as vitreous silica, are explained in terms of the continuous random network as proposed by Zachariasen (see following section).

Glasses can be formed from a large number materials. The majority of engineering plastics is amorphous [41]. Even metals can be prepared in the amorphous state at very high cooling speeds [46, 47]. There are, however, certain materials that are well-suited for the glass transformation, as they condense into the vitreous state even at slow cooling rates. These materials are called glass formers and consist of oxide systems based on Si, B, P, Ge and As [48]. In their crystalline forms, glass formers are typically arranged from periodic ring or chain structures of identical molecular building blocks (e.g.  $\text{SiO}_4$  tetrahedra in the case of silicates). Therefore, by rapid cooling of the liquid, there is not enough time for these building blocks to rearrange into the crystalline form and they stay trapped in the structure of the liquid.

Furthermore, glasses often exhibit characteristic electronic and optical properties. Most oxide based glasses are good insulators and exhibit a large band-gap (ca. 9 eV in the case of silica). These glasses are transparent, because the optical transmission function is high for light in the visible range. Only ultraviolet (electronic excitations) and infrared light (vibrational excitations) fail to penetrate these glasses without absorption processes.

## 1.2 Continuous Random Network

In 1932, when William H. Zachariasen published his thoughts on “The Atomic Arrangement in Glass” [3], there was a large debate about whether glasses are built up from crystalline material [49]. Zachariasen attempted to rule out the crystallite hypothesis. First, he assumed that the bonding forces between the atoms in a glass and in a crystal should be essentially identical, because both have comparable mechanical properties. According to Zachariasen, the main feature that distinguishes a glass from a crystal

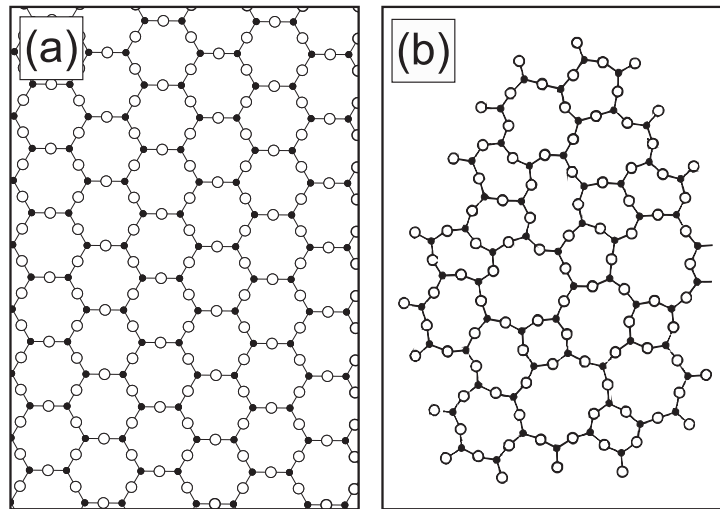


**Figure 1.2:** Zachariasen’s schematics (black dots = cations (A); white circles = oxygen). (a) The picture shows the atomic structure of a 2D  $A_2O_3$  crystal (retraced from Ref. [3] and extended). (b) An image illustrating the atomic arrangement in a 2D glass of the same  $A_2O_3$  composition (retraced from Ref. [3]).

is the lack of periodicity and symmetry. Furthermore, to sketch an atomic picture of a glass, Zachariasen used the predictions made by Goldschmidt, who suggested that tetrahedral atomic configurations are required to form glasses [50]. Because it was difficult to draw a three-dimensional (3D) picture, Zachariasen made use of a two-dimensional (2D) analogy. In Figure 1.2a, we retraced Zachariasen’s scheme of a crystal and extended it for better visibility. The black dots represent the cations (A) and the white circles depict the O atoms. The crystal in Figure 1.2a has a composition of  $A_2O_3$  and is constructed of  $AO_3$  triangles. These triangular units are connected to each other via a constant A–O–A angle of  $180^\circ$  forming regular sixfold rings. Figure 1.2b shows Zachariasen’s picture of a glass with the same chemical composition— $A_2O_3$ . Although the building blocks in this case are the same as in the crystal, namely the  $AO_3$  triangles, the glass structure lacks periodicity and long range order. This is due to the large variety of A–O–A angles which bridge two neighboring building units. The angular diversity leads to a structure consisting of differently sized rings. Figure 1.2b became the most widespread picture to illustrate the atomic structure of a glass, because it nicely shows the difference between crystals and glasses. Furthermore, Zachariasen’s postulates were very useful in explaining diffraction experiments on glasses [4]. Zachariasen’s scheme of the atomic arrangement in a glass has later been termed “continuous random network”.

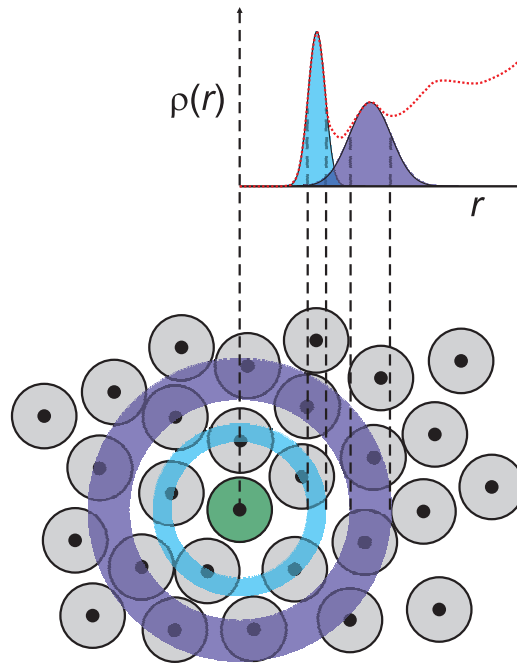


**Figure 1.3:** Schematic illustration of the PCF. The blue circle denotes the first coordination shell, the purple one the second. The green atom is the atom from where the shown PCF is defined. The red dashed curve represents the sum of all peaks. This figure has been retraced from Ref. [51].

In his work, Zachariasen also derived some simple empirical rules for the formation of oxide glasses. According to those rules, (1) one O atom is linked to not more than two A atoms, (2) the number of O atoms around an A atom must be small, (3) the O polyhedra are corner-sharing and (4) at least three corners of the O polyhedra must be shared. Oxides of type  $\text{AO}_2$ ,  $\text{A}_2\text{O}_3$ , and  $\text{A}_2\text{O}_5$  fulfill these conditions. Thus, the common glass formers  $\text{SiO}_2$ ,  $\text{B}_2\text{O}_3$ , and  $\text{P}_2\text{O}_5$  are included.

### 1.3 Pair Correlation Function

A very useful concept in analyzing the atomic correlations in amorphous materials is the pair correlation function (PCF; also called radial distribution function). A schematic representation of the PCF is displayed in Figure 1.3. The PCF is defined from a random atom  $i$  in the solid (green atom in Figure 1.3). The distance to any other point in space is the so-called radial distance  $r$ . If we denote the PCF as  $\rho(r)$ , then  $\rho(r)dr$  gives the probability to find a neighbor  $j$  for atom  $i$  at a distance between  $r$  and  $r + dr$ , with  $dr > 0$ . Figure

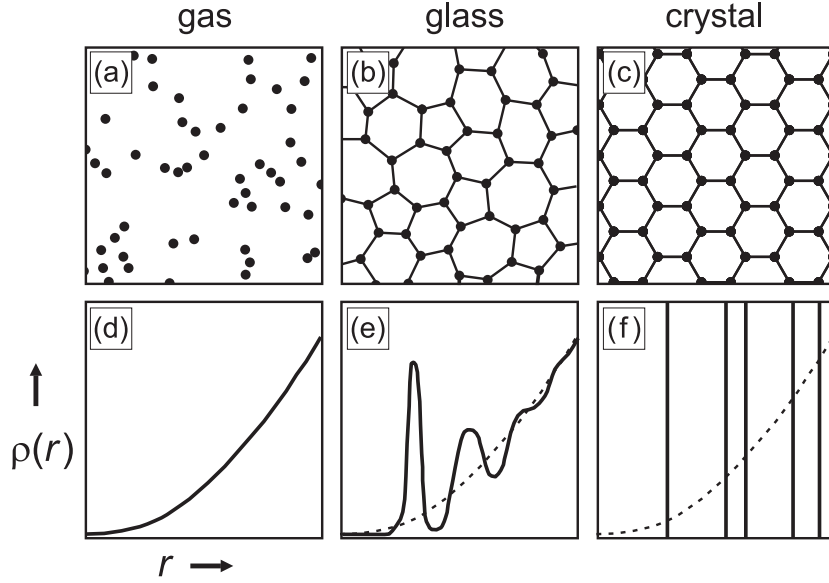


**Figure 1.4:** Correlation between atomic positions and the PCF. Panels (a)–(c) show snap-shots of the real space atomic structure in a dilute gas, a monoatomic glass, and a monoatomic hexagonal crystal, respectively. Panels (d)–(f) depict schematic shapes of the corresponding PCFs. The PCF from a random distribution of atoms (d) is shown as a black dashed curve in panels (e) and (f). These images have been adapted from Ref. [1].

1.3 shows two different coordination shells (blue and purple) giving rise to two consecutive peaks in  $\rho(r)$ . In the rest of this section, we will elaborate on the different PCFs of a monoatomic dilute gas, a glass, and a crystal.

For point particles distributed randomly in space with an average number density of  $\rho_0$ , we can easily derive the formula for  $\rho(r)$  by considering the number of expected particles in a shell of volume  $4\pi r^2 dr$ : it is this volume element times  $\rho_0$ . This model corresponds physically to a dilute gas of noninteracting atoms or molecules. For the PCF, we obtain:

$$\rho_{gas}(r) = 4\pi r^2 \rho_0. \quad (1.1)$$

Figure 1.4a shows a snap-shot of the particle positions in this model. The corresponding PCF is plotted in Figure 1.4d.

Things look different, if we consider a simple monoatomic glass (Figure 1.4b). There is a certain minimal distance  $r_{min}$  between the atoms and therefore the corresponding PCF,  $\rho_{glass}$ , is zero for  $r < r_{min}$  (Figure 1.4e). Furthermore, the atomic arrangement in a glass is not completely random (see also section 1.4). Due to the correlation between the atoms and their nearest neighbors (NNs), there is a series of peaks in the PCF. The first peak



is usually sharp, as it is defined by the bond length between two adjacent atoms. The following peaks, however, increase in width and get more diffuse. The correlation gets weaker with increasing radial distance. For large distances,  $\rho_{glass}$  approaches the value of  $\rho_{gas}$ .

For a crystal lattice (Figure 1.4c), the PCF, if we neglect thermal effects, is a sum of delta functions (Figure 1.4f):

$$\rho_{crystal}(r) = \sum_j z_j(r) \delta(r - r_j) \quad (1.2)$$

where  $z_j(r)$  is the coordination number in the  $j$ -th shell. The first peak of  $\rho_{crystal}$  coincides with  $\rho_{glass}$ , as the NN interactions are very similar in both cases. The next peaks, however, show substantial deviation. For large distances, the peaks in  $\rho_{crystal}$  become very closely spaced.

## 1.4 Ranges of Order

In section 1.1, we learned that glasses lack long range order. Nevertheless, the glass structure is not completely random and it is possible to characterize order on different length scales. Traditionally, order in glasses was divided into three ranges: short, intermediate, and long [54]. Adrian C. Wright pointed out that in the case of network solids, such as vitreous silica, it is more convenient to introduce the four ranges I–IV [5, 52], which are briefly addressed hereafter.

Figure 1.5a shows a typical neutron diffraction (ND) PCF of bulk vitreous silica. In Figure 1.5b, the first three ranges of order are indicated by arrows and additionally illustrated by silica model structures (Si: green balls; O: red balls).

**Range I** – The first range represents the structural building unit of a given amorphous solid. This unit can be quite complex and even a combination of several structural units is possible. In covalent networks, well-defined building blocks are present, such as the  $\text{SiO}_4$  tetrahedron in vitreous silica or the  $\text{AsS}_3$  pyramid in melt-quenched stoichiometric  $\text{As}_2\text{S}_3$  [52]. The first range in vitreous silica is primarily characterized by quantities within the  $\text{SiO}_4$  tetrahedron: the Si–O and O–O distances, as well as the O–Si–O angle.

**Range II** – The second range reflects the interconnection of two adjacent structural. Most commonly, the structural building blocks in covalent systems share corners, but there are also edge sharing structures, e.g.  $\text{GeSe}_2$  [52]. In bulk vitreous silica, the connection of two  $\text{SiO}_4$  tetrahedral units not

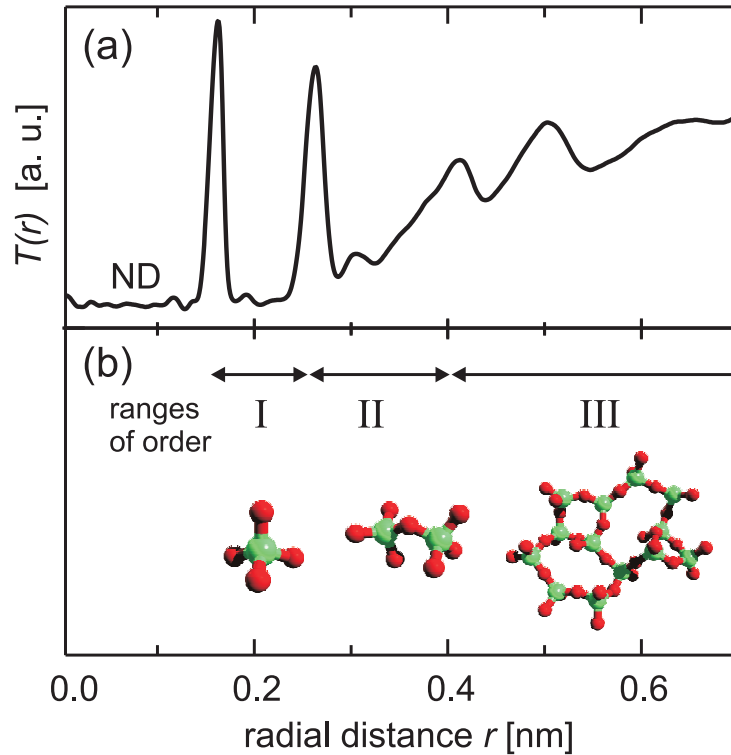


**Figure 1.5:** Ranges of order in network solids as proposed by Wright [5, 52]. (a) An ND PCF of bulk vitreous silica (retraced from Ref. [53]). (b) Schematic visualization of the different ranges of order (Si: green, O: red).

only involves the Si–O–Si bonding angle, but also the torsion angle at the bridging O atom. Furthermore, range II in vitreous silica is characterized by the Si–Si distance between two neighboring building blocks.

**Range III** – The third range describes order beyond adjacent structural units and is thought to extend to about 1 to 2 nm [54, 55]. For simple network materials, it can be defined in terms of the network topology. An important concept in this context is the ring size distribution. Range III can also be characterized by the PCF above about 0.4 nm and by the Si–Si–Si angle in the case of vitreous silica.

**Range IV** – Although long range order is absent in amorphous materials, there may be longer range density fluctuations that arise, e.g., from phase separations.

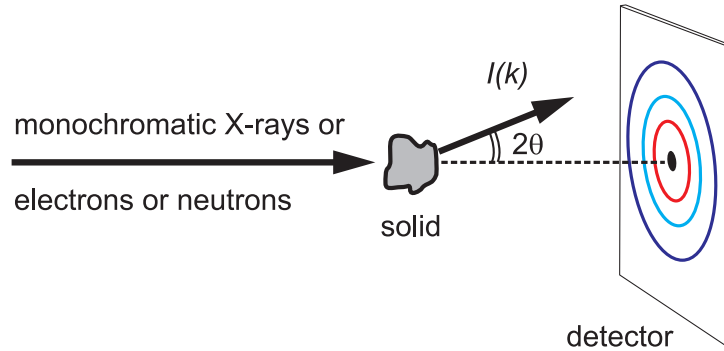


**Figure 1.6:** Schematic representation of a diffraction experiment (retraced from Ref. [1]).

## 1.5 Methods for Glass Studies

In this section, experimental and theoretical methods that have been used to study the structure of glasses are briefly summarized. Note that this is neither an extensive nor an exhaustive overview and for more information, consult the excellent overview articles in this field [5, 6] as well as textbooks [1, 56].

### 1.5.1 Experimental Methods

Diffraction methods were the first techniques applied to probe the structure of glasses. Figure 1.6 shows a schematic geometry of a diffraction experiment. A beam of monoenergetic electrons, X-rays, or neutrons is directed at the sample. The resulting diffraction pattern directly reveals, whether a sample is crystalline or amorphous. A diffraction pattern of a single crystal exhibits a set of sharp spots according to Bragg's law:

$$2d \sin \theta = n\lambda \quad (1.3)$$

where  $d$  is the distance between two lattice planes,  $n$  is the order of reflection,  $\theta$  is the angle between the incoming radiation and the normal of the lattice plane, and  $\lambda$  is the wavelength. The wavelength of the incident photons ( $\lambda = hc/E$ ), or the de Broglie wavelength of the incident particles ( $\lambda = h/\sqrt{2mE_{kin}}$ ) is chosen such that it is of the order of interatomic distances.

A powder sample of a crystalline material consists of small, randomly oriented crystalline grains. Therefore, such kind of samples display sharp rings in their diffraction patterns (see Figure 1.7a for a diffraction pattern of  $\alpha$ -quartz, a crystalline form of silica). In contrast, amorphous solids lack

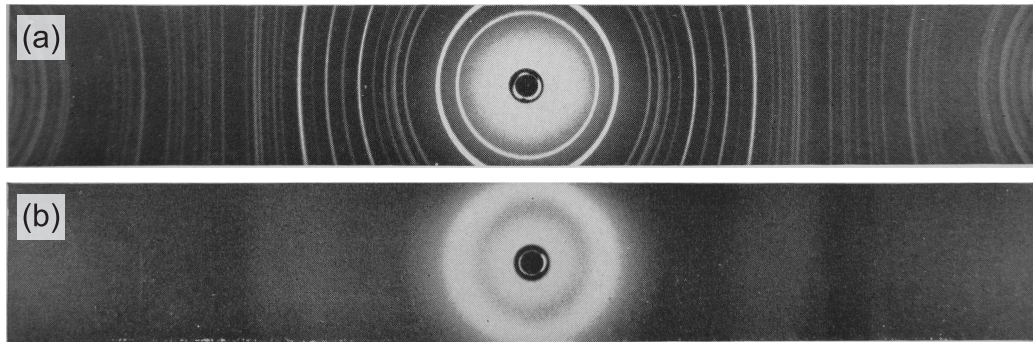


**Figure 1.7:** Two X-ray diffraction patterns. (a) Powder sample of  $\alpha$ -quartz. (b) Vitreous silica. Taken from Ref. [57].

crystal planes and therefore Bragg's law is not directly applicable. However, their diffraction patterns are not completely structureless: amorphous samples show one or several diffuse halos (see Figure 1.7b for a diffraction pattern of vitreous silica). This indicates that amorphous materials still have a certain degree of order.

Quantitatively, a diffraction experiment yields the scattering interference function  $I(k)$ , where the scattering vector  $k$  is defined via the observed scattering angle  $2\theta$  by  $k = (4\pi/\lambda) \sin \theta$ . The corresponding PCF can be calculated by Fourier transforming  $I(k)$ . Although it sounds simple, this process requires very careful acquisition and processing of the data [58–61].

Special attention was drawn to the puzzling nature of the first sharp diffraction peak in vitreous materials, e.g. the inner halo in Figure 1.7b. It stems from the most slowly decaying real space Fourier component with the highest period [5]. For vitreous silica, the peak is situated at  $1.53 \text{ \AA}^{-1}$ , being equivalent to a real space periodicity of  $2\pi/(1.53 \text{ \AA}^{-1}) = 4.1 \text{ \AA}$  [5]. This value has been attributed to the periodicity of cages in the network structure [62–64].

Note that X-ray diffraction (XRD) and ND measure different atomic properties. Whereas X-rays interact with the electrons, neutrons are sensitive to the nuclei. In the XRD case, an electron distribution has to be assumed leading to possible uncertainties. The position of the nuclei, however, might differ from the center of the electron cloud. Thus, PCFs calculated from XRD and ND might suffer from errors.

Although diffraction methods are able to yield very high resolution data, they have several limitations: (1) the structural information is averaged over a large sample volume, depending on the characteristics of the incident beam, (2) they give, in the first place, only information in reciprocal space, and (3) the maximum that can be obtained is a one-dimensional (1D) PCF, which

makes it impossible to characterize a 3D structure in all its details. Therefore, the only way to understand diffraction experiments is by comparing the experimental PCF to PCFs calculated from coordinates of hand-built or computer-generated structural models (see section 1.5.2). However, even a perfect match between model and experiment is not a guarantee that there are no other models that would fit equally well [52].

In addition to diffraction methods, many other experimental techniques were applied to glasses. The vibrational properties of glasses can be studied using infrared and Raman spectroscopy. Characteristic vibrational modes in vitreous silica were observed by means of infrared spectroscopy [65–67]. The application of Raman vibrational spectroscopy supplied information about ring configurations in vitreous silica [68, 69]. Furthermore, from nuclear magnetic resonance measurements, bond angle distributions were derived [70–72].

Scanning probe methods possess the potential to resolve atomic surface structures in real space (see section 2.3). The application of scanning probe methods to cleaved glass surfaces [10–15] and to glassy metals [16] has been shown. However, a detailed and unambiguous atomistic assignment of the observed structures was hindered by rough surfaces and large corrugations. These obstacles can be overcome by modern thin film preparation and modeling concepts. In particular, thin oxide films on metal supports represent a versatile material class that can be studied by well-established surface science tools [73].

### 1.5.2 Theoretical Methods

As described before, a 1D PCF is the maximal structural information a diffraction experiment of an amorphous solid can provide. Before the advent of computers, scientists attempted to understand the 3D atomic structure of glasses by building handmade ball and stick models [74–77]. Especially Bell and Dean were very successful in mimicking the structure of vitreous silica [77]. They built a large model from polystyrene spheres and steel wires. The coordinates were extracted from the physical model using a photogrammetric technique. From these atomic positions, Bell and Dean calculated the PCF and found good agreement with PCFs obtained in XRD and ND experiments. To learn more about the ring size distribution of 2D random networks Shackelford and Brown extended the Zachariasen scheme [78, 79].

The manual model building was, however, very tedious and time-consuming. In addition, the model size was limited and the structure may be influenced by the designer’s prejudice [80]. Therefore, when the use of computers became common practice, scientists started to simulate 3D glassy

structures using various methods. The first simulated glass structures were generated by molecular mechanics [81, 82]. This method is similar to manual model construction: the network is built up following certain predefined rules. However, this method neglects the interaction between the particles. In contrast, in molecular dynamics (MD), Newton's equations of motion are numerically solved for all particles in the model [83]. This method was applied to silica glass in a number of studies [84–93]. A large number of atoms can be simulated using MD [94]. However, the result of an MD simulation strongly depends on the choice of interatomic potentials [80], which is not always straightforward. In reverse Monte Carlo (RMC), the model is adjusted until the model's structural factor is consistent with experiment [95].

Density functional theory (DFT) is an *ab initio* method that has strongly influenced the theoretical description of atoms, molecules, liquids, and solids [96–98]. Vitreous silica structures were simulated using DFT [99–101]. Car and Parrinello suggested to combine MD with DFT to study larger systems than with pure DFT [102]. This *ab initio* method was also applied to the study of glasses [103, 104]. However, *ab initio* methods generally are very computer-time consuming and, therefore, the sample size is limited. As amorphous systems lack periodicity, it is of great interest to perform statistical analyses of large glassy samples. Simulating large clusters of amorphous materials is still a challenge regarding computers and methods.

# Chapter 2

## Methods and Experimental Implementation

This chapter addresses the experimental methods used in this work. It embraces basic theory about the working principles of low energy electron diffraction, Auger electron spectroscopy, as well as low temperature scanning tunneling microscopy and noncontact atomic force microscopy. Furthermore, we consider practical implementation issues of the applied techniques.

### 2.1 Low Energy Electron Diffraction

Low energy electron diffraction (LEED) is a powerful technique to determine the surface structure of single crystals and adsorbate layers. Figure 2.1a shows a schematic view of a LEED setup. A beam of monoenergetic electrons is directed at the surface. To guarantee the highest surface sensitivity, the kinetic energy of the incident electrons is set between 50 and 200 eV, which is at the minimum of the electron mean free path in solids [105] (also referred to as the “universal curve”). At these energies, electrons are only able to penetrate the solid up to a few atomic layers. Reflected electrons are visualized on a fluorescent screen. A grid system separates elastically from inelastically scattered electrons.

Constructive interference of the elastically back-scattered electrons takes place if the path difference between electron waves originating from neighboring sites is equal to an integer multiple of the electron wavelength (see Figure 2.1b for a 1D illustration). For a 2D case with normal incidence, this rule can be expressed in the following relation (compare to equation (1.3)):

$$\sin \alpha = \frac{n\lambda}{d_{h,k}} = \frac{nh}{d_{h,k}\sqrt{2mE_{\text{kin}}}} \quad (2.1)$$

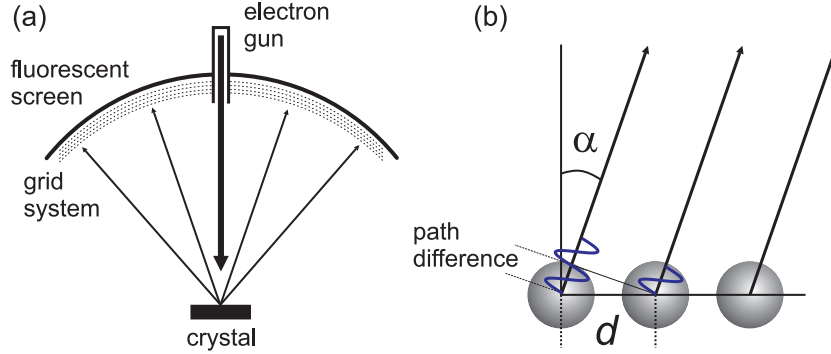


**Figure 2.1:** Low energy electron diffraction (LEED). (a) Schematic view of a LEED experiment. (b) Definition of the angle  $\alpha$  and the lattice constant  $d$ .

where  $\alpha$  is the angle between the scattered electrons and the surface normal,  $n$  is the order of reflection,  $\lambda$  the electron de Broglie wavelength,  $d_{h,k}$  the distance between two atomic rows on the surface along the direction  $[h,k]$ ,  $h$  the Planck constant,  $m$  the electron mass, and  $E_{\text{kin}}$  the kinetic energy of the electron. Note that  $\lambda$  is of the order of  $1 \text{ \AA}$  for a kinetic energy of  $150 \text{ eV}$ .

For a crystalline surface, the resulting LEED image shows a lattice of sharp spots. Due to the inverse relationship between  $\sin \alpha$  and  $d_{h,k}$ , the separation between the LEED spots is large when the interatomic distances are small, and vice versa. More exactly, the LEED experiment yields an image in reciprocal space, which is defined via the relationship

$$\vec{a}_i \cdot \vec{a}_j^* = \delta_{ij} \quad (2.2)$$

where  $\vec{a}_i$  are the base vectors of the real space lattice ( $i = 1,2$ ),  $\vec{a}_j^*$  are the base vectors of the reciprocal space lattice ( $j = 1,2$ ), and  $\delta_{ij}$  is the Kronecker symbol.

Although the typical spot size of the incident electron beam is around  $1 \text{ mm}$ , the coherence length is reduced due to energy spread, the width of the electron source and deviations from parallelity in the beam [106]. The typical resulting coherence length is of the order of  $5$  to  $10 \text{ nm}$  [106, 107]. Thus, the surface area, from which information on the periodicity can be obtained, is limited. This means that atomic correlations that are larger than the coherence length cannot be resolved in LEED. Furthermore, recording LEED intensities at different energies in combination with model calculations can yield more accurate information about the surface structure (so-called LEED-IV [108, 109]).

In summary, LEED is a versatile surface sensitive tool. It is able to unravel the symmetry of a sample's topmost atoms. However, LEED fails



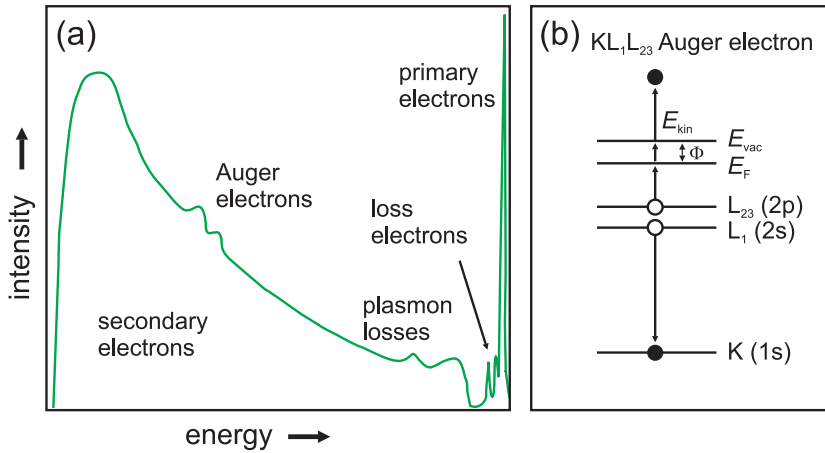


**Figure 2.2:** Auger Electron Spectroscopy (AES). (a) Schematic electron spectrum showing the different origin of some characteristic peaks. (b) Energy diagram of an Auger process. Adapted from Ref. [111].

to give information about the local structure of single atoms, molecules, or defects, as well as about complex or nonperiodic atomic arrangements. Furthermore, LEED is not element-specific.

## 2.2 Auger Electron Spectroscopy

Auger Electron Spectroscopy (AES) can be either performed with a four-grid LEED optics<sup>1</sup> or a cylindrical mirror analyzer [110]. In AES, a beam of medium-energy electrons (2–5 keV) hits the surface. By measuring the intensity of the electrons coming from the surface, one obtains a curve with characteristic features from different types of electronic interactions with the sample (see schematic representation in Figure 2.2a). Auger electrons appear as small peaks on the large background of secondary electrons, i.e. inelastically scattered electrons. To enhance the intensity of these peaks, it is common to measure the derivative of the electron current via lock-in technique.

The Auger process can take place if a primary electron with sufficient energy creates a hole in the core level of an atom [112] (see Figure 2.2b for a schematic energy diagram). The excited atom relaxes by filling the core hole (e.g. K) with an electron from a higher shell (e.g. L<sub>1</sub>). The energy is either released as an X-ray photon (this process is called X-ray fluorescence)

<sup>1</sup>For this study, the combined four-grid LEED/AES unit from SPECS with a screen size of 100 mm was used.

or by an Auger process. In the Auger transition, a second electron (e.g. from  $L_{23}$ ) is emitted, which is referred to as the Auger electron. Consequently, the kinetic energy of an Auger electron, e.g. originating from a  $KL_1L_{23}$  Auger transition, can be written as

$$E_{\text{kin}} \approx E_{\text{K}} - E_{L_1} - E_{L_{23}} - \delta E - \Phi \quad (2.3)$$

where  $E_{\text{K}}$ ,  $E_{L_1}$ , and  $E_{L_{23}}$  are the binding energies of the respective electronic levels,  $\delta E$  the energy shift caused by relaxation effects, and  $\Phi$  the work function. Thus,  $E_{\text{kin}}$  arises from a combination of well-defined atomic levels being unique for a given atom. It is, therefore, evident that AES yields element-specific information. The AES peaks can be identified using tabulated Auger transition energies [113]. Furthermore, for many elements, AES is highly surface sensitive [111]. In this work, Si, Ru, and O were investigated by AES. These elements have characteristic AES peaks in an energy window between 80 and 520 eV, where the electron mean free path is small. In some cases AES is also able to provide information on the oxidation state of certain species. These data are, however, difficult to interpret and X-ray photoelectron spectroscopy is the method of choice for this purpose. Note that the high energy of the primary electrons can inflict damage on sensitive material on the surface (e.g. biomolecules).

## 2.3 Tuning Fork Microscope

Scanning Probe Methods (SPMs) have had an immense impact in science, as they enabled the investigation of surfaces in real space with atomic resolution. The tuning fork microscope (TFM) is a new type of an SPM combining two techniques in one single sensor: scanning tunneling microscopy (STM) and noncontact atomic force microscopy (nc-AFM). In this section, the TFM is introduced and the main components are described.

### 2.3.1 Low Temperature Ultrahigh Vacuum Setup

To minimize the impact of atoms and molecules from the gas phase onto the surface, an ultrahigh vacuum (UHV) system was used. The UHV setup consists of three chambers: (1) a chamber for cleaning of samples and preparation of thin oxide films, (2) another chamber for cleaning and for transferring of samples, and (3) the microscope chamber. Figure 2.3 illustrates the cryogenic setup. A liquid helium dewar houses an exchange gas canister filled with helium gas. The microscope UHV chamber is situated inside the exchange gas canister. The helium gas thermally couples the microscope to the

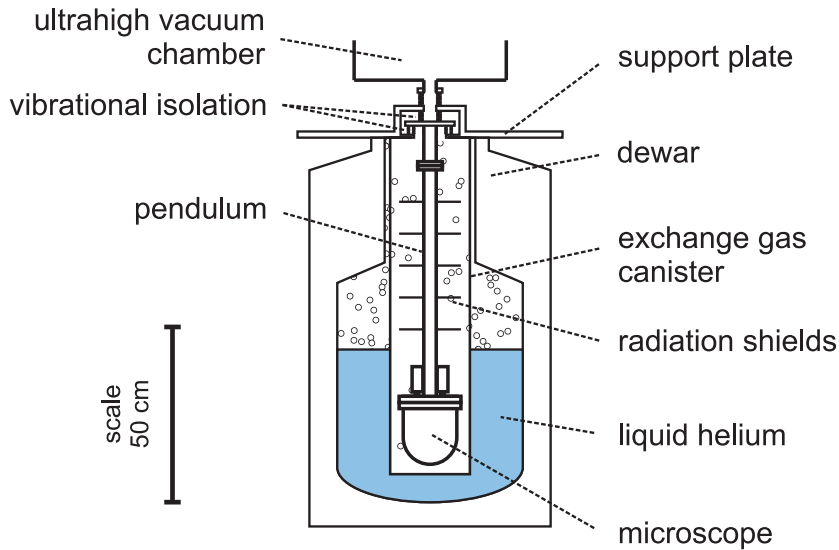


**Figure 2.3:** Schematic overview of the low temperature ultrahigh vacuum setup.

liquid helium reservoir; at the same time it isolates the microscope from vibrational noise. The whole TFM is cooled down to approximately 5 K. Low temperatures help reducing thermal drift effects, thermally induced noise, and relaxation times of piezo electric materials [114]. Furthermore, at low temperatures the energy resolution, the thermal stability, and the stiffness of the tuning fork are enhanced leading to better scanning conditions.

Damping is also crucial to reduce vibrational influence from the environment. In our setup, it is realized by (1) an eddy current damping stage supporting the whole microscope chamber, (2) a passive pneumatic damping stage, (3) active hydraulic damping feet, and (4) the sound isolation cabin which houses the whole UHV setup.

### 2.3.2 Tuning Fork Sensor

As already mentioned above, the TFM yields complementary information about the sample surface from two different methods. A tuning fork is a quartz based electronic device which has a very sharp resonance frequency, which is typically 32.768 kHz [115]. Furthermore, quartz itself is a piezoelectric material. Therefore, the tuning fork frequency can be easily accessed by measuring the resulting charge at the electrodes [116]. For these two reasons, tuning forks are frequently used in clocks and watches. In the TFM, the tuning fork is glued with one prong onto an insulating carrier plate which is mounted on a piezo actuator (see Figure 2.4). The oscillation frequency of

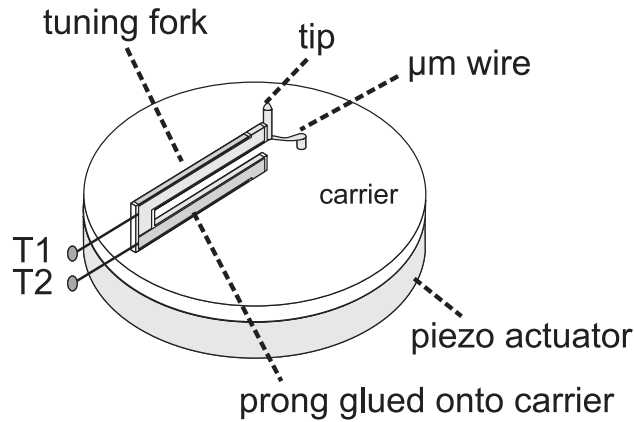


**Figure 2.4:** The scheme shows the tuning fork sensor head. The diameter of the carrier plate is 10 mm.

the tuning fork is read out via the two electrodes T1 and T2. A sharp PtIr tip is attached to the end of the free prong. The fixation on one side and the additional weight of the tip reduce the tuning fork’s resonance frequency to about 21 kHz. The metal tip is electrically insulated from the tuning fork electrodes. An additional, thin wire connects the metal tip carrying the tunneling current [117, 118]. The separation of the oscillation and the tunneling signal is essential to get reproducible results without mutual influence [119] (also termed “cross talk”). Moreover, using a metal tip guarantees full control over the applied potential at the tip.

The tuning fork is driven in a stable self-exciting oscillation mode, where the excitation signal is phase shifted with respect to the measured oscillation signal, keeping the resonance frequency constant. The oscillation mode prevents the tip from making contact with the surface when the tip-sample distance becomes small, as it introduces an additional restoring force [120]. When the tip is brought into short distance with a sample, the tuning fork senses the interaction with the surface. As a result, the instantaneous tuning fork frequency,  $f$ , shifts. The frequency shift is denoted as  $\Delta f$ :

$$\Delta f = f - f_0, \quad (2.4)$$

where  $f_0$  is the unperturbed resonance frequency of the tuning fork at a large distance from the surface. The amplitude of the oscillation,  $A_{OSC}$ , is of the order of 3 Å. A small amplitude increases the surface sensitivity [119]. A feedback loop keeps the amplitude constant [116].<sup>2</sup> If, in addition, a bias

<sup>2</sup>The described mode is sometimes termed frequency modulation dynamic force microscopy (FM-DFM); in this work we, however, will make use of the more common name “nc-AFM” [121].

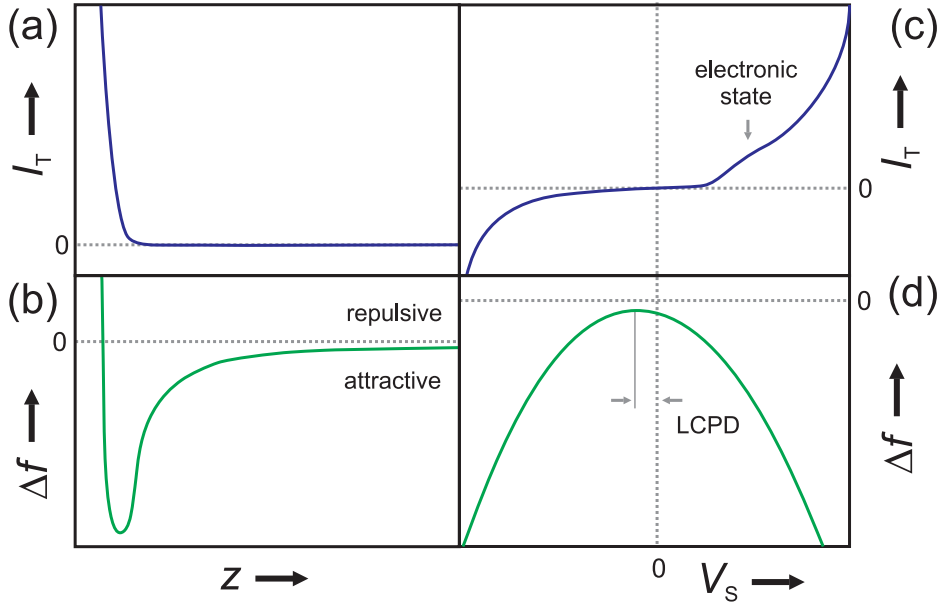


**Figure 2.5:** Schematic graphs demonstrating the dependences of the two interaction signals. (a) Tunneling current  $I_T$  vs. tip-sample distance  $z$ . (b) Frequency shift  $\Delta f$  vs.  $z$ . (c)  $I_T$  vs. bias voltage  $V_S$ . (d)  $\Delta f$  vs.  $V_S$ .

voltage is applied between the metal tip and the sample surface, electrons can tunnel through the vacuum barrier. The tunneling current  $I_T$  is measured. The whole tuning fork sensor plate is attached to a tripod made of piezoelectric material, enabling the tip to move along all three space directions ( $x$ ,  $y$ , and  $z$ ) with picometer precision. Both  $\Delta f$  and  $I_T$  can be used to obtain a topography image of the surface. Before the imaging modes are discussed, the distance and voltage dependences of both signals are described.

The dependences of  $I_T$  and  $\Delta f$  on the tip-sample separation  $z$  at constant bias voltage  $V_S$  are schematically depicted in Figures 2.5a and b.  $I_T(z)$  can be described by the following simple formula [122, 123]:

$$I_T(z) \propto \exp\left(-\frac{2}{\hbar}z\sqrt{2m\Phi}\right), \quad (2.5)$$

where  $\Phi$  is the work function of the sample,  $\hbar$  the reduced Planck constant, and  $m$  the electron mass.<sup>3</sup>  $I_T(z)$  has a very strong exponential behavior

<sup>3</sup>Note that the given formula is just an approximation of more elaborate theory about the vacuum tunneling process [124–126]. However, equation 2.5 well describes the dependence of  $I_T$  on the tip-sample distance. To correctly calculate  $I_T$  from first principles, one needs to assume a tip shape which is usually unknown in the experiment.

(Figure 2.5a). Furthermore,  $I_T(z)$  is monotonic. These two properties render  $I_T$  an excellent candidate to control the tip-sample separation.

In contrast,  $\Delta f(z)$  exhibits a more complex, nonmonotonic behavior (Figure 2.5b). At larger  $z$ , the tip-sample interaction is weakly attractive ( $\Delta f < 0$ ) due to long-range forces [127]. These forces originate from the interaction of charges (electrostatic forces) and mutually induced dipole moments (van-der-Waals forces) [107]. At smaller  $z$ , the interaction first becomes strongly attractive, reaches a minimum, and finally becomes highly repulsive ( $\Delta f > 0$ ). The origin of the described behavior are the short-range chemical forces which are of quantum mechanical nature [128]. The attractive part stems from forces generated by the total energy reduction when atoms share electrons, i.e. when atomic orbitals overlap (covalent forces). The strong repulsive part emerges from the Pauli exclusion principle, implying that no two electrons are allowed to be in one quantum state simultaneously.

The nonmonotonic shape of  $\Delta f(z)$  complicates  $z$ -control. However, short range chemical forces are accessible carrying a lot of information about the surface structure and properties. The tip-sample force  $F(z)$  can be calculated from  $\Delta f(z)$  using the formulas outlined in Ref. [129]. Nevertheless, it is common to present and discuss  $\Delta f$  data, because forces are not attainable from individual images.

Let us now consider the dependences of  $I_T$  and  $\Delta f$  on  $V_S$  at constant  $z$ . Figure 2.5c and d display schematic  $I_T(V_S)$  and  $\Delta f(V_S)$  curve shapes, respectively.  $|I_T(V_S)|$  increases exponentially with  $|V_S|$  (see Figure 2.5c). The derivative of the tunneling current,  $dI_T/dV_S$ , is proportional to the local density of states (LDOS) [130]:

$$\frac{dI_T}{dV_S} \propto \rho(z, V_S) \quad (2.6)$$

where  $\rho(z, V_S)$  is the LDOS at a given tip-sample separation  $z$  and bias voltage  $V_S$ . Already in  $I_T(V_S)$ , small shoulders indicate changes in the LDOS. The structure of the LDOS can be better resolved by directly measuring  $dI_T/dV_S$  with a lock-in technique. In this manner, bias-dependent tunneling spectroscopy can unveil electronic states of the studied surface [131, 132], as well as adsorbed single atoms [133, 134] and molecules [135, 136]. Furthermore, the second derivative of the tunneling current,  $d^2I_T/d(V_S)^2$ , is used to shed light on inelastic processes excited by the electrons. For example, vibrational modes of single molecules on the surface were measured [137, 138].

$\Delta f(V_S)$  has a parabolic shape due to electrostatic forces, which are proportional to  $(V_S)^2$  (see Figure 2.5d). At the maximum of the parabola, the electrostatic tip-sample forces are zero. At this point,  $V_S$  is not necessarily

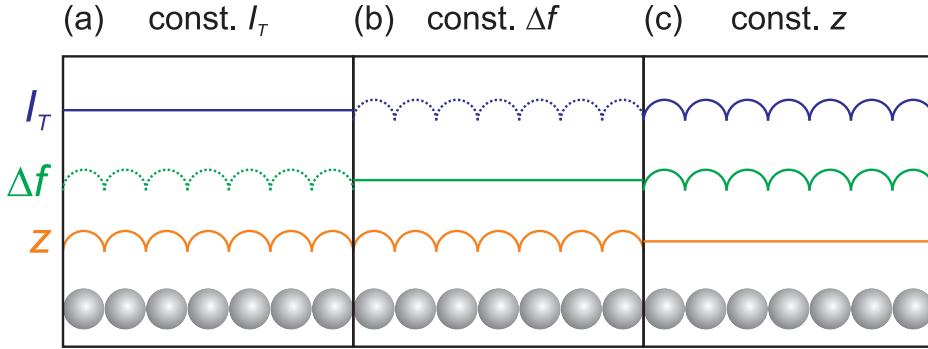


**Figure 2.6:** Overview of the different operation modes of the tuning fork microscope. (a) Constant  $I_T$  mode. (b) Constant  $\Delta f$  mode. (c) Constant  $z$  mode. The dotted curves denote the corecorded signals.

zero: a local contact potential difference (LCPD) between tip and sample can lead to a shift. The LCPD originates from an alignment of Fermi levels when tip and sample are in close proximity; it equals the difference in work function between tip and sample. Hence, the LCPD can be used to determine the locally resolved work function [139–142], to measure the charge state of single atoms [143] and defects [144], and to map the charge distribution of surfaces [145–148] and molecules [149].

### 2.3.3 Imaging Modes

During imaging, the TFM-tip is scanned laterally along the surface. The TFM can operate in three different imaging modes: (a) constant  $I_T$ , (b) constant  $\Delta f$ , and (c) constant  $z$  (see Figures 2.6a–c). The constant  $I_T$  mode is the most convenient method. Here, a feedback loop adjusts  $z$  to keep  $I_T$  constant. Thus,  $z(x, y)$  represents a contour of constant LDOS. If the surface is homogeneous,  $z(x, y)$  reproduces, in a first approximation, a topographic map of the selected surface area. Note that single adsorbates on the surface may produce a false topographic image in this mode. For example, a CO molecule produces a depression in STM while a protrusion is expected [150]. This is connected with the various tunneling channels (e.g. the scattering of electrons at the molecule) involved when measuring  $I_T$  through a molecule. Tunneling through a thin oxide film prepared on a metal support is possible if the film thickness is low [151]. High resolution can be achieved on the oxide film, even when tunneling at low  $V_S$  in the band gap region of the oxide. The scattering of electrons at the oxide film also plays an important role in this case. However, one has to be careful in interpreting low  $V_S$  STM images of oxide films, as the observed morphology might not correspond

to the structure of the topmost atomic layer [151]. Note further that, as the TFM-tip is in continuous oscillation, not  $I_T$ , but the time-averaged  $\langle I_T \rangle$  is measured. As the scan speed for one image line (ca. 1 Hz) is much smaller than  $f_0$  (ca. 21 kHz), the impact of the oscillation on constant  $I_T$  measurements is small. If, nevertheless, an exact treatment is required, one can employ the formula presented in Ref. [152] to calculate the instantaneous  $I_T$  from  $\langle I_T \rangle$ .

Mode (b) uses a feedback loop to keep  $\Delta f$  constant. This method also records a topographic map of the surface. If the LCPD between tip and sample is balanced by adjusting  $V_S$ , it is possible to minimize electrostatic forces leading to a higher sensitivity regarding the short-range chemical forces [127]. Scanning at constant  $\Delta f$  can result in atomically resolved images of some oxide surfaces (see e.g. Refs. [117, 153–156]). However, for other surfaces, this mode seems to be unsuitable, as the exact shape of the  $\Delta f(x, y, z)$  landscape inhibits constant  $\Delta f$  imaging [30]. Furthermore, the scan speed in mode (b) must be low to account for the additional time needed by the two feedback loops ( $A_{OSC}$ - and  $z$ -regulation).

In both modes (a) and (b), the other channel is corecorded. However, the corecorded signals should be interpreted with caution, as  $z$  varies during those scans and the resulting maps can suffer from artifacts. To obtain reproducible simultaneous acquisition of  $I_T$  and  $\Delta f$ , the constant  $z$  mode (c) should be used. In mode (c), the  $z$ -regulation is switched off and the tip is scanned at constant height. Obviously, it is crucial to make sure that the plane is correctly adjusted and that no large objects obstruct scanning.  $I_T(x, y)$  and  $\Delta f(x, y)$  are corecorded, yielding independent and complementary information. Recently, we could show that it is possible to image two different atom types simultaneously using the TFM (see Figure 1 of Ref. [31]). Furthermore, by choosing a small tip-sample distance, one can obtain information from the repulsive regime of the short-range chemical forces, leading to an enhanced resolution [30, 157].



# Chapter 3

## Precharacterization of Thin Silica Films on Ru(0001)

To achieve reproducible and highly resolved structural information on the thin silica film, it was very important to characterize its growth in detail. In section 3.1, we first describe how the thin silica films were prepared. Afterwards, section 3.2 conveys the results of a detailed coverage dependent study.

### 3.1 Preparation Procedure

Thin silica films have been in the scope of research for nearly two decades [158, 159]. In particular, a monolayer silica film was developed on Mo(112) [17] and explored in great detail [18–21, 23, 160, 161]. The film was prepared by evaporating Si onto an oxygen covered Mo(112) surface at 900 K in an O<sub>2</sub> atmosphere of  $5 \times 10^{-8}$  mbar and subsequent annealing to 1250 K in UHV for 5 min [21]. However, upon attempting thicker films, a well-defined structure was not observed [27]. It was concluded that due to strong interfacial Mo–O–Si bonds, the film does not grow layer by layer but rather forms ill-defined 3D structures [27]. In addition, because the monolayer is strongly bound to the metal, it has a stoichiometry of SiO<sub>2.5</sub>.

To prepare a well-defined and planar bilayer silica film, which resembles the bulk SiO<sub>2</sub> stoichiometry, it was necessary to exchange the Mo support for a different metal substrate. Ru(0001) appears to be a promising candidate, because (1) it has sixfold symmetry supporting the growth of hexagonal films, (2) it has a lattice constant of 0.271 nm [162], which matches perfectly half the lattice constant of the crystalline silica monolayer (0.54 nm), and (3) it is a durable material with a high melting point (2000 K [162]) enabling easy

**Table 3.1:** The preparation steps of thin silica films on Ru(0001).

Step	Procedure	Typical Parameters
1	Ru(0001) cleaning by – Ar <sup>+</sup> bombardment – and annealing	1 kV, 5×10 <sup>-6</sup> mbar Ar 1500 K, UHV
2	3O(2×2) adlayer	1170 K, 2×10 <sup>-6</sup> mbar O <sub>2</sub>
3	PVD of Si	350 K, 2×10 <sup>-7</sup> mbar O <sub>2</sub>
4	oxidation	1180 K, 2×10 <sup>-6</sup> mbar O <sub>2</sub>

cleaning. Ru(0001) has already been successfully employed in the preparation of thin ceria films [163, 164].

In the present work, silica films of different thickness were prepared on Ru(0001) via a four-step preparation procedure (see Table 3.1). In the following, all four steps are briefly described.

**Step 1** – Prior to film preparation the Ru(0001) substrate was cleaned by repeated cycles of Ar<sup>+</sup> bombardment at 1 kV and annealing to 1500 K. The cleanliness of the substrate was checked by LEED, AES and STM. LEED showed six sharp reflexes corresponding to a hexagonal symmetry of the atomic lattice (Figure 3.1a). AES revealed four characteristic Ru peaks at 155, 206, 236, and 278 eV (blue curve in Figure 3.2). In addition, a set of small peaks is visible in the region between 300 and 400 eV. These small peaks have been found to occur on very clean Ru surfaces only [165]. In STM, we observed flat and clean terraces (Figure 3.1b). A high resolution image demonstrates that the surface was slightly contaminated with adsorbates (Figure 3.1c). Due to a convolution with the tip, in STM, single defects and adsorbates appear larger than they are [150, 166]. In our case, the real coverage of these adsorbates was less than 0.1 monolayers (MLs), being no obstacle for the film growth. The exact nature of those adsorbates was not examined. From previous studies, however, it is known that the Ru(0001) surface is typically contaminated by C and O [167]. Note that the C AES peak overlaps with the biggest Ru peak at 278 eV and is therefore not detectable in AES.

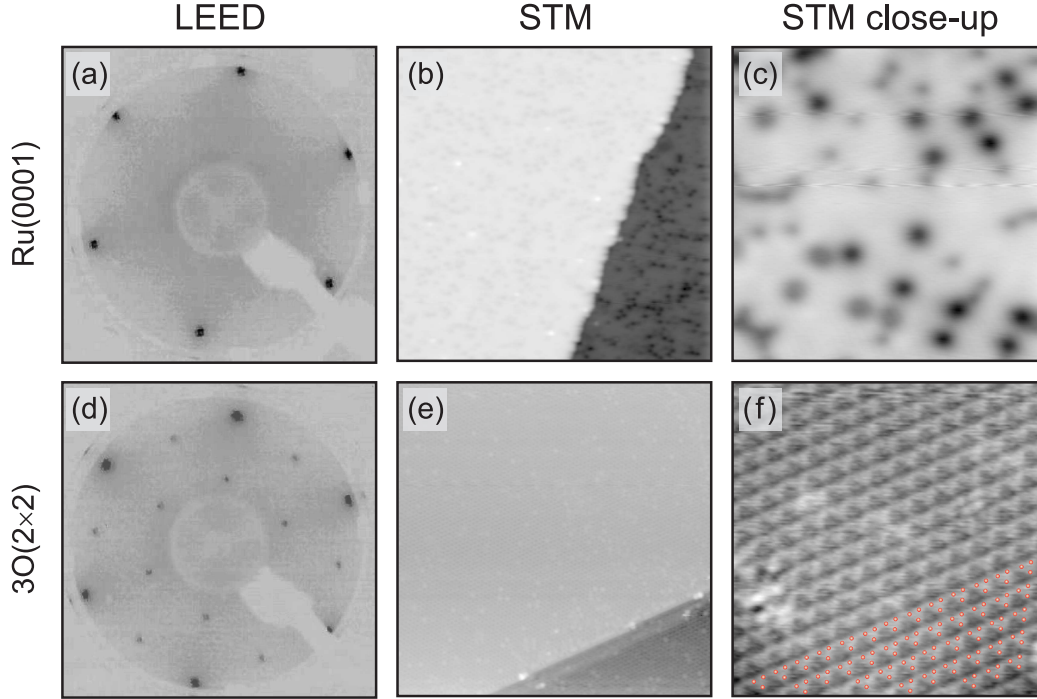


**Figure 3.1:** The Ru substrate and its O overlayer. Panels (a)–(c) depict a clean Ru(0001) surface. (a) LEED at an electron energy of 75 eV. (b) STM image,  $V_S = 500$  mV,  $I_T = 500$  pA, scan range =  $40 \text{ nm} \times 40 \text{ nm}$ . (c) STM image,  $V_S = 50$  mV,  $I_T = 500$  pA, scan range =  $7 \text{ nm} \times 7 \text{ nm}$ . Panels (d)–(f) show experiments on  $3\text{O}(2 \times 2)$  on Ru(0001). (d) LEED at 73 eV. (e) STM image,  $V_S = 400$  mV,  $I_T = 1$  nA, scan range =  $40 \text{ nm} \times 40 \text{ nm}$ . (f) STM image,  $V_S = 200$  mV,  $I_T = 100$  pA, scan range =  $7 \text{ nm} \times 7 \text{ nm}$ . Red balls: O atoms.

**Step 2** – A  $3\text{O}(2 \times 2)$  adlayer was prepared on the Ru(0001) substrate. This layer is assumed to inhibit intermixing of Si and Ru during evaporation and high temperature annealing. The  $3\text{O}(2 \times 2)$  structure has three O atoms in its unit cell and is the second most dense O overlayer on Ru(0001) [168, 169]. The most dense structure,  $\text{O}(1 \times 1)$ , can be achieved via dissociative adsorption of  $\text{NO}_2$  [170]. In contrast,  $3\text{O}(2 \times 2)$  on Ru(0001) is obtained by simply annealing the Ru(0001) sample at 1170 K in  $2 \times 10^{-6}$  mbar  $\text{O}_2$  for 10 min. The annealing temperature was measured with an alumel-chromel thermocouple and controlled with a pyrometer. After this step, the LEED pattern exhibits a  $(2 \times 2)$  superstructure resulting from the O lattice (Figure 3.1d). In AES, a faint additional peak was detected at 517 eV corresponding to O (red curve in Figure 3.2). The STM results are shown in Figures 3.1e and f. The large scale STM image displays flat and clean terraces and a sharp step edge. The close-up reveals the triangular structure of the  $3\text{O}(2 \times 2)$  layer. O

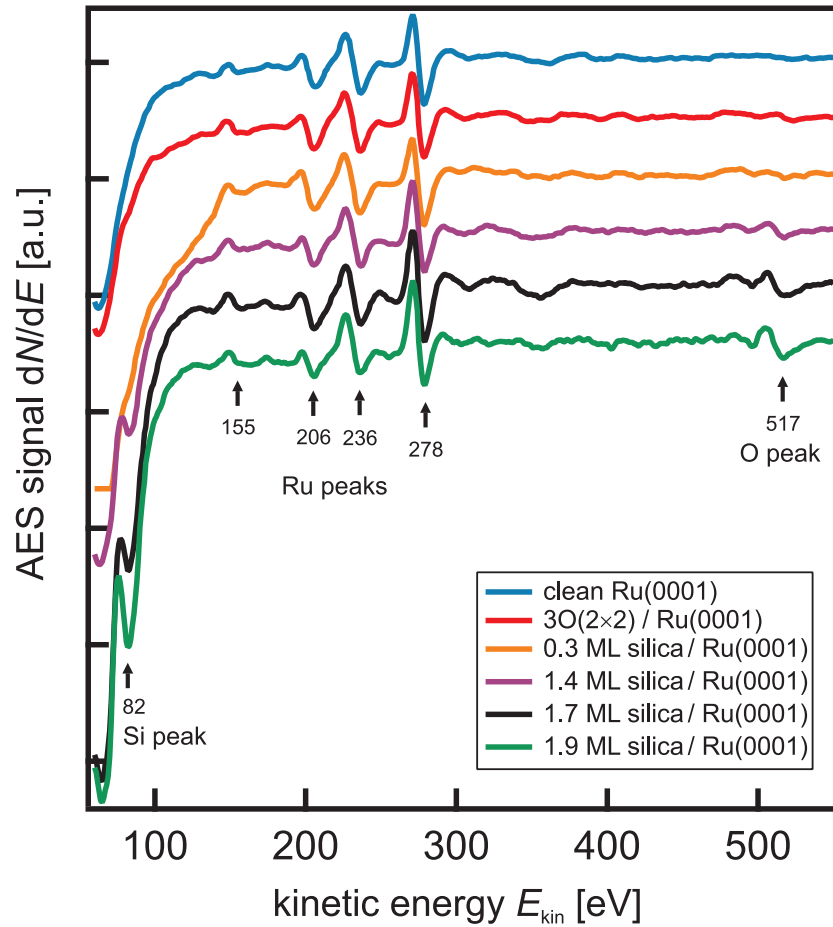


**Figure 3.2:** AES spectra of different preparations. The graph shows the AES spectra taken on clean Ru(0001) (blue curve),  $3\text{O}(2\times 2)$  on Ru(0001) (red curve), 0.3 MLs silica on Ru(0001) (orange curve), 1.4 MLs silica on Ru(0001) (purple curve), 1.7 MLs silica on Ru(0001) (black curve), 1.9 MLs silica on Ru(0001) (green curve). The curves were normalized to the largest Ru peak at 278 eV.

atoms are indicated by red balls in the lower right corner of the image.

**Step 3** – Si was evaporated onto the sample by physical vapor deposition (PVD). For this purpose, a Si rod of 4 mm thickness and high purity (99.999 %) was heated by electron beam heating using a high voltage of 1000 V. The sample was biased at the same high voltage to prevent acceleration of ions and an unintended damage of the surface. The temperature of the sample during evaporation was typically between 320 and 660 K. By evaluating more than 20 preparations, we did not observe large differences of the film morphology for evaporation temperatures in the given range. It

is known from elaborate studies carried out in the same department that a sample temperature of 100 K during PVD facilitates the growth of ordered monolayer and bilayer films [34]. However, this approach was not feasible with our setup. For the growth study, we used evaporation times from 5 to 40 minutes at an ion flux of 15 nA. We will discuss the strongly coverage-dependent structure of the silica film in section 3.2.

After the deposition of Si, the silica lacks a well-defined structure. In STM we observed 2–3 nm large and ca. 1 nm high deposits. The corresponding LEED image showed no defined structure.

**Step 4** – Finally, the sample was annealed at 1180 K in  $2 \times 10^{-6}$  mbar  $O_2$  for typically 20 minutes, resulting in a flat silica film. In our experiments, the general structure of the film did not depend on the oxidation time. Rather, the film exhibited fewer defects if the sample was annealed for a longer time. The annealing temperature (AT) was another important parameter to control the film morphology. Setting the AT too low ( $AT < 1070$  K) resulted in a defect-rich film which was not well suited for SPM. However, if the AT was too high ( $AT > 1370$  K), the film desorbed from the surface. The optimum AT of 1180 K yielded a flat film with a low number of defects.

The cooling rate is one of the critical parameters for the preparation of glassy structures. In general, amorphous materials are formed by fast cooling after high-temperature annealing [1]. In this manner, the crystallization process is bypassed (see section 1.1). In our machine, we did not observe a strong influence of the cooling rate on the film structure. A slower cooling rate rather supported the existence of monolayer patches at coverages from 1.5 to 1.7 MLs. Nevertheless, we could adjust the growth of crystalline and/or vitreous structures by a fine-tuning of the coverage: 1.9 MLs produced a vitreous film, whereas 2.0 MLs resulted in a film with coexisting vitreous and crystalline regions (see Section 3.2 for a detailed discussion). Another group from our department did observe influence of the cooling rate when using lower sample temperatures during Si deposition. Ultimately, the formation of crystalline and/or vitreous silica bilayer films depends on a delicate balance of the critical parameters [34].

## 3.2 Growth Study

To find the right Si amount to produce a bilayer silica film, a thorough growth study was conducted. We varied the initial Si load and investigated the resulting film after oxidation using LEED, AES, and STM. Figure 3.3 shows a plot of the Si deposition time at a flux of 15 nA vs. the resulting surface

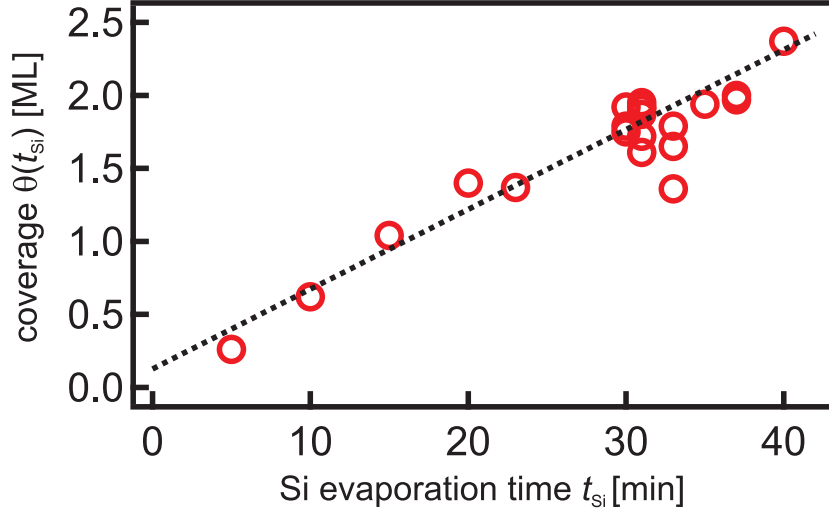


**Figure 3.3:** Growth of silica films on Ru(0001). The graph shows the coverage measured using STM vs. the Si evaporation time for more than 20 preparations (red circles). The black dotted line is a linear fit to the data.

coverage of the film as observed by STM. This graph clearly demonstrates the linear growth behavior of the silica film on Ru(0001). The bilayer coverage was accomplished after a Si deposition time of roughly 35 minutes.

The growth study will focus on characteristic intermediate coverage steps: 0.3 MLs, 1.4 MLs, 1.7 MLs, 1.9 MLs, and 2.0 MLs silica. In this notation, 2.0 MLs is the coverage needed to form the bilayer silica film. The coverage was always identified for a certain preparation using STM by calculating the following ratio:

$$\Theta(t_{\text{Si}}) = \frac{1}{A_{\text{scan}}} \sum_i A_i^{\text{silica}} \Delta h_i, \quad (3.1)$$

where  $\Theta$  denotes the coverage in MLs,  $t_{\text{Si}}$  the Si deposition time,  $A^{\text{scan}}$  the scan area of the evaluated image in  $\text{nm}^2$ ,  $A_i^{\text{silica}}$  the area of the  $i$ th silica island in  $\text{nm}^2$ , and  $\Delta h_i$  the height of the  $i$ th silica island in MLs. The coverage was determined using STM images that were at least  $50 \text{ nm} \times 50 \text{ nm}$  in size.

In the following, we will discuss the intermediate coverage steps in detail. For this purpose, we show a LEED image at an electron energy of approximately 75 eV, a large scale STM image with a scan range of  $40 \text{ nm} \times 40 \text{ nm}$ , and a higher resolution STM image with a size of  $7 \text{ nm} \times 7 \text{ nm}$  for every preparation. Bear in mind that every coverage step represents a completely new preparation starting with a clean Ru(0001) substrate.

**0.3 MLs Silica** – The LEED pattern of this preparation (Figure 3.4a) was

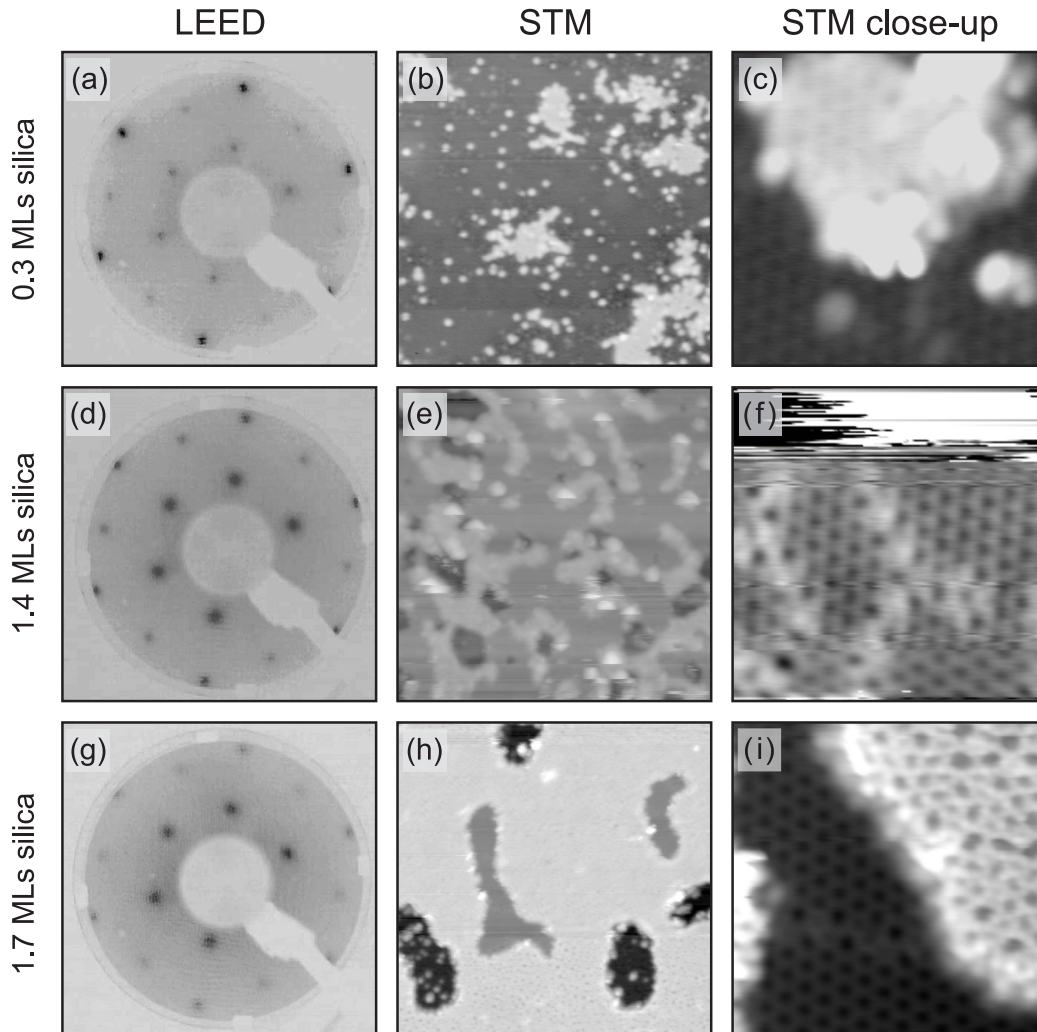


**Figure 3.4:** Low coverages of silica on Ru. Panels (a)–(c) depict 0.3 MLs silica on Ru(0001). (a) LEED at an electron energy of 76 eV. (b) STM image,  $V_S = 5$  V,  $I_T = 500$  pA, scan range = 40 nm  $\times$  40 nm. (c) STM image,  $V_S = 1$  V,  $I_T = 100$  pA, scan range = 7 nm  $\times$  7 nm. Panels (d)–(f) show experiments on 1.4 MLs silica on Ru(0001). (d) LEED at 72 eV. (e) STM image,  $V_S = 3$  V,  $I_T = 100$  pA, scan range = 40 nm  $\times$  40 nm. (f) STM image,  $V_S = 2$  V,  $I_T = 300$  pA, scan range = 7 nm  $\times$  7 nm. Panels (g)–(i) show data of 1.7 MLs silica on Ru(0001). (g) LEED at 73 eV. (h) STM image,  $V_S = 1$  V,  $I_T = 10$  pA, scan range = 40 nm  $\times$  40 nm. (i) STM image,  $V_S = 1$  V,  $I_T = 10$  pA, scan range = 7 nm  $\times$  7 nm.

very similar to the LEED image of the  $3O(2 \times 2)$  adlayer (Figure 3.1d), except that the inner  $(2 \times 2)$  spots became less distinct. In AES, a little shoulder is visible at a kinetic energy of 82 eV (orange curve in Figure 3.2). This peak is

characteristic for oxidized Si ( $\text{Si}^{4+}$ ). Any silica coverage below 0.3 MLs was not detectable in our AES instrument. The large scale STM image (Figure 3.4b) shows that the surface is covered by silica clusters (ca. 1 nm in diameter) and silica islands (ca. 5 nm in diameter). A high resolution image reveals the structure on top of an island (Figure 3.4c). The atoms form a crystalline pattern with a lattice constant of approximately 0.54 nm. By examining the structure of the  $3\text{O}(2\times 2)$  adlayer underneath, which is also resolved in the STM image, we note that this overlayer is a suitable template for the silica island growth, as both structures exhibit similar lattice spacings and crystal orientations. STM measured an apparent height difference between the silica island and the substrate underneath of approximately 1.5 Å. This is the smallest apparent height that we observed for silica islands of different thickness. We therefore conclude that an apparent height of 1.4–1.5 Å at the given tunneling conditions represents the thickness of the silica monolayer. See the section “1.7 MLs Silica” for a discussion of apparent heights in STM on silica thin films.

**1.4 MLs Silica** – By increasing the coverage to over 1.0 MLs, one would expect a completion of the silica monolayer. However, this was not the case, as the preparation with 1.4 MLs silica demonstrates. At this coverage step, the LEED spots became more diffuse than at 0.3 MLs (Figure 3.4d). Furthermore, the  $(2\times 2)$  and  $(1\times 1)$  spots were nearly equal in intensity. In AES, the Si peak was clearly visible (purple curve in Figure 3.2). The O peak also increased in intensity. Figure 3.4e displays a large scale STM image of this preparation. Evidently, there are patches of two different thicknesses: the monolayer and some elongated islands on top of the monolayer. The atomic structure of these islands could not be resolved. Furthermore, these islands made STM imaging extremely difficult, probably because they consist of ill-defined and badly conducting silica clusters that are easily manipulated by the tip. This undefined structure may be an explanation for the diffuse LEED image of this preparation. An STM image with a higher resolution is shown in Figure 3.4f. It reveals the honeycomb structure of the silica monolayer with a lattice constant of 0.54 nm and some domain boundaries between the crystalline patches. At the top of the image, the tip changed and imaging was not possible anymore.

**1.7 MLs Silica** – This preparation sheds light on the different structures of the silica monolayer and bilayer. The LEED image of 1.7 MLs silica (Figure 3.4g) was similar to the 1.4 MLs LEED image. The  $(1\times 1)$  spots of the 1.7 MLs LEED became very faint. AES showed an intensity increase of the Si and the O peak (black curve in Figure 3.2). The large scale STM image



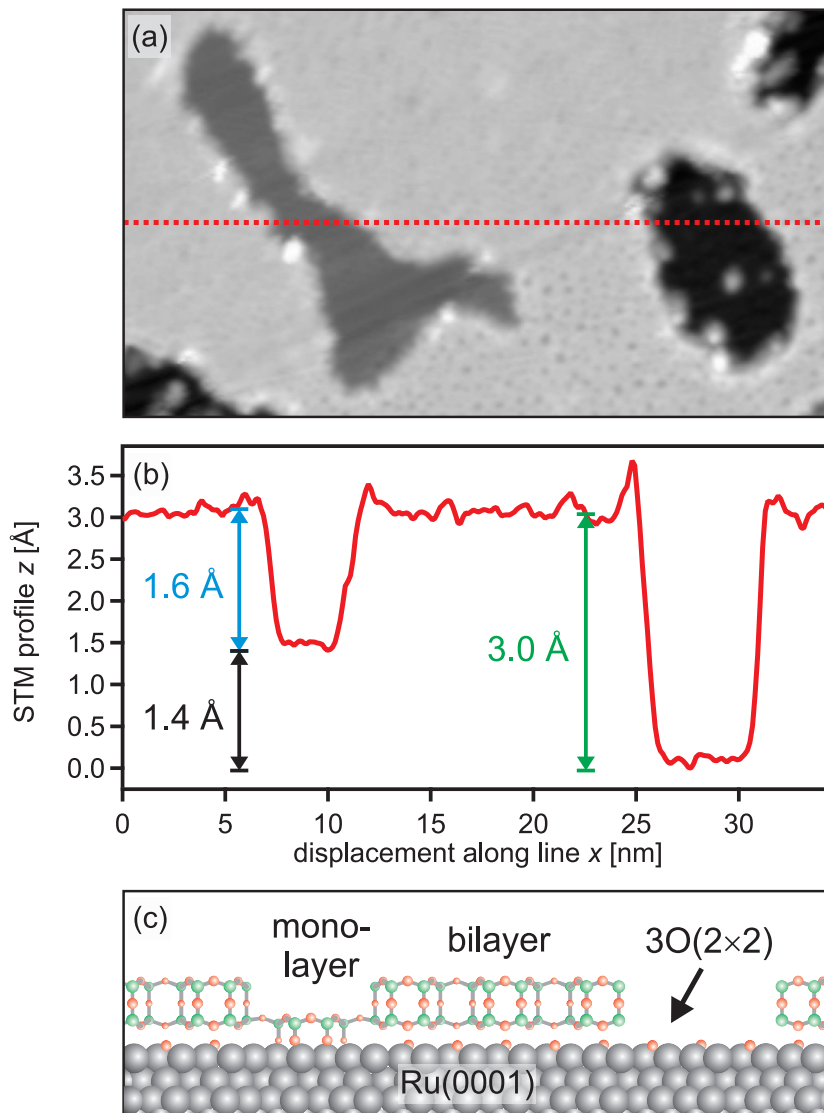


**Figure 3.5:** Apparent height of silica patches. (a) STM image of 1.7 MLs silica on Ru(0001);  $V_S = 1$  V,  $I_T = 10$  pA, scan range =  $35$  nm  $\times$   $20$  nm. (b) STM constant current contour along the red dotted line in panel (a). Arrows and figures show the apparent height differences between substrate and monolayer (black), substrate and bilayer (green), and monolayer and bilayer (blue). (c) Schematic model of monolayer and bilayer silica on  $3O(2 \times 2)/Ru(0001)$  (Ru gray, Si green, O red). The model is not to scale.

reveals a flat surface with open patches of different depth (Figure 3.4h). These height differences are analyzed in Figure 3.5.

Figure 3.5a depicts a rotated cutout from the STM image in Figure 3.4h.

Three different height levels are visible: dark gray, gray, and light gray image contrasts. An STM height profile across this image is presented in Figure 3.5b. The apparent depth of the gray and dark gray open patches was 1.6 Å and 3.0 Å, respectively. Figure 3.5c shows a schematic model of the height distribution along the given line (Ru gray, Si green, O red; sizes are not to scale). As the dark gray open patches are the deepest holes we observed in a preparation with a coverage between 1.5 and 2.0 MLs, we assign those to an exposure of the 3O(2×2) covered Ru(0001) substrate (right depression in Figure 3.5b). The open patches with the gray image contrast (left depression in Figure 3.5b) correspond to the silica monolayer, because the apparent height difference between the substrate and these patches is in the same range (1.4–1.5 Å) as for monolayer silica islands on the surface at a coverage of 0.3 MLs. Thus, the upper terrace defines the silica bilayer. Infrared reflection absorption spectroscopy of a similar preparation has shown a strong vibrational mode of 1300 cm<sup>-1</sup> normal to the surface (see Figure 4 in Ref. [34]) being characteristic for the Si–O–Si linkage [28] and proving the silica bilayer structure. A phonon at 1134 cm<sup>-1</sup>, which is characteristic for the silica monolayer, has confirmed that mono- and bilayer silica coexist at coverages between 1 and 2 MLs [34].

The apparent heights of the silica layers are an issue to be carefully analyzed. It is not straightforward to measure correct layer thicknesses with STM. In the first place, STM is sensitive to the local density of states (LDOS) of the surface (see section 2.3.2). Height differences of terrace A and terrace B can only reproducibly be obtained if terraces A and B are composed of exactly the same material with the same LDOS. If A and B are different materials, constant current STM fails to give a correct value of the height difference. Furthermore, this apparent height difference is bias voltage dependent [132, 171].

DFT calculations of a silica bilayer on Ru(0001) have predicted a thickness, i.e. the distance between the centers of the outer O atoms, of 4.3 Å [28]. In the same study, the film has been found to be weakly bound to the metal support, i.e. via van-der-Waals forces. Additional DFT simulations have shown that the distance between the silica and the Ru substrate depends on the amount of adsorbed O on the metal surface and ranges from 2.8 Å to 3.9 Å [172]. For a 3O(2×2) adlayer between the silica bilayer and the Ru support, the calculated total metal-bilayer height difference is equal to 4.3 Å + 3.8 Å = 8.1 Å. However, the measured apparent thickness of the bilayer (3.0 Å) at the given tunneling conditions ( $V_S = 1$  V,  $I_T = 10$  pA) deviates from the DFT value. The apparent height of the monolayer with respect to the metal support (1.4 Å) is also lower than the DFT value (3.9 Å [172]). This is connected with the earlier mentioned effect: the silica film is

less conductive than the metal. Therefore, STM produces a distorted (lower) value for the film thickness. See Ref. [32] for a detailed comparison of the electronic structure of monolayer and bilayer silica supported on metals.

The lateral structures of the silica monolayer and bilayer were different. Figure 3.4i displays a close-up of the silica monolayer (left part) and the bilayer (right part). The monolayer exhibits a honeycomb structure with a lattice constant of 0.54 nm, exactly the same as in the case of 0.3 MLs and 1.4 MLs. An antiphase domain boundary separates two crystalline monolayer regions. Whereas the monolayer exhibits an ordered porous structure, different pore sizes dominate the silica bilayer. The bilayer lacks long range order and, therefore, has a vitreous lateral structure.

It is utmostly surprising that we were able to prepare a vitreous film on a highly ordered substrate. The growth results on Ru(0001) are, however, affirmed by the possibility to grow vitreous silica bilayers on other crystalline substrates, i.e. on graphene [35] and on Pt(111) [36]. Furthermore, the energy of the crystalline phase is thought to be generally lower than for the respective vitreous case. It is, therefore, remarkable that such a vitreous film develops. However, DFT simulations performed by Marek Sierka, Radosław Włodarczyk, and Joachim Sauer (Humboldt-Universität zu Berlin) have unveiled the metastable nature of the vitreous silica film [29]. Their results have demonstrated that the simulated vitreous structures are 5.5–9.6 kJ/mol higher in energy than the ordered film, being much lower than for the 3D counterpart [173]. Once formed, the transition into the crystalline phase is energetically extremely unfavorable (338 kJ/mol per Si–O bond involved). Furthermore, theoretical calculations have shown that isolated silica bilayer ring structures of different size lie close in energy [29, 174, 175]. Thus, the formation of the vitreous metastable phase, which probably proceeds from silica clusters of different size, is a kinetically controlled process.

The main goal of this work is to investigate the atomic structure of the silica bilayer’s vitreous phase. See chapter 4 for a detailed analysis of atomically resolved images of the vitreous bilayer, chapter 5 for a comparative study of crystalline and vitreous bilayer regions and chapter 6 for the evaluation of a crystalline–vitreous interface.

**1.9 MLs Silica** – At this coverage the silica bilayer film was nearly closed. The LEED image at 72 eV displays two circles: an inner circle and an outer one (Figure 3.6a). The diameter of the outer circle roughly corresponds to the distance between two opposing LEED spots of the clean Ru(0001) surface (see LEED image in Figure 3.1a which was taken at 75 eV). The inset of Figure 3.6a shows a LEED image at 134 eV clearly resolving the outer circle. The outer LEED circle evidences that short range correlations are present

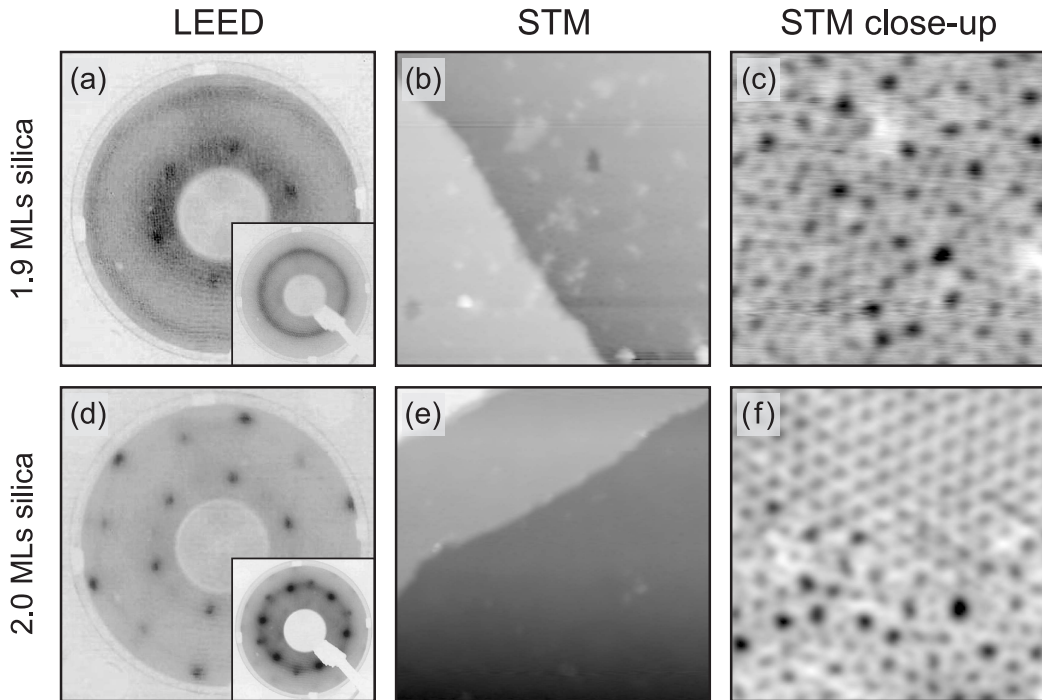


**Figure 3.6:** High coverages of silica on Ru. Panels (a)–(c) depict 1.9 MLs silica on Ru(0001). (a) LEED at an electron energy of 72 eV. The inset shows a LEED image at 134 eV revealing a circular feature. (b) STM image,  $V_S = 1$  V,  $I_T = 10$  pA, scan range = 40 nm  $\times$  40 nm. (c) STM image,  $V_S = 2$  V,  $I_T = 100$  pA, scan range = 7 nm  $\times$  7 nm. Panels (d)–(f) show experiments on 2.0 MLs silica on Ru(0001). (d) LEED at 78 eV. The inset shows a LEED image at 130 eV revealing a superposition of a circular feature and 12 spots. (e) STM image,  $V_S = 2$  V,  $I_T = 100$  pA, scan range = 40 nm  $\times$  40 nm. (f) STM image,  $V_S = 1$  V,  $I_T = 100$  pA, scan range = 7 nm  $\times$  7 nm.

in the silica film, being of the order of the Ru lattice constant (0.271 nm). These correlations are, however, not fixed to certain space directions; they are randomly distributed over 360°. The inner LEED circle corresponds to a real space length of roughly double the Ru lattice constant. Similar to the origin of the first sharp diffraction peak of bulk vitreous silica (see section 1.5.1), the inner circle is related to the periodicity of silica pores. Small crystalline areas might generate the six spots on the inner LEED circle. For a detailed analysis of circles in reciprocal space, see section 4.4.

The AES curve exhibits larger Si and O peaks than at lower silica coverages (green curve of Figure 3.2). In STM we observed nearly full coverage of the substrate with the silica film (Figure 3.6b). Only few open patches were present. As the close-up in Figure 3.6c demonstrates, the film exhibits dif-

ferently sized pores. This vitreous structure lacks symmetry and periodicity.

**2.0 MLs Silica** – We observed an interesting effect at a full coverage of the bilayer silica film: the film was partly crystalline and partly vitreous. A LEED image taken at 78 eV shows a  $(2\times 2)$  structure (Figure 3.6d), similar to the LEED at 1.4 MLs coverage (Figure 3.4d). However, faint lines connect the spots. This LEED circle becomes clearer at higher electron energies (see inset of Figure 3.6d taken at 130 eV). The LEED results suggest a coexistence of crystalline and vitreous silica bilayer patches. The large scale STM image shows a flat surface without open patches (Figure 3.6e). A close-up reveals the two different morphologies of this bilayer preparation (Figure 3.6f). Whereas the upper part of the STM picture has a regular arrangement, the lower part lacks order. The atomic structure of such a crystalline–vitreous interface will be discussed in detail in chapter 6.

### 3.3 Summary

Before the film structure could be investigated, a careful growth study was essential to this work. To precharacterize the thin film's growth, we varied the coverage of the film and explored the results by employing a combined low temperature STM/nc-AFM microscope. The study was accompanied by LEED and AES, yielding further information about the film structure and the presence of certain chemical species. A linear coverage vs. Si-evaporation-time dependence was observed. First, small silica clusters and islands formed. At increasing coverage, a mixture of first and second layer growth was found. Whereas the monolayer exhibited a crystalline structure, the bilayer lacked long range order. At nearly full coverage, the substrate was covered with a flat, extended silica bilayer film exhibiting differently sized pores. Finally, when the dosage was adjusted to a complete bilayer coverage, we observed a coexistence of crystalline and vitreous regions. The discussion of atomically resolved images of the silica bilayer will follow in the next chapters.



# Chapter 4

## The Atomic Structure of a Thin Vitreous Silica Film

This chapter focuses on the atomic arrangement in the thin vitreous silica bilayer film on Ru(0001). First, we discuss atomically resolved nc-AFM images and the procedure to construct an atomic model of the film. Afterwards, following Wright's classification of the structural order in amorphous network solids (see section 1.4) [5, 52], the order of range I–IV will be evaluated.

### 4.1 Assignment of Atomic Positions

Figure 4.1a shows an atomically resolved constant height nc-AFM image of the vitreous silica bilayer (scan size = 5.0 nm × 5.0 nm). The image reveals the complex atomic arrangement in this 2D network being very similar to Zachariasen's scheme [3] (see section 1.2). We observed protrusions at atomic separations arranged in triangles. Based on this triangular symmetry, we assigned these triangles of protrusions to one face of a tetrahedral SiO<sub>4</sub> building block. Consequently, the triangles of protrusions are triples of O atoms (red balls in Figure 4.1b). Sensitivity to the Si positions would result in a different local symmetry (see section 5.1 for further discussion). Based on the O coordinates, we determined the position of the Si atoms by calculating a circumscribed circle around every O triangle. The geometrical construction of the circumscribed circle is schematically explained in Figure 4.2a. By this method, a point is found, which has the same distance to the triangle's corners. By placing a green ball (Figure 4.1c) corresponding to a Si atom in the center of each resulting circle, we completed the 2D model of the topmost O and Si atoms. Figure 4.1c illustrates one area covered with such a model. The film showed atomic ring structures of different size and did not exhibit

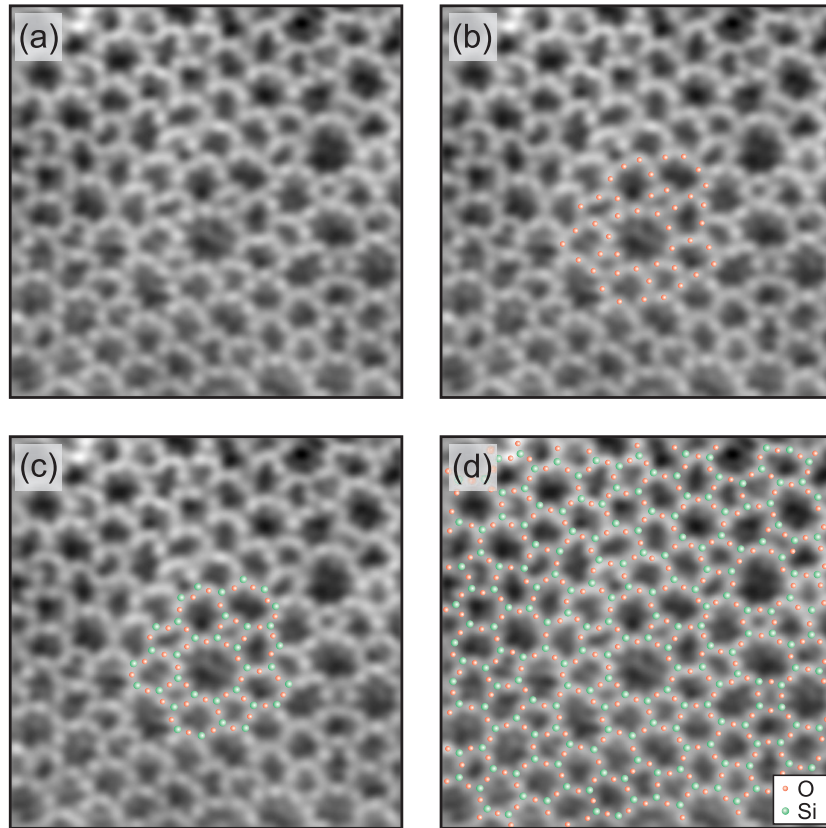


**Figure 4.1:** Assignment of atomic positions. (a) Atomically resolved constant height nc-AFM image ( $V_S = 100$  mV,  $A_{OSC} = 2.7$  Å, scan range =  $5.0$  nm  $\times$   $5.0$  nm). (b) Image from panel (a), partly overlaid with the O model (red balls). (c) Image from panel (b), additionally superimposed with the Si model (green balls). (d) Image from panel (a), covered with the complete model of the topmost Si and O atoms.

long range order.

In Figure 4.1d the nc-AFM image is completely covered by the structural model. All atoms were arranged in  $\text{SiO}_3$  triangles. No under- or overcoordinated species were observed. In 3D, this structure corresponds to a network of corner-sharing  $\text{SiO}_4$  tetrahedra. While the film is vitreous in the  $xy$ -plane (substrate plane), it is highly ordered in the  $z$ -direction. This is visualized in Figure 4.2b, showing an oblique view on a silica bilayer cluster consisting of two differently sized rings (one fivefold and one ninefold ring). The  $\text{SiO}_4$  tetrahedra of the first layer are linked via bridging O atoms to the  $\text{SiO}_4$  units of the second layer with an Si–O–Si angle of  $180^\circ$ . The linking O atoms represent a mirror plane. This particular structural element leads to a flat



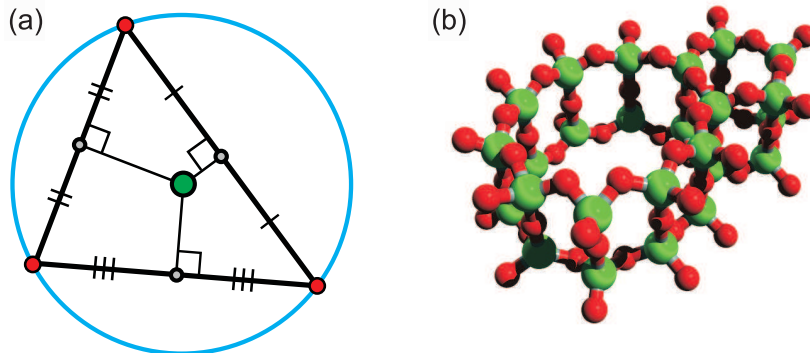


**Figure 4.2:** Structural elements of the vitreous silica bilayer. (a) Schematic showing the geometrical construction of the circumscribed circle. (b) An oblique view on two connected rings in the vitreous bilayer.

and 2D film. In other words, the film structure consists of four-membered rings perpendicular to the substrate (see Figure 4.5a), which are randomly connected, forming the 2D ring network.

The vitreous structure of the thin silica film is consistent with a weak, i.e. van-der-Waals, coupling to the metal support. The underlying metal is crystalline, but the film's registry to the substrate is lost. Thus, the film can grow in a vitreous arrangement.

The atomically resolved nc-AFM image and the derived model of the topmost layer are the starting point for further evaluation of the thin film's structure. Note that we only use the topmost O and Si positions derived from the nc-AFM image for the statistical evaluation presented in the following sections of this chapter. To compensate for the lack of information in the third dimension, in this chapter, we used the height difference between the topmost Si and O atoms from the DFT model of the crystalline silica bilayer (52 pm) [28]. In section 5.1 we substantiate this assumption.

## 4.2 Range I: The Structural Unit

In this section, the internal structure of the tetrahedral unit is analyzed (for a schematic of an  $\text{SiO}_4$  tetrahedron, see inset of Figure 4.3e). A tetrahedron is primarily defined by the tetrahedral angle, which is the angle between the center and two corners, as well as the side length. Another characteristic parameter is the distance from the center to one corner. Therefore, we will evaluate the Si–O and the O–O distance, as well as the O–Si–O angle.

In Figure 4.3a, all Si–O nearest neighbors (NNs) from the model in Figure 4.1d are connected with colored bars. The color scale represents the Si–O

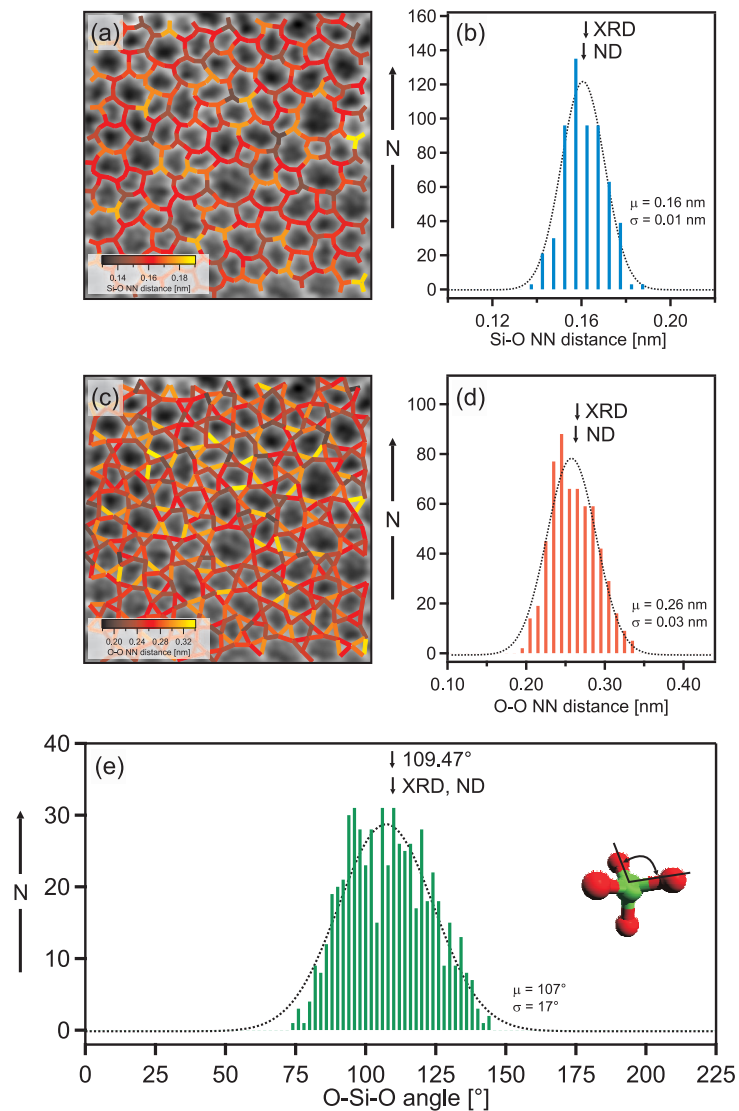


**Figure 4.3:** Characterization of range I order in the vitreous silica film. (a) Image from Figure 4.1a, overlaid with colored bars representing the Si–O NN distance (see scale bar). (b) A histogram of the Si–O NN distances. Average values from XRD and ND experiments on bulk vitreous silica are indicated by black arrows [53, 59]. (c) Image from Figure 4.1a, superimposed by colored bars representing the O–O NN distance (see scale bar). (d) A histogram of the O–O NN distances. Results from XRD and ND experiments on bulk vitreous silica are indicated by black arrows [53, 59]. (e) Histogram of the O–Si–O angles. The black arrows indicate reference values from XRD and ND data [53, 59], as well as the angle inside a regular tetrahedron ( $109.47^\circ$ ).

bond length (see scale bar). Throughout the image, a homogeneous distribution of Si–O NN distances was detected. Figure 4.3b displays a histogram of the Si–O NN distances. A Gaussian was fitted to the data and yielded an Si–O mean distance of 0.16 nm with a standard deviation of 0.01 nm. This is in good agreement with XRD [59] and ND [53] data which have been obtained on bulk vitreous silica (black arrows in Figure 4.3b).

The O–O NN distances are visualized in Figure 4.3c. It becomes clear that the O–O NN distances are equally distributed throughout the whole image. A histogram of the O–O NN distance is shown in Figure 4.3d. By fitting the data with a Gaussian, we obtained a mean O–O NN distance of  $0.26 \text{ nm} \pm 0.03 \text{ nm}$ . As the black arrows indicate, our experimental value agrees well with XRD and ND measurements on bulk vitreous silica [53, 59].

In addition, we computed NN O–Si–O angles in the atomic model<sup>1</sup> (see histogram in Figure 4.3e). The intratetrahedral angle shows a symmetric distribution with an average of  $107^\circ$  and a standard deviation of  $17^\circ$ . This value agrees well with the  $109.47^\circ$  angle in a regular tetrahedron, as well as with the  $109.8^\circ$  angle and  $109.7^\circ$  angle deduced from XRD and ND experiments on bulk vitreous silica, respectively [53, 59].

Hence, order of range I in the thin vitreous silica film reproduces the structural parameters derived from diffraction measurements on bulk vitreous silica. However, range I order is not characteristic for the vitreous nature, as it consists of well-defined building blocks ( $\text{SiO}_4$  tetrahedra). Characteristic features of the vitreous structure can be found in the ranges of higher order.

### 4.3 Range II: Interconnection of Adjacent Structural Units

Range II is characterized by the connection of neighboring tetrahedral building blocks (see Figure 4.4c for a schematic). This connection can be evaluated by examining the distance between the tetrahedral centers and the angle formed by their bonds to the bridging oxygen (see arrows in Figure 4.4c). Therefore, in this section, the Si–Si NN distance and the Si–O–Si angle are analyzed.

Figure 4.4a shows the real space distribution of Si–Si NN distances. Connecting bars are colored corresponding to the distance between two neighboring Si atoms (see scale bar). A homogeneous real space distribution was observed. The corresponding histogram is plotted in Figure 4.4b. A Gaus-

---

<sup>1</sup>In this work, only NN angles were evaluated. The specification “NN” is henceforth omitted.

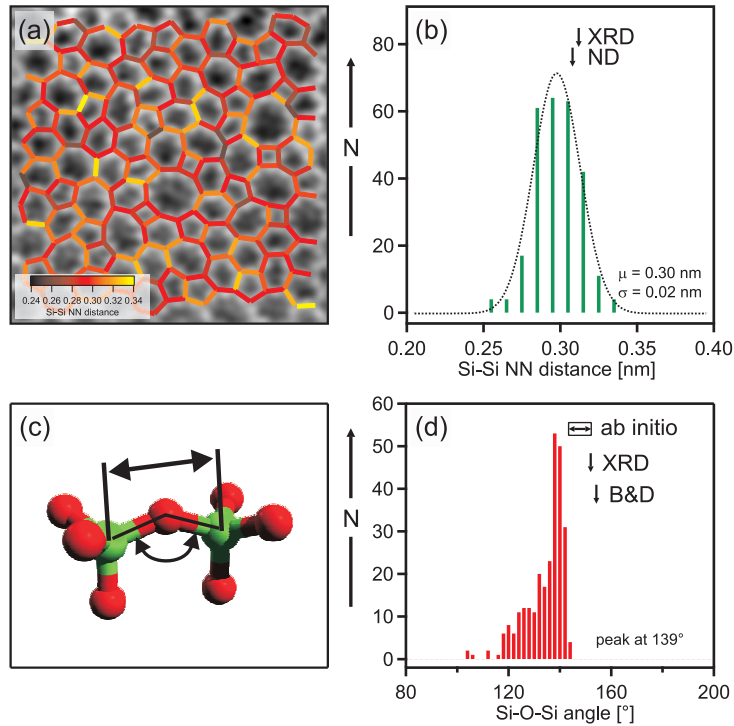


**Figure 4.4:** Characterization of range II order in the vitreous silica film. (a) Image from Figure 4.1a, overlaid with colored bars representing the Si–Si NN distance (see scale bar). (b) Histogram of the Si–Si NN distances. Average values from XRD and ND experiments on bulk vitreous silica are indicated by black arrows [53, 59]. (c) Two SiO<sub>4</sub> tetrahedral units connected via the bridging O atom. The Si–Si NN distance and the Si–O–Si angle are indicated by black arrows. (d) Histogram of the Si–O–Si angles. For a comparison to bulk vitreous silica, values from *ab initio* calculations [100], XRD [59] and Bell and Dean’s handmade model [77] are indicated by black arrows.

sian fit to the data yielded a mean Si–Si NN distance of  $0.30 \text{ nm} \pm 0.02 \text{ nm}$ . XRD and ND results on bulk vitreous silica indicate a slightly larger mean Si–Si NN distance than our measurements (see black arrows in Figure 4.4b). This is connected with a larger variety of Si–O–Si angles in 3D, discussed hereafter.

The histogram of the Si–O–Si angles is shown in Figure 4.4d. We observed a characteristic asymmetric shape of the Si–O–Si angle distribution. Therefore, it is not permissible to fit the distribution with a Gaussian. The peak in the Si–O–Si angle distribution is situated at  $139^\circ$ .

The Si–O–Si angle has been largely debated in literature [5, 176]. As it connects two tetrahedral building blocks, it is a very important angle for

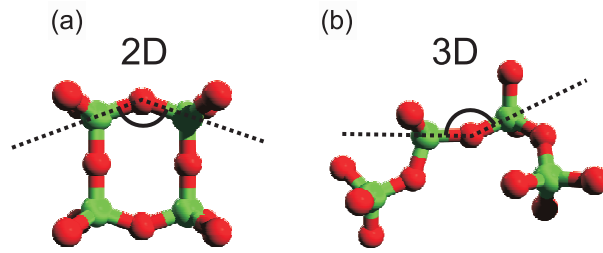


**Figure 4.5:** Comparison of Si–O–Si angles in 2D and 3D vitreous networks (Si: green, O: red). (a) A side view on the fourfold building block of the 2D vitreous silica bilayer. Here, the Si–O–Si angle is constrained by the flat structure of the film. (b) Four SiO<sub>4</sub> tetrahedra connected in 3D space. The Si–O–Si angles can assume a broader spectrum of values due to more degrees of freedom.

vitreous networks. The original XRD measurements on bulk vitreous silica from Mozzi and Warren yielded a most probable Si–O–Si value of 144° [59]. Some years later, the data were re-analyzed by Da Silva *et al.* [60]. They found 152° to be the most probable value for the Si–O–Si angle. Furthermore, Bell and Dean obtained a similar value for their hand-built model of bulk vitreous silica [77]. When these authors attempted to build a structure with a mean Si–O–Si value of 144°, they observed poor agreement with experiment. *Ab initio* simulations of bulk vitreous silica yielded mean Si–O–Si angles ranging from 143.4° to 152.2° depending on the potential, basis set and the structural optimization scheme applied [100]. A detailed analysis of the literature on measured and simulated Si–O–Si angles can be found in Ref. [176]. These authors estimate the most probable Si–O–Si angle of bulk vitreous silica to be situated near 147° with a full width at half maximum of 23 to 30° (corresponding to a standard deviation of 10 to 13°). If we compare all these Si–O–Si values to the angles calculated from distances of the 2D silica network in this study, we find a difference of approximately 4 to 13°.

The smaller Si–O–Si angles are an intrinsic feature of the vitreous silica bilayer. Figure 4.5 illustrates the different interconnections of tetrahedral units in 2D and 3D vitreous silica. In 2D, the connection of the building blocks is constrained by the flat structure of the film (see Figure 4.5a for a side view). There is a maximal Si–O–Si angle, which cannot be surpassed, because the Si atoms of, e.g., the top layer all lie in one plane. This effect is expressed in a characteristic sharp edge in the Si–O–Si distribution of a 2D vitreous network (see Figure 4.4d). However, in 3D, the Si–O–Si angles can assume a larger range of values, as there are more degrees of freedom (see

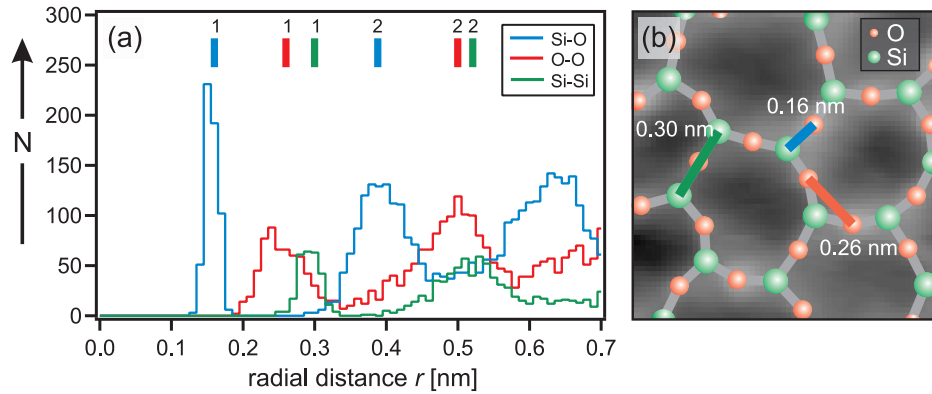


**Figure 4.6:** Evaluation of pair distances in the experimental atomic model. (a) PDHs for Si–O (blue curve), O–O (red curve), and Si–Si (green curve). Peaks are indicated by vertical colored bars. The numbers above the bars represent the respective peak order. (b) Small cutout of the vitreous silica model. Colored bars indicate the respective NN distances.

Figure 4.5b). A sharp boundary in the distribution is absent [176].

## 4.4 Range III: Network Topology

Range III order is the most discussed, yet least understood topic in glass studies. It is in this range that striking differences between crystals and glasses are found (see also chapter 5 for a detailed comparison of crystalline and vitreous regions in the thin silica film). To characterize range III order in the thin vitreous silica film, we evaluated longer range distances, the ring statistics, the Si–Si–Si angles, and a 2D Fourier transformation.

### 4.4.1 Pair Correlation Function

A useful way to characterize the atomic order in a material is to compute the PCF (see section 1.3). The great advantage of this method is the direct comparison to PCFs derived from diffraction experiments using a Fourier transformation. We calculated longer range correlations for our model and compared them to literature values.

Figure 4.6a shows pair distance histograms (PDHs) for Si–O (blue), O–O (red), and Si–Si (green) derived from the nc-AFM model. The concept of the PDH is similar to the PCF. A PDH is a histogram of the number of pairs at various mutual separations ( $r$ ) evaluated for all sites against all sites. Additionally, in Figure 4.6a, peaks are marked by vertical colored bars. First

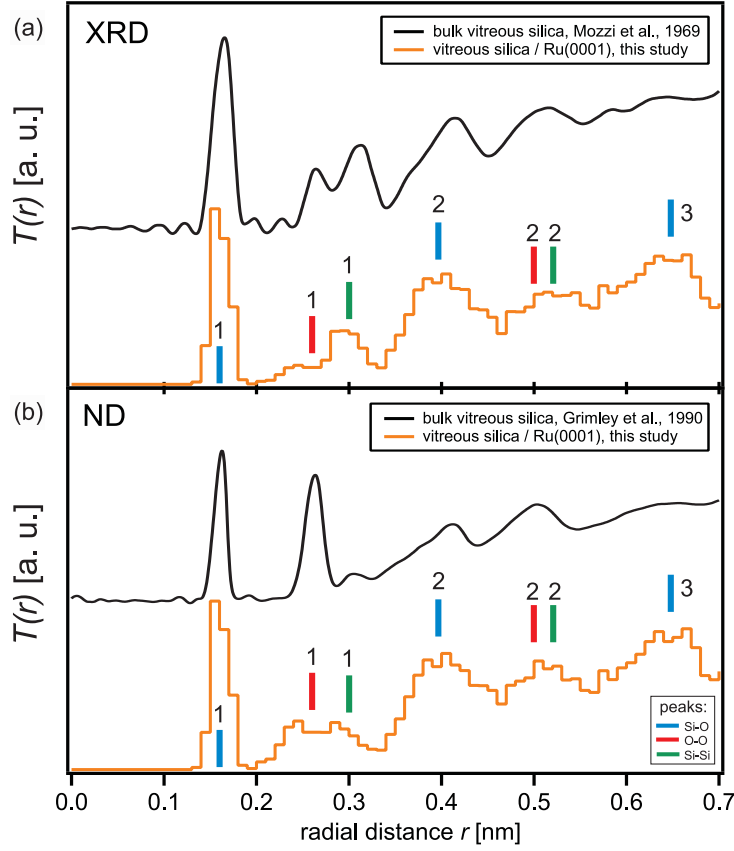


**Figure 4.7:** Pair correlation functions (PCFs). (a) Comparison of the total PCF from the vitreous silica bilayer,  $T_{\text{nc-AFM}}(r)$  (orange curve), with the PCF obtained from XRD measurements on bulk vitreous silica (black curve, retraced from Ref. [59]). (b) Comparison of  $T_{\text{nc-AFM}}(r)$  (orange curve) to results from ND on vitreous silica (black curve, retraced from Ref. [53]). Colored bars reproduce the respective PDH peak positions from Figure 4.6a.

peaks in all three distributions correspond to the respective NN distances (see Figure 4.6b), which were already discussed in sections 4.2 and 4.3. Second peaks represent the next nearest neighbor distances. Evidently, the second peaks are broader, more diffuse and exhibit a larger background than the first peaks. This is an intrinsic feature of the vitreous nature of the film: whereas the first peaks represent order of range I and II, the following peaks characterize range III order, and are therefore broader.

Moreover, we found good agreement between the PCF of the vitreous silica film and the PCFs obtained in diffraction studies of bulk vitreous silica. The total PCF of the experimentally derived structural model,  $T_{\text{nc-AFM}}(r)$ , was obtained by summing up the different PDHs using X-ray and neutron

scattering factors of Si and O according to the formulas in Refs. [77, 82].  $T_{\text{nc-AFM}}(r)$  was additionally normalized by  $r^{-1}$  to account for the 2D structure of the thin film. Figure 4.7a compares  $T_{\text{nc-AFM}}(r)$  to the PCF obtained in an XRD experiment on bulk vitreous silica, which was carried out up to a radial distance of 0.7 nm (black curve, retraced from Ref. [59]). In Figure 4.7b, we compare  $T_{\text{nc-AFM}}(r)$  to ND measurements (black curve, retraced from Ref. [53]). The major peak positions, their relative magnitudes and peak shapes of  $T_{\text{nc-AFM}}(r)$  indicate reasonable agreement with the XRD and ND PCFs. The small deviations stem from the different dimensionalities of the compared systems: while the silica bilayer on Ru(0001) is flat and 2D, the silica glass studied in diffraction experiments is 3D.

One of the highly discussed questions is how far order can extend in glasses. The maximum extension of order in the vitreous silica film is addressed in section 5.4.

#### 4.4.2 Ring Size Distribution

Another way to characterize the network topology of the thin vitreous silica film is to evaluate its ring size distribution. The ring size distribution is not directly attainable from diffraction measurements and other averaging techniques. Therefore, the presented model system offers the unique possibility in studying this quantity in real space. We define the ring size  $s$  as the number of Si atoms per ring. As rings are quite large objects, a large statistical sample is required. Therefore, for the evaluation of rings, we use a large, atomically resolved STM image (Figure 4.8a). In contrast to the nc-AFM image from Figure 4.1, this particular STM image shows the structure of the Si atoms. Note that the sensitivity of the scanning probe tip to a certain atom type is mainly dominated by the microscopic tip termination (see section 5.1 for an overview of different tip contrasts in STM). In Figure 4.8b, the STM image is superimposed by the atomic model of the topmost Si and O atoms. As in Figure 4.1d, a complex ring network is revealed. The real space visualization of the ring size distribution is presented in Figure 4.8c. Colored disks represent the polygonal area spanned by the Si atoms of every ring. This quantity is directly correlated to the ring size (see scale bar in Figure 4.8c). Strikingly, the environment of a ring depends on its size. Rings with more than six Si atoms tend to be surrounded by smaller rings. The ring arrangement is governed by the possible angles inside an  $\text{SiO}_4$  tetrahedron and angles connecting two tetrahedra (see sections 4.2 and 4.3, as well as the discussion of Si–Si–Si angles hereafter).

A histogram of the ring sizes from the STM image including ring fractions at the image boundaries is depicted in Figure 4.8d. The smallest rings in the



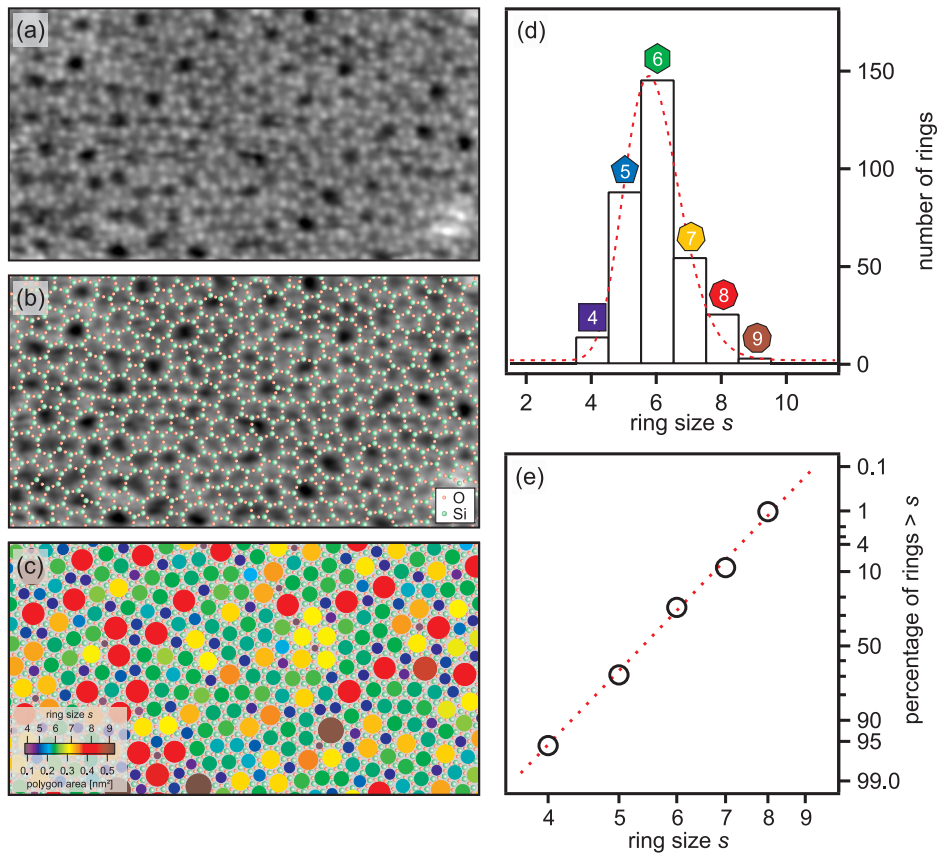


**Figure 4.8:** The ring size distribution in 2D vitreous silica. (a) Large atomically resolved STM image of the vitreous silica film revealing the Si positions ( $V_S = 2$  V,  $I_T = 50$  pA, scan range =  $12.2$  nm  $\times$   $6.6$  nm). (b) Image from panel (a) superimposed by the atomic model of the topmost Si and O atoms. (c) Real space visualization of the ring size distribution. The colored disks represent the polygonal area of the rings (see scale bar). (d) Histogram of the ring size distribution, based on the STM image in panel (a). Colored polygons indicate the different rings. The red dashed curve is a log-normal fit to the data. (e) A log-normal plot of the ring size distribution (black circles). The dashed straight line serves as a guide to the eye.

STM image consist of four Si atoms and the biggest ones of nine Si atoms. The most common ring has six Si atoms. The distribution is asymmetric around the maximum. Being preciser, the ring size distribution of the vitreous film follows a characteristic log-normal behavior. The log-normal ring size distribution of a 2D random network was first pointed out by Shackelford and Brown who analyzed an extended Zachariasen network [78]. The origin lies in the connectivity requirements of 2D random networks [78]. Fitting a

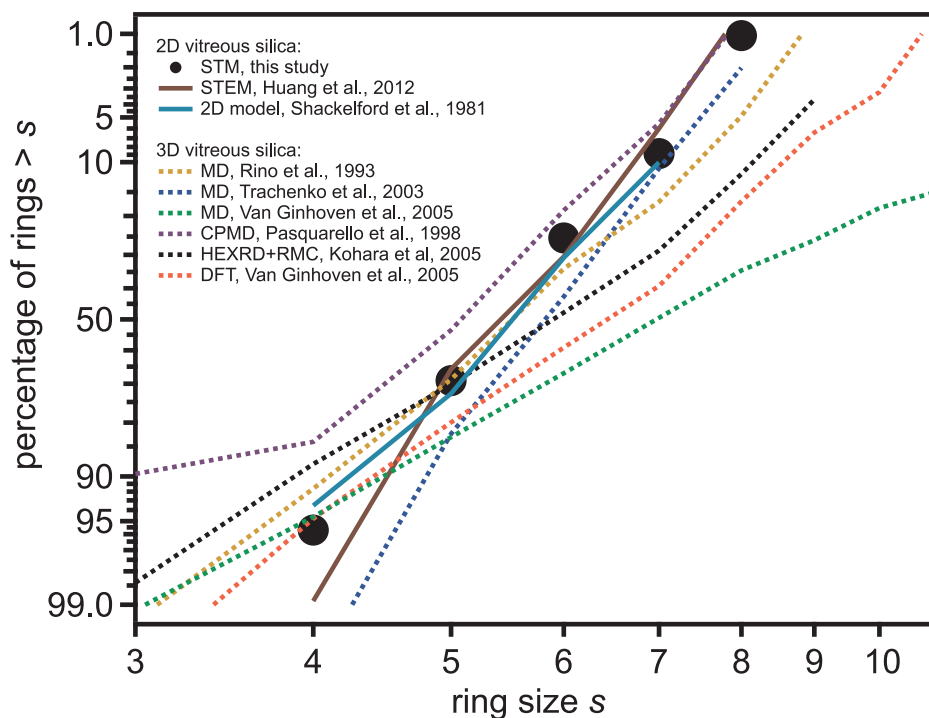


**Figure 4.9:** Log-normal plots of ring size distributions from different studies. Our STM results are compared to other 2D systems [35, 78] and to 3D theoretical models [69, 88, 100, 177, 178].

log-normal distribution function to the silica/Ru(0001) ring size distribution shows good agreement with the experimental distribution shape (dashed line in Figure 4.8d). The inherent log-normal law of the ring size distribution can also be verified by looking at a log-normal plot (Figure 4.8e). In theory, a perfect log-normal distribution gives a straight line on log-normal probability paper. The black circles represent the experimental ring statistic and indeed lie on a straight line (see red dashed line in Figure 4.8e, serving as a guide to the eye).

As pointed out by Wright [5], it is very difficult to experimentally assess the 3D ring size distribution in vitreous silica. However, various research groups have published the ring size distributions of theoretical models. Figure 4.9 displays a log-normal graph comparing 2D and 3D ring size distributions. In 3D, a ring is regarded as a loop, and can be a nonplanar structure. The corresponding size is determined by the shortest path analysis as proposed by King [179]. The black dots in Figure 4.9 depict the ring size distribution from our study (same as in Figure 4.8e). The other 2D ring size distributions originate from the STEM study of a vitreous silica bilayer on graphene [35]

and the 2D model from Shackelford and Brown [78] (solid curves). These 2D systems are compared to studies of 3D structures obtained from molecular dynamics (MD) [88, 100, 177], Car-Parrinello MD (CPMD) [69], high energy XRD in combination with reverse Monte Carlo modeling (HEXRD+RMC) [178], and DFT [100] (dotted curves). The distribution of rings obtained from STM agrees well to Shackelford's 2D model. The STEM results are also in decent agreement with the other 2D models. The 2D systems have all a similar slope in their log-normal ring size distributions. However, the slope of the 3D models is in general smaller. This means that there is a preference to larger loops, which can be explained by the larger degree of freedom in 3D.

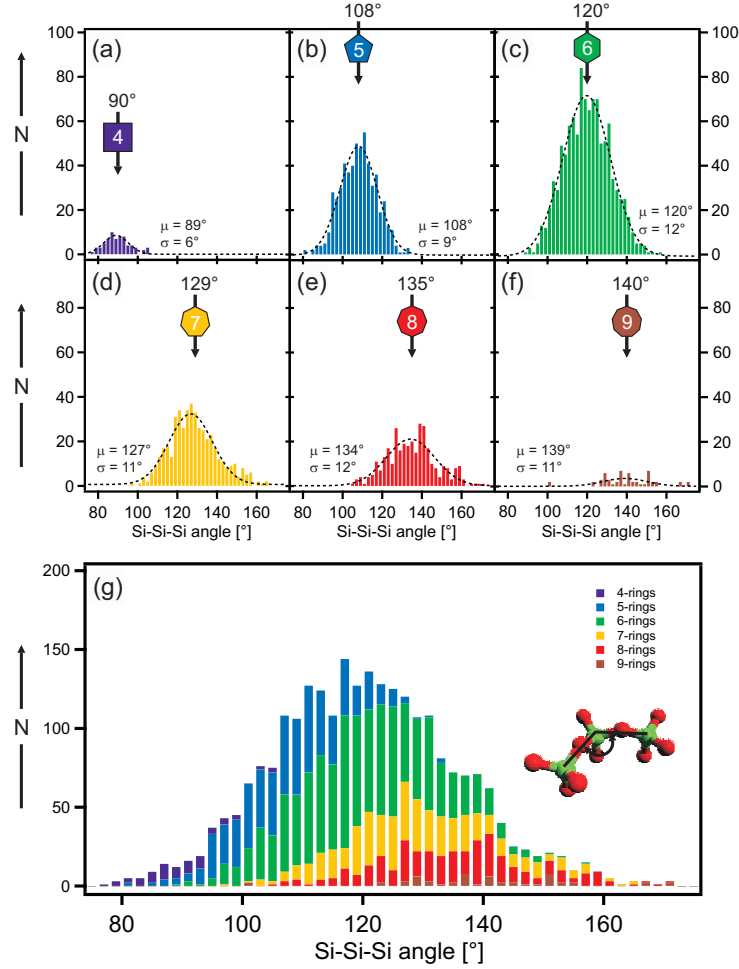
#### 4.4.3 Si–Si–Si Angle Distribution

Figure 4.10 presents the result of the Si–Si–Si angle computation, based on the experimental model from Figure 4.8b. The Si–Si–Si angle expresses the internal structure of a silica ring (see also inset of Figure 4.10g). Figures 4.10a–f display histograms of the Si–Si–Si angle inside four- to nine-membered rings, respectively. In addition, for every ring size, the angle of the corresponding regular polyhedron is marked by a black arrow. The Si–Si–Si angles scatter around the polyhedral angles, showing that the rings in the vitreous silica film have a distorted shape. The sum of all ring contributions is plotted in Figure 4.10g. The Si–Si–Si angle exhibits a broad distribution, having a maximum at  $120^\circ$ , corresponding to the average angle inside the most frequent, i.e. sixfold, ring. The broadness of the distribution demonstrates how flexible the internal ring structure of this 2D network structure can be.

#### 4.4.4 Fourier Transformation

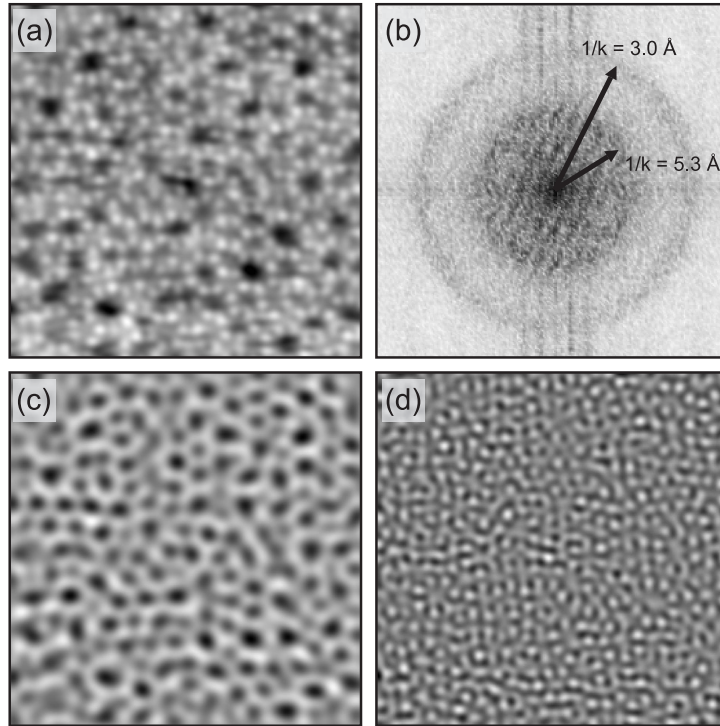
A Fourier analysis can also shed light on longer range correlations within the vitreous silica film. Figure 4.11a depicts a cutout from the STM image in Figure 4.8a. A fast Fourier transformation (FFT) of this image is displayed in Figure 4.11b. The FFT reveals two diffuse circles in reciprocal space. Similar circles appeared in the LEED image of the purely vitreous film (see Figure 3.6a). Fourier back-transforms unveil the origin of the two circles.

Figure 4.11c illustrates an inverse Fourier transform of the inner FFT circle only. Clearly, the porous structure of the bilayer is visible, however, lacking the atomic protrusions. The inner FFT circle corresponds to a  $1/k$  value of  $5.3 \text{ \AA}$ ,  $\vec{k}$  being a vector in reciprocal space and  $k = |\vec{k}|$ . This length is exactly equal to the average NN distance between two pores in



**Figure 4.10:** Histograms of Si-Si-Si angles calculated from the atomic positions in the STM image in Figure 4.8a. (a-f) Histograms of Si-Si-Si angles inside four- to nine-membered rings. Arrows and numbers at the top indicate angles in regular polyhedra. (g) Total Si-Si-Si angle distribution. Contribution from different ring sizes are colored correspondingly.

the 2D silica film. From the coordinates in Figure 4.8b, an average NN distance between the centers of two rings of  $5.3 \text{ \AA} \pm 0.7 \text{ \AA}$  was obtained. For a crystalline film, which consists of sixfold rings only, the calculated ring-to-ring distance is only slightly larger ( $5.4 \text{ \AA}$  [28]). Thus, the inner FFT circle represents the network structure and can be explained in terms of a rotationally invariant ring-to-ring correlation. Therefore, the inner FFT and LEED circle are closely related to the first sharp diffraction peak of bulk vitreous silica, which was attributed to the periodicity of the holes in the network structure [62–64] (see also section 1.5.1).



**Figure 4.11:** Fourier analysis of an STM image of vitreous silica. (a) Cutout from the STM image in Figure 4.8a ( $V_S = 2$  V,  $I_T = 50$  pA, scan range =  $7.0$  nm  $\times$   $7.0$  nm). (b) 2D FFT of image (a) revealing two circles. (c) Fourier back-transform of the inner FFT circle showing the porous morphology of the silica film. (d) Fourier back-transform of the outer FFT circle resolving the atomic protrusions.

If we look at Figure 4.11d, depicting the Fourier back-transformation of the outer FFT circle, the origin of this circle becomes obvious. The back-transform of the outer FFT circle only reproduces the atomic protrusions of the Si atoms from the STM image. Consequently, the outer circle's  $1/k$  value of  $3.0$  Å perfectly matches the Si–Si NN distance (compare with Figure 4.4b).

## 4.5 Range IV: Longer Range Density Fluctuations

To study the order of range IV, the 2D mass density of the silica film was evaluated (Figure 4.12). The atomic model from Figure 4.8b was used as a basis for the density determination (green wireframe in Figure 4.12). Beneath

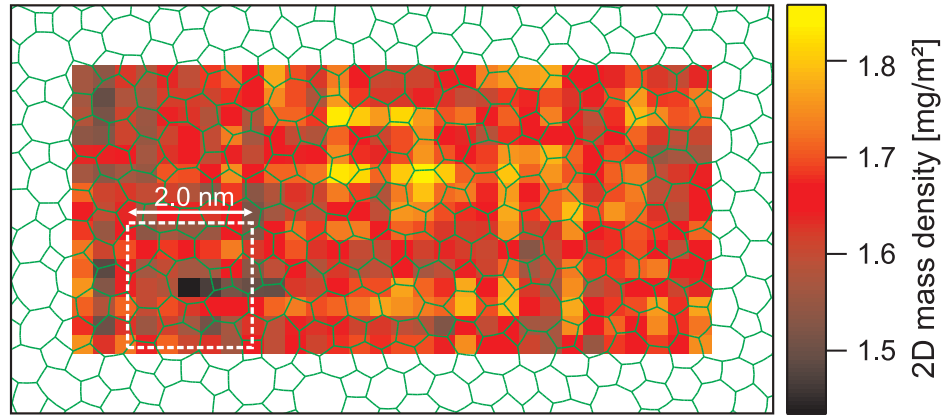


**Figure 4.12:** Analysis of the silica film’s 2D mass density. The green wireframe corresponds to the model from Figure 4.8b. The colored boxes are a real space representation of the 2D mass density (see scale bar). The white dashed box displays the bilayer slab used to calculate the 2D mass density.

the wireframe, small colored boxes depict the 2D mass density in  $\text{mg}/\text{m}^2$  (box size =  $0.34 \text{ nm} \times 0.30 \text{ nm}$ ; see scale bar in Figure 4.12). For every small box, the 2D mass density of a  $2 \text{ nm} \times 2 \text{ nm}$  slab around it was calculated (white dashed square in Figure 4.12). The size of the slab was chosen large with respect to the typical ring size. The slab comprises the whole bilayer structure, i.e., not only the topmost  $\text{SiO}_4$  tetrahedra, but also the lower ones.

We found that the 2D mass density varied from 1.46 to  $1.83 \text{ mg}/\text{m}^2$ . The total 2D mass density amounted to  $1.65 \text{ mg}/\text{m}^2$ , which is just twice the 2D mass density of graphene [180]. Evidently, the 2D mass density locally fluctuates. This most probably originates from the local ring environment: an area with large rings has a lower density than an area consisting of smaller rings. This way, the 2D mass density is lower in the lower left corner of the model, and higher towards the center of the image, which is dominated by smaller rings, i.e. four- to sevenfold rings.

## 4.6 Summary

In this chapter, the determination of the atomic surface structure of the vitreous silica film was presented. We used atomically resolved nc-AFM and STM images to characterize the atomic arrangement in detail. The images revealed a ring network resembling Zachariasen’s famous continuous random network. First, an atomic model of the topmost surface layer was developed from the observed protrusions in the images. Afterwards, we fol-

lowed the classification introduced by A.C. Wright who divided the order in network solids in four ranges: (I) structural unit, (II) interconnection of adjacent structural units, (III) network topology, and (IV) longer range density fluctuations. Range I revealed a well-defined structural unit, i.e., the  $\text{SiO}_4$  tetrahedron, with distances and angles corresponding to XRD and ND measurements on bulk vitreous silica. In range II, we found the first difference between the vitreous film and 3D silica glass, namely the Si–O–Si angle distribution, which exhibited a sharp edge in our case. This feature was assigned to the restricted dimensionality of the flat film. The most intriguing properties, however, were found in range III. The evaluation of pair distance histograms and pair correlation functions showed good agreement with results from XRD and ND on bulk vitreous silica, even for higher radial distances. By further evaluating the network topology, we found an asymmetric ring size distribution with pore sizes ranging from fourfold to ninefold rings; the six-membered ring was found to be the most frequent one. Our measured distribution of rings exhibited a characteristic log-normal shape, which originates from the connectivity requirement in 2D random networks as pointed out by Shackelford. In addition, the Si–Si–Si angle distribution and a Fourier transformation were analyzed for further insights into range III. An evaluation of range IV suggested that the local 2D mass density is determined by the ring environment.





# Chapter 5

## Comparison of Crystalline and Vitreous Phases

In the previous chapter, we presented atomically resolved nc-AFM and STM images of a bilayer of vitreous silica that was prepared on a Ru(0001) support. As outlined in section 3.2, we could grow vitreous silica films or films with coexisting crystalline and vitreous regions. In this chapter, the atomic structure of silica films exhibiting crystalline and vitreous phases is addressed and compared to each other. The positions of Si and O atoms were resolved on both phases. On the basis of these atomically resolved images, we present a detailed structural analysis including characteristic distances, orientations, and angles. Our measurements are compared to experimental and theoretical data from the literature. This chapter reflects the work published in Ref. [31].

### 5.1 Atomic Structure

In Figure 5.1, we present the analysis of crystalline and vitreous areas by STM including a comparison to Zachariasen's models. Figure 5.1a and d depict Zachariasen's 2D schemes of the atomic arrangement in a crystal and a glass, respectively (see also section 1.2). In both cases, the black dots represent the cations (A) and the white circles the O atoms. These atoms form well-defined  $\text{AO}_3$  units. In the crystalline structure, these building blocks are connected to a network with long range order consisting of sixfold rings only and a constant A–O–A angle of  $180^\circ$ . In contrast, in the glass, the  $\text{AO}_3$  units are connected via a large variety of A–O–A angles forming a so-called continuous random network. The ring size within this random network varies from four to eight.

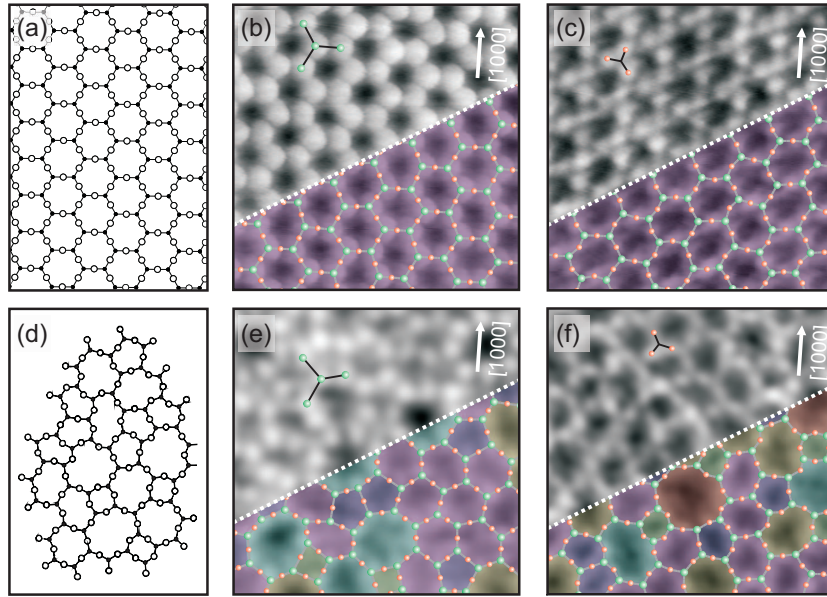


**Figure 5.1:** Atomic structure of crystalline and vitreous regions. (a,d) Zachariasen's schemes of the atomic arrangement in a crystal (a) and a glass (d) (from Ref. [3]). (b,c,e,f) Atomically resolved crystalline and vitreous regions of the thin silica film (the scan area of all images is  $3.5 \text{ nm} \times 3.5 \text{ nm}$ ). (b) STM image of a crystalline area showing the positions of Si atoms ( $V_S = 3.0 \text{ V}$ ,  $I_T = 100 \text{ pA}$ ). (c) STM image of a crystalline patch showing the arrangement of O atoms ( $V_S = 100 \text{ mV}$ ,  $I_T = 100 \text{ pA}$ ). (e) STM image of a vitreous area revealing the positions of Si atoms ( $V_S = 2.0 \text{ V}$ ,  $I_T = 50 \text{ pA}$ ). (f) STM image of a vitreous area showing the arrangement of O atoms ( $V_S = 100 \text{ mV}$ ,  $I_T = 100 \text{ pA}$ ). (b,c,e,f) Arrows indicate one crystallographic axis of the Ru(0001) substrate. Green balls represent the Si atoms, red balls the O atoms.

Figures 5.1b, c, e, and f display atomically resolved STM images with a size of  $3.5 \text{ nm} \times 3.5 \text{ nm}$ . Figures 5.1b and c were measured above a crystalline phase and Figures 5.1e and f on vitreous regions of the silica bilayer film. Both phases show ring networks resembling Zachariasen's schemes.

We were able to resolve the atomic structure of the topmost Si (Figures 5.1b and e) and O atoms (Figures 5.1c and f). This can be verified by examining the NN configurations of the imaged protrusions (see top part of Figures 5.1b, c, e and f). In Figures 5.1c and f, every *three* protrusions (red balls) form a three-bladed windmill shape representing one triangular face of an  $\text{SiO}_4$  tetrahedron. Therefore, these positions correspond to O atoms. However, in Figures 5.1b and e, *four* protrusions (green balls) form a three-bladed windmill with one protrusion sitting in its center. These positions represent the centers of four different tetrahedra and therefore correspond to

the Si atoms. Furthermore, the NN distances are characteristic for a certain atom type and are significantly larger for Si than for O (see also Table 5.1). Note that the observed chemical sensitivity of STM strongly depends on the microscopic tip configuration.

All STM images in Figure 5.1 are superimposed by an atomic model in the bottom right corner (Si: green, O: red). To find the O coordinates from the measured Si positions in Figures 5.1b and e, we calculated the center between each pair of Si NNs and defined this as the O position. A Si–O height difference ( $\Delta z_{\text{Si-O}}$ ) of 0.52 Å was assumed in this case. This number has been obtained in DFT calculations of the crystalline bilayer film [28]. In contrast to this procedure, the Si positions were computed self-consistently from the O coordinates in Figures 5.1c and f without assuming a fixed  $\Delta z_{\text{Si-O}}$ . For this purpose, first, a circumscribed circle was calculated for every triangle of O NNs (see Figure 4.2a). Afterwards, the circle center was defined as the Si position. Finally, for every  $\text{SiO}_4$  tetrahedron,  $\Delta z_{\text{Si-O}}$  was set to the radius of its insphere  $r_{\text{in}} = \bar{r}_{\text{O-O}}/\sqrt{24}$ , with  $\bar{r}_{\text{O-O}}$  being the average O–O NN distance in this particular  $\text{SiO}_4$  unit. Via this procedure, an average  $\Delta z_{\text{Si-O}}$  of  $0.55 \text{ \AA} \pm 0.04 \text{ \AA}$  and  $0.53 \text{ \AA} \pm 0.04 \text{ \AA}$  was obtained for the crystalline (Figure 5.1c) and the vitreous structure (Figure 5.1f), respectively. These heights are in good agreement with the DFT value of  $\Delta z_{\text{Si-O}}$ , justifying the use of the latter in the Si case and in the previous chapter.

To visualize rings of different size, the pores were color coded in Figure 5.1. Clearly, the crystalline phase is built up from only one ring type, namely the six-membered ring (a ring consisting of six Si and six O atoms). On the contrary, the vitreous phase is constructed from differently sized pores ranging from four- to nine-membered rings (see section 4.4 for a typical ring size distribution histogram). The atomically resolved images from Figure 5.1 served as the basis for further evaluation of the silica film’s structure.

## 5.2 Directed Distance Orientations

By carefully looking at the crystalline phases in Figures 5.1b and c, it appears that the imaged structures are not perfectly crystalline. Exactly this issue is addressed in the current section. In Figure 5.2, characteristic atomic orientations are evaluated. A quantity that reflects the order of a particular film region, is the directed distance orientation (DDO) between two atoms, i.e. the slope of a line segment connecting two atoms with respect to a certain fixed axis (here, we used the image ordinate as a reference).

Figure 5.2a visualizes the O–O NN DDOs of the crystalline region from Figure 5.1c using colored bars. The color scale represents the DDO value

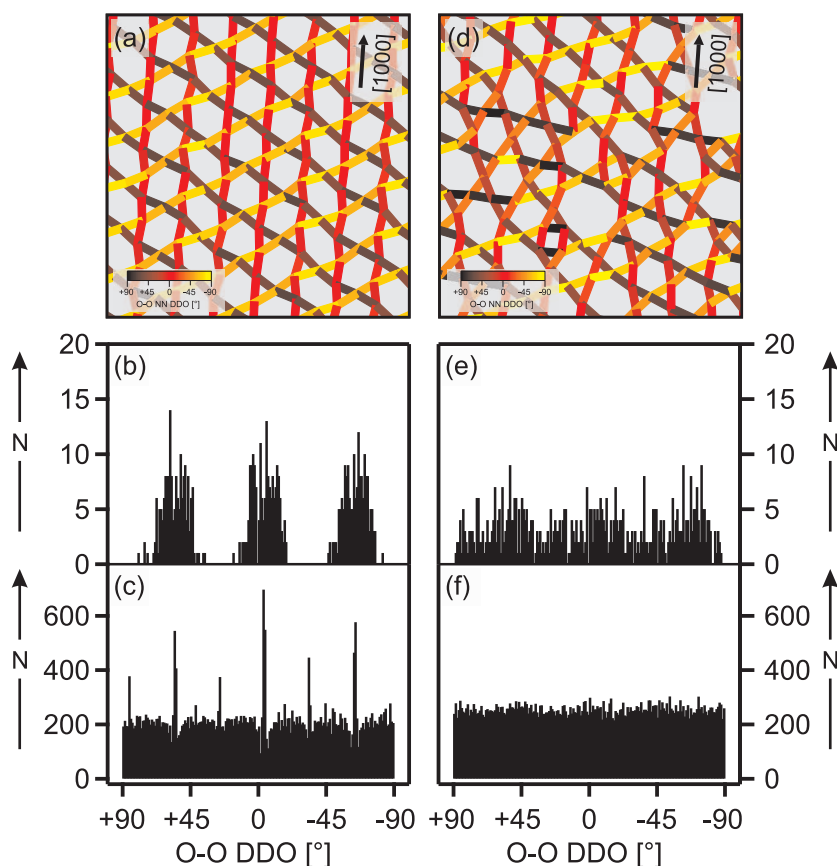


**Figure 5.2:** Analysis of the O–O directed distance orientations (DDOs). (a) The O–O NN orientations of the STM image in Figure 5.1c (crystalline structure) are represented by colored bars (see scale bar; image size = 3.5 nm × 3.5 nm). (b) A histogram of the O–O NN DDOs. These orientations represent the threefold symmetry of the crystalline phase. (c) A histogram of all O–O DDOs. Additionally to the NN peaks, second NN peaks are present. (d) O–O NN orientations of the STM image from Figure 5.1f (vitreous structure). Colored bars represent the DDO value (see scale bar; image size = 3.5 nm × 3.5 nm). (e) A histogram of the O–O NN DDOs. (f) The histogram of all O–O DDOs exhibiting a completely random distribution of angles. For the evaluation of (b), (c), (e), and (f) slightly larger surface areas were used (5 nm × 5 nm). (a,d) Arrows indicate one crystallographic axis of the Ru(0001) substrate.

(see scale bar). Apparently, three different orientations are present in this crystalline area. For a better visualization of the DDO distribution in this region, a histogram of the O–O NN DDOs is plotted in Figure 5.2b. Due to the threefold symmetry of the crystalline silica bilayer, we observe three peaks in the orientational distribution. The peaks are centered at  $+55.2^\circ$ ,

$-4.3^\circ$ , and  $-64.7^\circ$  and have equal peak heights. Surprisingly, the peaks are quite broad and have an average standard deviation of  $8.6^\circ$ . There are two possible explanations for this experimental result: (1) the determination of the atomic positions is not exact enough and/or (2) the crystalline region is not perfectly ordered. As we show in Appendix A, the deviation resulting from effect 1 was quantified by determining the atomic positions of a perfectly crystalline structure as a benchmark. The DDO error that stems from the manual determination of atomic coordinates should not be larger than  $1.7^\circ$ . Thus, effect 1 is weak. Therefore, we conclude that some regions consisting of hexagonal rings only are not perfectly crystalline. This residual disorder might be induced by a closely situated vitreous area. A detailed discussion about the influence of a vitreous region on the crystalline phase and the crystalline–vitreous interface can be found in chapter 6. Furthermore, the network structure might allow additional degrees of freedom and lead to certain distorted structures, which are close in energy.

Finally, Figure 5.2c displays the histogram of all O–O DDOs in the crystalline region, i.e. not only NN DDOs, but also DDOs between higher order neighbors. In this distribution we observe six sharp peaks on a large background. The three largest peaks can be identified as the average orientations of O–O NN rows, centered at  $+55.2^\circ$ ,  $-3.8^\circ$ , and  $-64.2^\circ$  (compare with Figure 5.2b). These sharp peaks verify the long range order of the crystalline phase. Moreover, these three main orientations are parallel to the crystallographic axes of the Ru support. The other three peaks represent the mean O–O second NN directions at  $+85.5^\circ$ ,  $+25.7^\circ$ , and  $-33.8^\circ$ . In a perfect crystalline structure, DDO peaks originating from third and higher order NNs are visible (see Appendix A). However, these peaks are not present in Figure 5.2c, being another indication for the residual disorder of this crystalline region.

A similar evaluation of pair orientations for the vitreous area from Figure 5.1f is presented in Figures 5.2d to f. The O–O NN DDOs are displayed in Figure 5.2d as colored bars (see scale bar). The DDO values of the vitreous state assume a large variety of values. This can be seen more clearly in Figure 5.2e, showing the O–O NN DDO histogram for the vitreous structure. The orientations are distributed over the whole range of  $-90^\circ$  to  $+90^\circ$  and separated peaks are absent. Several little peaks seem to be present in the distribution. However, after a careful analysis of several other images, showing a completely random distribution of NN orientations (see Appendix A), we ascribe the wavy structure in Figure 5.2e to the small size of the statistical probe in that case. The evaluation of DDOs between all atoms in the model reveals the true vitreous state of this region (see Figure 5.2f). In the histogram peaks are absent, demonstrating the lack of long range orientational order. The combination of a narrow distribution of NN distances and this

orientational disorder leads to the outer LEED and FFT circle (Figures 3.6a and 4.11b), which were described in the previous chapters.

One important aspect in this context is the interaction with the substrate. In the crystalline regions, the regular arrangement of silica pores follows the crystallographic orientations of the Ru substrate (see Figure 5.1b and c). However, the vitreous structures lack symmetry and periodicity and are therefore structurally decoupled from these axes. The weak coupling to the substrate might be one of the driving forces for the formation of vitreous patches. Huang and coworkers have also observed crystalline and vitreous silica bilayer patches on one and the same, crystalline substrate (graphene) [35]. Defects at the interface might be another influence on the film structure. It is important to note that in our nc-AFM and STM measurements, we observe only the top part of the bilayer, i.e. information on the interface is not attainable.

### 5.3 Distances and Angles

As introduced by Wright, the structural order in a network solid, like vitreous silica, can be divided into four ranges [5, 52] (see section 1.4). In this chapter, we will focus on the ranges I–III.

Table 5.1 shows an overview of distances and angles characterizing the ranges I, II and III in the topmost Si and O atoms of the crystalline and vitreous silica films. As a measure of range I, Table 5.1 includes the Si–O NN distance, the O–O NN distance and the O–Si–O mean angle. Furthermore, the Si–Si NN distance and the mean Si–O–Si angle are given, as they determine order of range II. Finally, Table 5.1 specifies one range III parameter, namely the Si–Si–Si angle, which defines the ring structure inside a network. We fitted our data with a Gaussian and the values in Table 5.1 represent the mean  $\pm$  standard deviation. Note that only values followed by an asterisk were directly measured in this study. In addition, in Table 5.1, the STM results are compared to distances and angles from the literature. The data of the crystalline film is confronted with (1) XRD of  $\alpha$ -quartz [181, 182], (2) ND of  $\alpha$ -quartz [183, 184], and (3) *ab initio* simulations of  $\alpha$ -quartz [185, 186]. Moreover, we compare values from the 2D vitreous silica film to (1) XRD of 3D vitreous silica [59], (2) ND of 3D vitreous silica [53], (3) *ab initio* calculations of 3D vitreous silica [100], and (4) the Bell and Dean handmade model of 3D vitreous silica [77].

The characteristic range I distances (Si–O and O–O) of the crystalline silica film agree well within the standard deviation with XRD, ND and *ab initio* results of  $\alpha$ -quartz. The same is true for the intratetrahedral angle

**Table 5.1:** Overview of characteristic distances determining structural order of range I, II and III. STM results from this study are compared to results from XRD, ND, and *ab initio* simulations on  $\alpha$ -quartz and bulk vitreous silica, as well as the handmade model of Bell and Dean for vitreous silica.

<i>crystalline</i>	STM <sup>a</sup>	STM <sup>b</sup>	XRD <sup>c</sup>	ND <sup>d</sup>	<i>ab initio</i> <sup>e</sup>	
Si-O [Å]	1.67 ± 0.08	1.66 ± 0.06	1.61	1.61	1.61-1.62	
O-O [Å]	2.71 ± 0.18*	2.72 ± 0.11	2.63-2.65	2.63	2.62-2.65	
O-Si-O [°]	109.4 ± 8.1	110.1 ± 5.7	108.8-110.5	108.7-110.5	108.5-110.2	
Si-Si [Å]	3.12 ± 0.08	3.15 ± 0.11*	3.06	3.06	3.07	
Si-O-Si [°]	139.9	143.5	143.7	143.6	144-148	
Si-Si-Si [°]	120.2 ± 6.3	119.5 ± 6.9*				
<i>vitreous</i>	STM <sup>a</sup>	STM <sup>b</sup>	XRD <sup>f</sup>	ND <sup>h</sup>	<i>ab initio</i> <sup>i</sup>	B&D <sup>j</sup>
Si-O [Å]	1.60 ± 0.09	1.61 ± 0.11	1.62	1.61 ± 0.05	1.61-1.63	1.59 ± 0.03
O-O [Å]	2.59 ± 0.21*	2.65 ± 0.19	2.65	2.63 ± 0.09	2.63-2.67	2.60 ± 0.08
O-Si-O [°]	109.2 ± 10.9	109.4 ± 12.6	109.8	109.7 ± 4.5	109.3-109.5	109.4 ± 4.9
Si-Si [Å]	3.01 ± 0.12	3.07 ± 0.23*	3.12	3.08 ± 0.11	3.03-3.12	3.11 ± 0.07
Si-O-Si [°]	140.5	142.6	144 (152 <sup>g</sup> )		143.4-152.2	154.2 ± 9.3
Si-Si-Si [°]	120.2 ± 14.7	118.8 ± 15.3*				104.9 ± 17.8
Si-Si-Si <sup>#</sup> [°]	119.9 ± 10.6	119.9 ± 13.2*				

\* directly measured values, this study

# six-membered rings only

<sup>a,b</sup> values given are the mean ± standard deviation from a Gaussian fit to the data

<sup>a</sup> STM with O structure, this study (Figures 5.1c and f)

<sup>b</sup> STM with Si structure, this study (Figures 5.1b and e)

<sup>c</sup> from Refs. [181, 182]

<sup>d</sup> from Refs. [183, 184]

<sup>e</sup> from Refs. [185, 186]

<sup>f</sup> from Ref. [59]

<sup>g</sup> re-analysis of the same data; from Ref. [60]

<sup>h</sup> from Ref. [53]

<sup>i</sup> from Ref. [100].

<sup>e,i</sup> the given ranges represent results from different basis sets

<sup>j</sup> calculated from the coordinates in Ref. [77]

(O–Si–O). Furthermore, we observe good agreement of the intertetrahedral angle (Si–O–Si) and the Si–Si distance. The Si–O–Si angle obtained from STM images with O and Si structures are slightly different (139.9° vs. 143.5°). This is connected with the different ways of calculating the height difference between Si and O in both cases, which was mentioned above.

The range I and II distance values for the vitreous silica film show also good agreement with XRD and ND, as well as with the handmade model and

*ab initio* simulations. The O–Si–O angle exhibits in all six vitreous cases nearly the same magnitude and approaches the mathematical tetrahedral angle of  $109.47^\circ$ .

In the vitreous case, there is a discrepancy between the Si–O–Si angle obtained from STM and literature values on 3D silica. The Si–O–Si is an important angle for the connectivity of the network structure. The difference in the Si–O–Si angle in 2D and 3D vitreous networks has already been discussed in section 4.3.

By comparing the values of crystalline and vitreous silica films, we note that range I and II distances are slightly larger in the crystalline case. However, this effect is only about 3 % and is negligible within the standard deviation. Furthermore, in an evaluation of the distances on both sides of a crystalline–vitreous interface in the thin silica film we did not observe any significant difference of the atomic distances (see chapter 6). If we concentrate on the directly measured distances with STM (O–O and Si–Si), we see that the standard deviation of the O–O NN distance distribution is nearly equal in the crystalline and the vitreous case ( $0.18 \text{ \AA}$  vs.  $0.21 \text{ \AA}$ ). This result is in line with the identical tetrahedral shape of crystalline and vitreous building blocks. In contrast, the standard deviation of the Si–Si NN distance distribution is larger for the vitreous structures than for the crystalline ones ( $0.23 \text{ \AA}$  vs.  $0.11 \text{ \AA}$ ). This effect stems from the larger distribution of possible intertetrahedral angles (Si–O–Si) in the vitreous film, enabling a larger variety of Si–Si NN distances.

It is in range III, where considerable differences between crystalline and vitreous structures are found. One range III parameter is the Si–Si–Si angle, which can be directly measured from STM images resolving the Si positions (Figures 5.1b and e). In the imaged crystalline phase, the Si–Si–Si angle has a mean value of  $119.5^\circ$ . As the crystalline structure consists of sixfold rings only, this angle agrees well with the  $120^\circ$  angle in a regular hexagon. In the vitreous phase, we observed ring sizes ranging from four to nine. For regular polyhedra with four to nine corners, angles ranging from  $90^\circ$  to  $140^\circ$  are allowed. Correspondingly, we measured Si–Si–Si angles ranging from  $80^\circ$  to  $170^\circ$ . The most common ring type in the vitreous phase is the six-membered ring. This fact explains that the vitreous structure yields a mean Si–Si–Si angle of  $118.8^\circ$ . The difference between crystalline and vitreous regions can be found in the width of the Si–Si–Si angle distribution. The standard deviation of the vitreous phase is larger than for the crystalline case by a factor of 2. Furthermore, it is interesting to note that even the sixfold rings in the vitreous phase have a broader Si–Si–Si angle distribution than the crystalline film. We conclude that sixfold rings exhibit a larger deformation in vitreous regions than in crystalline ones. In 3D, rings and loops are not



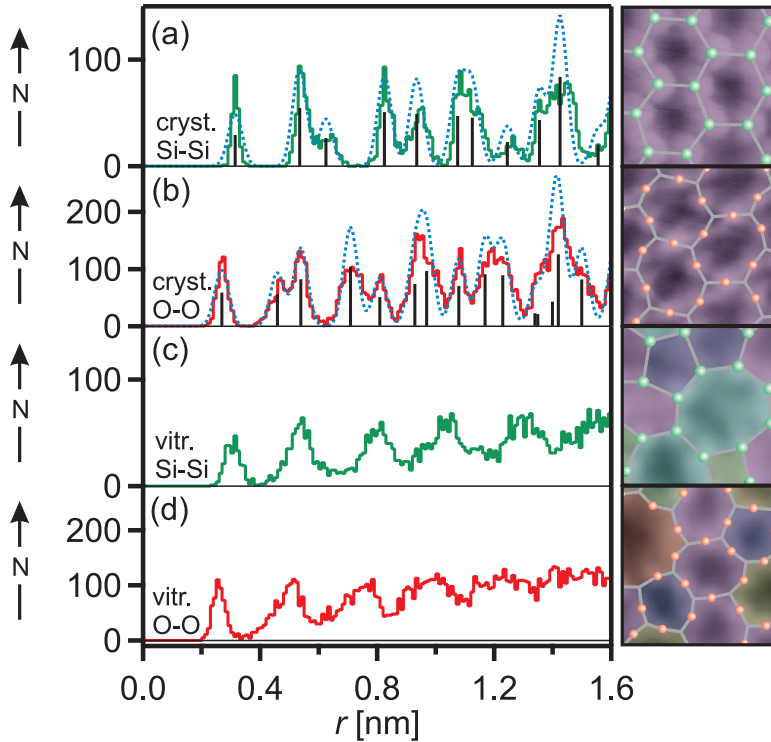


**Figure 5.3:** PDHs of crystalline and vitreous phases of the silica film. (a) Si–Si PDH of a crystalline patch. The black lines represent Si–Si distances from the DFT silica bilayer model. [28] The blue dotted curve shows the artificially broadened DFT PDH. (b) O–O PDH of a crystalline region. As in panel (a), the black lines and the blue dotted curve represent the DFT values. (c) Si–Si PDH of the vitreous phase. (d) O–O PDH of a vitreous area of the film. For panels (a)–(d), 5 nm × 5 nm images were evaluated. Image cutouts at the right show local coordination of atoms (green balls: Si, red balls: O; cutout size: 1.3 nm × 1.3 nm).

limited to a planar shape, and therefore a different Si–Si–Si angle distribution has been predicted ( $106^\circ \pm 20^\circ$ ) [88].

## 5.4 Pair Distance Histograms

To quantify the structural order of range III, Figure 5.3 presents the O–O and Si–Si PDH of crystalline and vitreous areas in the silica film. The 1D PDHs from Figures 5.3a–d were extracted from atomically resolved STM images with equal size (scan ranges: 5 nm × 5 nm; cutouts shown in Figure 5.1b, c, d, and f). Radial distances ( $r$ ) up to 1.6 nm were evaluated. At the right side of Figure 5.3, model cutouts display the local order and coordination

of the corresponding atom type for every PDH curve (green balls: Si, red balls: O; image size:  $1.3 \text{ nm} \times 1.3 \text{ nm}$ ). For a better peak interpretation of the crystalline PDHs, we plotted the PDH of the DFT model for the crystalline silica bilayer [28] (black bars in Figure 5.3a and b). Evidently, the experimental curves are much broader than the DFT PDH, but they agree well with the artificially broadened DFT peaks (blue dotted curves in Figure 5.3a and b). Similar to the discussion of Figure 5.2, the reason for this broadening might be twofold: (1) experimental uncertainty and/or (2) minor disorder of the crystalline phase. As we show in Appendix A, effect 1 should be in the range of  $\pm 0.08 \text{ \AA}$  for the first crystalline peak in the O–O distribution. However, the standard deviation of the first O–O peak in Figure 5.3c is  $0.18 \text{ \AA}$ , which means that only half of the broadening can be explained by reason 1. Thus, Figures 5a and c give another indication for the residual disorder of the crystalline region.

Although the experimental crystalline distance distributions exhibit broadening, the PDHs of the crystalline (Figure 5.3a and b) and the vitreous regions (Figure 5.3c and d) clearly exhibit several differences: (1) the vitreous peaks are in general broader and have a lower intensity than the crystalline ones, (2) the vitreous peaks become broader and more diffuse with increasing  $r$ , and (3) the background of the curves is more pronounced in the vitreous case. It is noteworthy that in the vitreous PDHs, peaks can be identified up to about  $2 \text{ nm}$ , which is in good agreement with the estimated distance up to which order can extend in bulk vitreous silica [54, 55]. The PDH of an extended 2D Zachariassen scheme [78, 79] also shows peaks up to radial distances of at least  $2 \text{ nm}$  (see Appendix A). 2D vitreous networks might have an even longer correlation length than bulk glasses, as the 3D structure has more degrees of freedom and there are more possibilities to lose order [187].

## 5.5 Summary

In this chapter, we investigated the atomic structure of crystalline and vitreous regions in the silica bilayer film on Ru(0001). The atomic arrangement of Si and O atoms could be resolved for both cases. Some crystalline regions exhibit minor effects of disorder, which can be attributed to the flexible network structure. The evaluation of characteristic distances and angles showed good overall agreement with diffraction data and simulated networks. Even the extension of order is similar for the 2D and 3D vitreous structures.

# Chapter 6

## Crystalline–Vitreous Interface in Two-Dimensional Silica

In this chapter, we report on a detailed evaluation of the 1D interface between a crystalline and a vitreous region of the thin silica film. The evolution of characteristic atomic distances and angles is analyzed in detail. We discuss how ring statistics change across such a border. A measure of the film’s crystallinity is introduced and we look at its development from the crystalline to the glassy phase. This chapter reflects the work published in Ref. [33].

### 6.1 Motivation

The topological transition from a crystalline to an amorphous material can result in very complex structures. It is a demanding task to investigate the atomic arrangement in such boundaries and it requires a well-defined structural model system. Understanding the interface between a crystal and a glass can lead to a better description of the crystal-to-glass and the liquid-to-glass transitions. In addition, fundamental knowledge about semicrystalline materials can be gained, because there the crystallites are separated by disordered boundary regions.

A vast amount of studies have been published concerning crystalline–amorphous (*c/a*) interfaces of different, mostly tetrahedrally coordinated materials, including *c*-Ge/*a*-Ge [188], *c*-Si/*a*-Ge [189, 190], *c*-Si/*a*-Si [188, 191–194], *c*-Al<sub>2</sub>O<sub>3</sub>/*a*-CaSiO<sub>3</sub> [195], *c*-β-Si<sub>3</sub>N<sub>4</sub>/*a*-SiO<sub>2</sub> [196], and *c*-Si/*a*-SiO<sub>2</sub> [197–208], the last example being an important interface in semiconductor technology. The transitional structures were investigated by a large variety of theoretical [188, 191, 193, 195, 201, 203, 204, 206] and experimental methods [189, 190, 192, 196–200, 202, 205, 207, 208]. However, the interface between

crystalline and vitreous silica has not been addressed so far. Moreover, the application of SPM to a  $c/a$ -transition has not been shown. These structures were thought to be inaccessible by SPM, because the interfaces are buried inside the bulk materials [190].

In chapter 3 and 5, we showed that the silica film can be grown with coexisting crystalline and vitreous regions. The silica film on Ru(0001) provides the unique opportunity to study the interface between crystalline and vitreous growth modes with atomic resolution in real space.

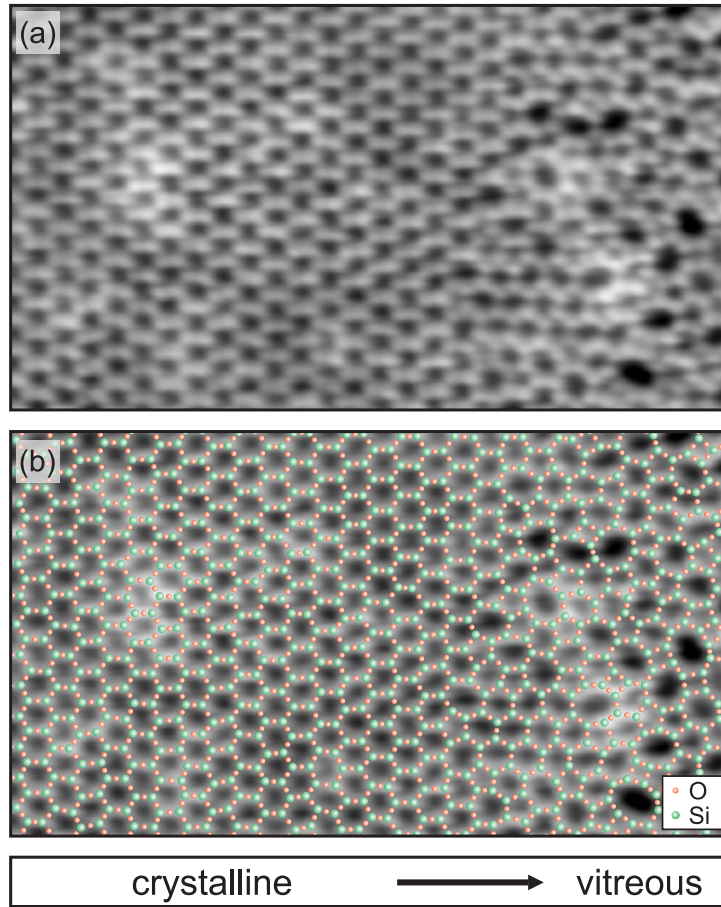
## 6.2 Atomic Structure

Figure 6.1a shows an atomically resolved STM image of a crystalline–vitreous transition region in the silica film. The porous structure of the bilayer film is clearly visible. Furthermore, every pore exhibits well-resolved protrusions. Because every four bright spots are arranged in a three-bladed windmill shape, we assign these features to the positions of Si atoms. The coordinates of the O atoms were obtained by calculating the center between every pair of Si–Si NNs. The final atomic model of the film’s topmost layer is superimposed onto the STM image in Figure 6.1b (Si: green balls, O: red balls). This atomic model served as a starting point for further analysis of the crystalline–vitreous interface.

A closer look at the model reveals that the left part of the image consists of a regular and periodic arrangement of atoms. However, the right third of the image lacks periodicity and symmetry and is therefore vitreous. Later, we will define a quantity that gives a measure of the order in a particular film region.

It is important to note that we did not observe any electronic signature from the crystalline–vitreous interface in the STM under the given tunneling conditions (see e.g. Figure 6.1a). For the antiphase domain boundaries in ultrathin alumina on NiAl(110), pronounced electronic features have been observed, which were attributed to defect-induced states of the nonstoichiometric structure at the interface. [209] We therefore conclude an absence of such defect states at the crystalline–vitreous boundary of the thin silica film. There are also no under- or overcoordinated Si atoms, as all Si atoms have exactly three Si NNs (four NNs if one takes into account the Si atom of the first silica layer sitting underneath every Si atom of the second layer that is imaged). Thus, the stoichiometry and the vertical structure are conserved at the crystalline–vitreous transition. These considerations show that the vitreous patch is smoothly connected to the crystalline one.

To evaluate the transition between both regions, it is interesting to look



**Figure 6.1:** (a) Atomically resolved STM image of the crystalline–vitreous interface in the silica film ( $V_S = 2$  V,  $I_T = 100$  pA, scan area =  $12.3$  nm  $\times$   $7.0$  nm). (b) The STM image, superimposed by the atomic model of the topmost layer (Si green, O red). The bar below indicates the crystalline and the vitreous areas. The black arrow shows the direction of the interface analysis.

at the change of quantities that characterize the film’s structure as we move from the crystalline to the vitreous area. For this chapter, we investigated the NN distances, NN orientations, the 2D mass density and the ring statistics. It would be desirable, to evaluate these quantities perpendicular to the interface. However, it is difficult to define the exact boundary line, because it is impossible to say whether a sixfold ring belongs to the crystalline or the vitreous region, as they appear in both phases. Therefore, we chose to evaluate the interface structure by approaching it from a direction that is perpendicular to one crystalline axis (see black arrow below Figure 6.1b). The image was cut into vertical slices of constant width. Subsequently, the

characteristic quantities were computed for every slice separately.

### 6.3 Atomic Distances and 2D Mass Density

First of all, we evaluated the Si–Si NN distances to tell, how the atomic separations change at the interface between the crystalline and the vitreous phase. The distances of all Si–Si NN pairs were computed and are displayed in Figure 6.2a. Differently colored bars represent the magnitude of the Si–Si NN distance (see scale bar in Figure 6.2a). Figure 6.2a shows a homogeneous distribution of Si–Si NN distances throughout the whole image including the crystalline, the vitreous, and the interface region. For a better quantification of the Si–Si NN distance evolution, we divided the image into ten vertical, 1.23 nm wide slices and computed the distance distribution for every slice. Each distribution was fitted by a Gaussian, yielding mean values and standard deviations. Figure 6.2c shows a plot of these two quantities vs. the lateral coordinate of the respective slice ( $x$ ). Although the slices' mean values exhibit a slight variation of 0.003 nm around the average for the whole image ( $0.303 \text{ nm} \pm 0.025 \text{ nm}$ , dashed line), the deviation is not significant. Therefore, we conclude that the mean Si–Si NN distance stays constant as we go from the crystalline to the vitreous state. The NN distance is also not affected at the crystalline–vitreous transition region. This finding is consistent with experimental results on bulk silica materials: the average Si–Si NN distances in vitreous silica [53] and  $\alpha$ -quartz [181, 184] are equal within the root mean square variation of the glass ( $0.3077 \text{ nm} \pm 0.0111 \text{ nm}$  and  $0.3059 \text{ nm}$ , respectively). However, although the NN distance stays constant throughout the interface, the standard deviation slightly increases in the vitreous region (from 0.2 to 0.3 nm). This is in line with the separate evaluation of crystalline and vitreous regions in chapter 5.

Additionally, the atomically resolved interface enables us to compare the density of the crystalline and the vitreous phase. From the atomic model displayed in Figure 6.1b, we calculated the local 2D mass density. We used the same division of the image into ten slices as discussed before (Figure 6.2b). The 2D mass density vs. the respective slice center is plotted using red circles in Figure 6.2d. The observed oscillation in the crystalline phase is an artifact; it occurs because the vertical slices are parallel to one crystalline direction. Therefore, these slices sometimes comprise one, sometimes two silica rows, producing low and high density, respectively. Hence, the slice thickness is too small for the density evaluation. It is, therefore, better to examine the 2D mass density calculated for three slices of equal width (each 4.11 nm wide; see blue squares in 6.2d). This representation clearly shows

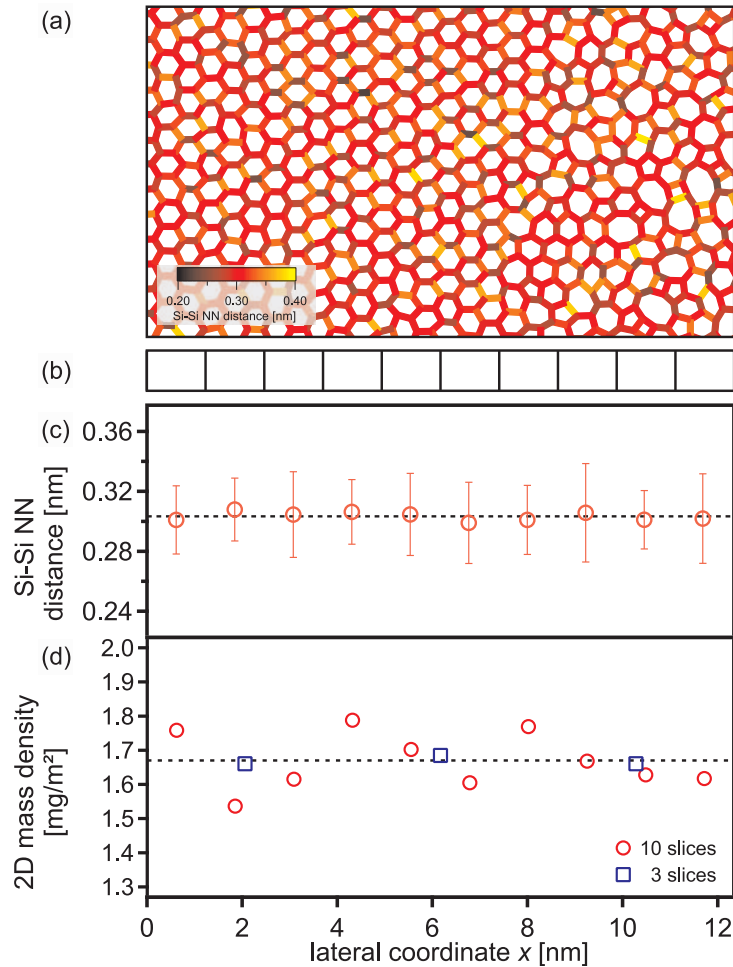


**Figure 6.2:** Evaluation of the Si–Si distances and the 2D mass density. (a) The Si–Si NN distances are visualized by colored bars. The color scale represents the distances between two Si atoms (see scale bar). (b) The position of ten vertical, 1.23 nm wide and 6.95 nm high slices. (c) The mean Si–Si NN distances for every slice are plotted vs. the lateral coordinate of the respective slice center ( $x$ ). Error bars represent the standard deviation of a Gauss fit to the distance distribution. The dashed line specifies the average value for the whole image ( $0.303 \text{ nm} \pm 0.025 \text{ nm}$ ). (d) The 2D mass density plotted vs.  $x$  for the ten slices as shown in panel (b) (red circles). The blue squares show the 2D mass density vs.  $x$  calculated for three slices of equal width (4.11 nm). The black dashed curve corresponds to the total 2D mass density of the presented area ( $1.67 \text{ mg/m}^2$ ).

that the surface densities of the crystalline and the vitreous phase are nearly equal and approach the value for the total image ( $1.67 \text{ mg/m}^2$ ; compare with section 4.5).

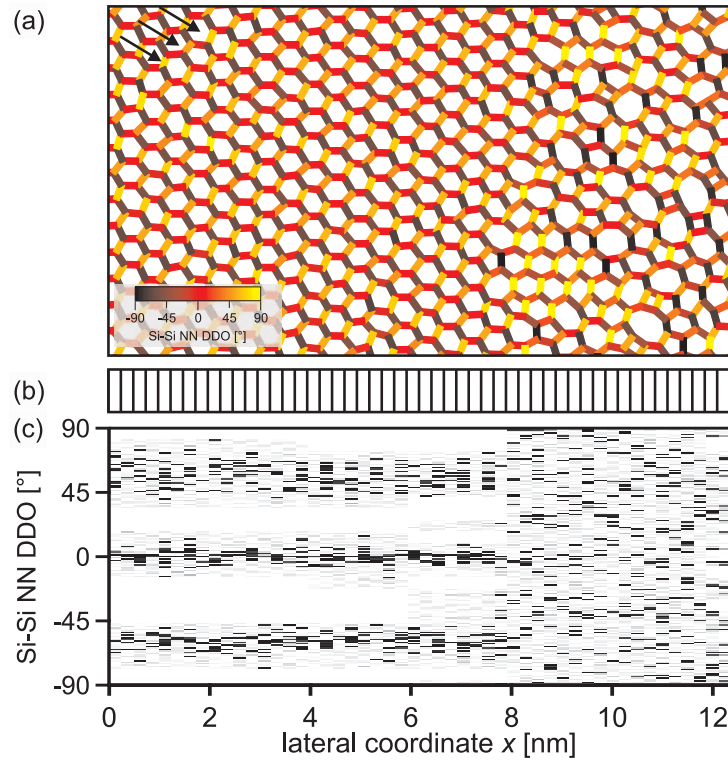


**Figure 6.3:** Evaluation of Si–Si NN DDOs. (a) The orientation of the directed Si–Si NN distances is displayed using different colors. The color scale indicates the orientation of Si–Si line segments with respect to the abscissa of the image plot (see scale bar). Arrows show examples of rows in the crystalline phase, where the DDOs slightly alternate. (b) The position of 50 vertical, 0.25 nm wide and 6.95 nm high slices. (c) DDO values for every slice plotted vs. the slice’s lateral coordinate.

## 6.4 Directed Distance Orientations

Another way of analyzing at the crystalline–vitreous interface is by exploring characteristic angles between the atoms of the silica film. A quantity that reflects the order of a certain region is the Si–Si NN DDO, which has already been introduced in section 5.2. In this chapter, the DDO is the slope of the connection line between two Si NNs with respect to the image abscissa. Figure 6.3a visualizes the different directions present in the film using colored bars. Si–Si NN DDO values range from  $-90^\circ$  to  $+90^\circ$  (see also the scale bar in Figure 6.3a). Clearly, the DDOs are different for the crystalline and the vitreous phase. This difference is demonstrated in Figure 6.3c, where the DDO values are plotted vs.  $x$  for 50 narrow slices. In the crystalline region



(left part of the STM image) DDOs assume three values:  $-60^\circ$ ,  $0^\circ$ , and  $+60^\circ$ . These three directions reflect the threefold symmetry of the crystalline structure. However, in the vitreous region (right part of the STM image) DDO values scatter randomly from  $-90^\circ$  to  $+90^\circ$ . This shows that in this area, the atoms are not collectively aligned. In addition, the representation in Figure 6.3c indicates the location of the interface region, namely around  $x = 8$  nm.

Surprisingly, in the crystalline region of Figure 6.3a, the NN orientations are not perfectly aligned to each other, but they rather seem to scatter around mean values. This is also visible in Figure 6.3c, where the crystalline peaks ( $x < 8$  nm) exhibit a certain width of roughly 20 to  $30^\circ$ . This is another expression of minor disorder in the crystalline region, which was already discussed in sections 5.2 and 5.4. In addition, row-like features of parallel DDOs can be identified in Figure 6.3a (see e.g. rows marked by black arrows). We exclude a drift-related effect, because the directions in these rows alternate from row to row. One possible explanation might be that the vitreous area induces stress into the crystalline phase, which is subsequently released via these rows.

## 6.5 Ring Size Distribution and Crystallinity

The final stage of the crystalline–vitreous interface evaluation is to examine larger objects than NN distances: the silica rings. By counting the number of Si atoms involved in every ring, we obtained a 2D distribution of ring sizes. Furthermore, to gain another quantity that characterizes the ring size, we calculated the areas of the polygons that are defined by the atoms of every ring.

In Figure 6.4a, all rings in the model were colored corresponding to their size. To see even small variations in the size distribution, the color scale is proportional to the rings' polygonal area (see scale bar). It becomes clear that the imaged area is not at all homogeneous. Whereas the film consists of only six-membered rings on the left side, rings of various size dominate the right third of the figure. Notably, even the six-membered rings of the crystalline area exhibit a variation in their polygon area. This stems from small deviations of NN distances and orientations leading to deformations of the rings.

Note that the transition region does not introduce any new elements into the film structure, e.g. large voids. The interface is solely constructed from ring types already known from the vitreous phase (see section 4.4).

To evaluate how the ring statistics evolve from the crystalline to the

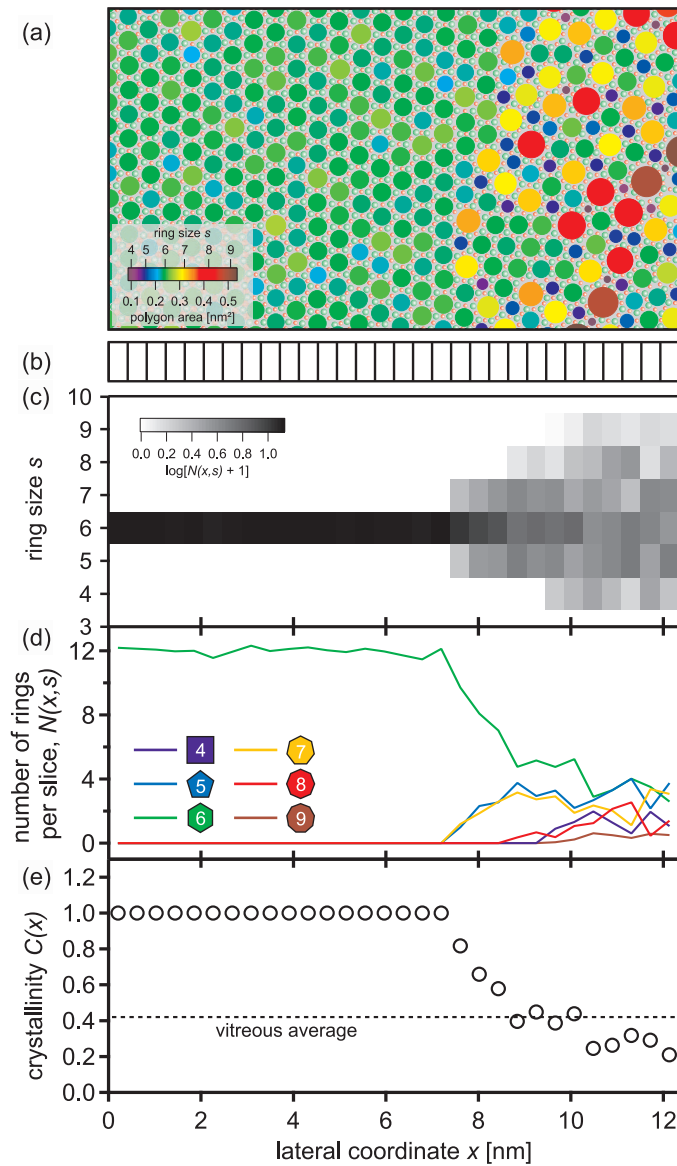


**Figure 6.4:** Analysis of the rings at the crystalline–vitreous interface of the silica film. (a) Visualization of the different ring sizes. Polygon areas range from  $0.1 \text{ nm}^2$  to  $0.5 \text{ nm}^2$  and ring sizes from four to nine Si atoms per ring (see scale bar). (b) The position of 30 vertical,  $0.41 \text{ nm}$  wide and  $6.95 \text{ nm}$  high slices. (c) The ring size distribution plotted for every slice. A logarithmic gray scale is used. (d) The number of rings per slice for every ring size plotted vs. the lateral coordinate. (e) The crystallinity of every slice plotted vs. lateral coordinate. The dashed horizontal line represents the overall crystallinity value of a vitreous region ( $C = 0.42$ ; see Figure 4.8d).

vitreous region, we divided the image into 30 vertical slices (each 0.41 nm wide; see Figure 6.4b). Afterwards, we computed ring size distributions for every slice, including ring fractions. Finally, we obtained the 3D data set

$$N(x, s), \quad (6.1)$$

where  $N$  is the amount of rings per slice,  $x$  the lateral coordinate of the respective slice, and  $s$  the amount of Si atoms per ring, i.e. the ring size. In Figure 6.4c, this 3D data set is plotted as a 2D graph. To obtain good contrast, the gray scale of the boxes represents the logarithm of the number of rings per slice,  $\log[N(x, s) + 1]$  (the +1 is added to avoid divergence at zero). Figure 6.4d is a slightly different way to visualize the data. In this graph,  $N(x, s)$  is plotted as a curve for every ring size separately (curve colors correspond to the color scale in Figure 6.4a).

The representations of Figure 6.4c and d show an interesting feature of the crystalline–vitreous interface: the first rings to appear close to the crystalline area other than six-membered rings are five- and seven-membered rings. In DFT calculations, the energy of isolated five- and sevenfold ring structures was found to be only slightly higher than the energy of the six-membered ring [29]. Furthermore, the formation of two fivefold and two sevenfold rings in the 2D film represents the smallest energy structural deviation from the crystalline phase [29]. This prominent four-rings structure is also known as the Stone-Wales defect [210] and was observed in Buckminsterfullerenes [211], in BN and C nanotubes [211, 212], in graphene [213–215], and in a  $\text{Cu}_2\text{O}$  thin film [216].

At increasing lateral coordinate, also four- and eightfold rings are found in the STM image of the silica film. The last ring to occur, is the ninefold ring, which represents the largest deviation from the presumably energetically most favorable six-membered ring [29].

To better quantify how the film transforms from the crystalline to a vitreous state, we define the crystallinity of a slice

$$C(x) = \frac{N(x, 6)}{\sum_{s=4}^9 N(x, s)}. \quad (6.2)$$

This quantity is plotted in Figure 6.4e. On the left side of the image ( $x \leq 7.2$  nm), where the film consists of sixfold rings only,  $C(x) = 1$ . As other ring types start to appear ( $x > 7.2$  nm),  $C(x)$  drops gradually to a value below 1. The dashed line in Figure 6.4e marks the reference crystallinity value for a large vitreous area ( $C = 0.42$ , based on the ring statistic from Figure 4.8d).

The  $C(x)$  plot shows that the thickness of the transition region from the crystalline ( $C(x) = 1$ ) to the vitreous area ( $C(x) = 0.42$ ) is approximately 1.6 nm. For the crystal–glass transitions of other 3D tetrahedral networks, interface widths of 0.3 to 1.4 nm were obtained theoretically [191, 193, 194, 201] and experimentally [190, 197, 207]. However, it is not straightforward to compare these values to our measurements because of the different interface system (silica–silica) and the different dimensionality of the boundary (2D vs. 1D). Furthermore, the thickness of the 1D interface in the silica film might be influenced by small crystalline patches enclosed in the vitreous structure that enhance the crystallinity of the transition region (see e.g. bottom right part of Figure 6.4a). As a recent paper shows, local crystallites might also be present in bulk glasses [217].

## 6.6 Summary

In this chapter, we studied the atomic structure of the topological transition from a crystalline to an amorphous phase in the thin silica film on Ru(0001). A smooth interface without under- and overcoordinated Si atoms was observed. The Si–Si distances appeared to remain constant in the crystalline, the vitreous, and the interfacial region. Similarly, the 2D mass density was equal in the crystalline and the vitreous phase. However, the orientation of the Si–Si directed distances showed a substantial change at the interface. Whereas in the crystalline area, the angular distribution exhibited three discrete peaks representing the crystalline axes, in the vitreous part the orientations were randomly distributed in all directions. Finally, ring statistics were computed for narrow image slices. It became evident that no new elements (e.g. voids) are present in the interface. Furthermore, this evaluation revealed that five- and sevenfold rings lie closer to the crystalline phase than four-, eight-, and nine-membered rings. Additionally, a thickness of the transition region of about 1.6 nm was obtained.

# Conclusion and Outlook

The presented work addresses the atomic structure of an ultrathin vitreous silica film on a Ru support. For the first time, it was possible to resolve the morphology of an amorphous system at the atomic scale. Detailed analysis and a comparison to crystalline regions of the same bilayer film unveiled the nature of this versatile model system.

The first and most essential step in this work was to characterize the growth of the silica film. For this purpose a combined state-of-the-art low temperature scanning tunneling and noncontact atomic force microscope was employed. Those results were accompanied by low energy electron diffraction and Auger electron spectroscopy to gain further information on the film morphology and the presence of certain chemical species. We found that the monolayer was always crystalline. Remarkably, the bilayer exhibited vitreous areas. By fine-tuning the coverage, we grew silica bilayers with coexisting crystalline and vitreous regions.

The next step of this work involved the determination of the atomic surface structure of the vitreous silica film. High resolution images revealed a ring morphology resembling Zachariasen's famous continuous random network. From the observed protrusions, an atomic model of the topmost surface layer was derived, serving as the basis for further analysis. The structure was characterized following Wright's classification of order in network solids into four ranges. The distances and angles in our model showed good agreement with diffraction results on bulk vitreous silica. The most intriguing feature of the bilayer film—the ring size distribution—was analyzed in detail. A log-normal distribution was detected. As pointed out by Shackelford and Brown, it originates from the connectivity requirement in two-dimensional random networks.

In chapter 5, we explored the atomic arrangement in crystalline and vitreous regions of the silica film. A complete evaluation of the experimentally resolved Si and O positions was presented. Some crystalline regions exhibited minor deviation from perfect order, which can be attributed to the flexible network structure. Furthermore, a detailed analysis of characteristic dis-

tances and orientations yielded good agreement with diffraction data and simulated networks. Correlation was found to extend up to 2 nm in vitreous networks.

The last chapter addressed the crystalline–vitreous interface in 2D silica. The Si–Si distance was found to remain constant throughout the transition region. The evaluation of atomic ring structures shed light on the interface structure. The first rings to appear close to the crystalline region were five- and sevenfold rings, followed by four- and eight-membered rings. The energetically least favorable ring, i.e. the ninefold ring, occurred only deep inside the vitreous region. Surprisingly, neither new elements nor under- or over-coordinated sites were found in the transition region. The thickness of the interface was estimated to be about 1.6 nm.

In summary, a detailed and comprehensive picture of the silica bilayer structure was developed. This model system provides the unique opportunity to study vitreous structures with a local technique at the atomic level. This work opens the way to further studies about the vitreous nature of this film. For example, it is of great interest to directly study the amorphization process. This can be achieved by high resolution electron microscopy. Furthermore, studying the interaction of the film with single adsorbates or molecules could clarify the properties of oxide materials used in industrial catalysis, which are usually also amorphous.

# Appendix A

## Supporting Information for Chapter 5

### Determination of DDO Errors

The atomic positions in Figures 5.1b, c, e, and f were determined manually. Evidently, this is a possible source of errors and broadening of peaks. In this section, we focus on the characterization of the error made by the manual determination of atomic positions. For this purpose, we compare three different crystalline silica structures: (a)  $5\text{ nm} \times 5\text{ nm}$  supercell of the DFT model of the crystalline film [28] as a benchmark for a perfectly crystalline arrangement of atoms, (b) manually determined positions on the basis of the DFT supercell, and (c) manually determined positions of a  $5\text{ nm} \times 5\text{ nm}$  STM image of the crystalline silica film (a cutout of this image is shown in Figure 5.1c). The result of the DDO error analysis is shown in Figure A.1. Figures A.1a-c give O–O NN DDOs for the three above mentioned structures. Apparently, the DDO peaks of the DFT supercell are extremely sharp, proving perfect orientational order (Figure A.1a). Figure A.1b shows the O–O NN DDO analysis for the manually determined positions on the basis of the DFT supercell. The peaks became broader than in the pure DFT case. On average, a Gaussian fit to the peaks had a standard deviation (SD) of  $1.7^\circ$ . However, the manually determined STM positions yielded peaks with an average SD of  $8.6^\circ$  (see Figure A.1c). Therefore, we conclude that the breadth of the experimental peaks can not only be explained by the manual determination of atomic coordinates. In Figures A.1d-f all O–O DDOs were evaluated from the three above mentioned structures. It is evident that the pure DFT supercell and the manually retraced DFT structure show more peaks than the manually determined STM positions. In addition, the back-

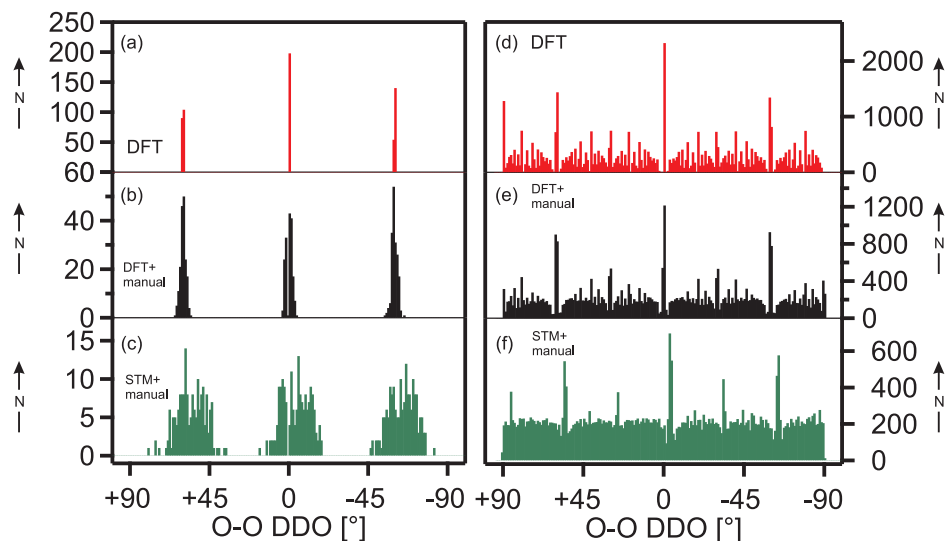


**Figure A.1:** Characterization of the error of manual evaluation of atomic positions and its influence on DDOs. (a–c) O–O NN DDOs. (d–f) All O–O DDOs. (a,d) DDOs calculated on the basis of a  $5 \text{ nm} \times 5 \text{ nm}$  supercell of the crystalline DFT structure from Ref. [28]. (b,e) DDOs calculated from positions that were obtained manually from the DFT structure. (c,f) DDOs calculated from positions that were obtained manually from a  $5 \text{ nm} \times 5 \text{ nm}$  STM image of a crystalline region in the silica film (cutout shown in Figure 5.1c).

ground is larger in the STM case. Hence, this evaluation suggests that the imaged crystalline region lacks perfect orientational and long range order.

## Determination of PDH Errors

To characterize the error made in the evaluation of PDHs, we follow the same route as described in the previous section. The O–O PDH of the DFT structure [28], the manually retraced DFT structure, and the manually determined STM positions are shown in Figures A.2a–c. The first DFT peak is very sharp with an SD of  $0.003 \text{ \AA}$ . The manual determination yields a first PDH peak that is much broader (SD =  $0.08 \text{ \AA}$ ) than the first DFT peak. However, the STM SD is  $0.18 \text{ \AA}$ , which can not originate purely from the manual determination error.



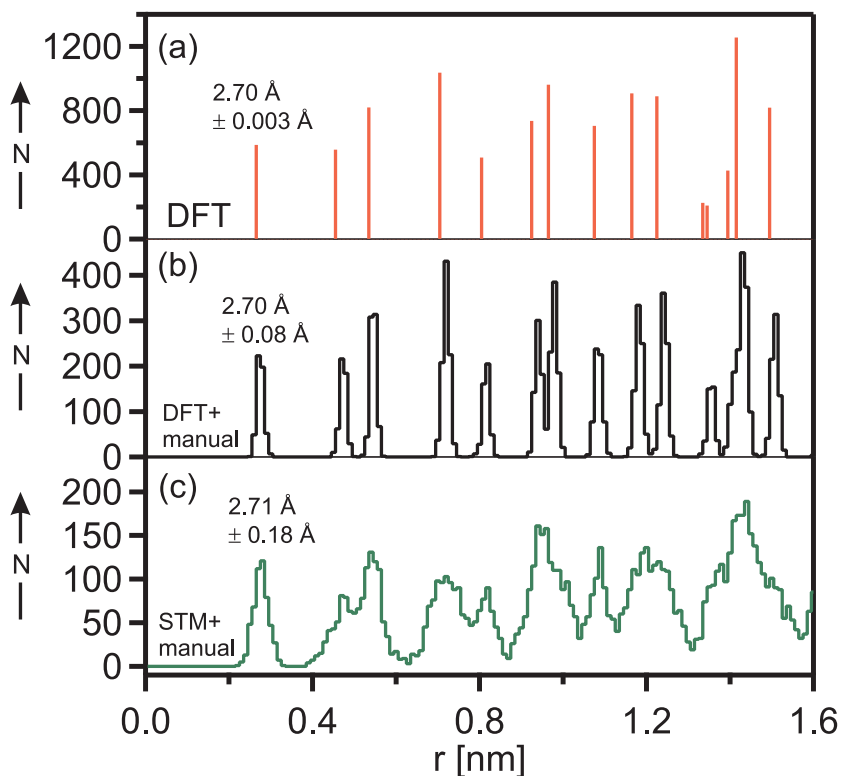


**Figure A.2:** Characterization of the error of manual evaluation of atomic positions and its influence on the PDH. (a) The PDH calculated on the basis of a  $5 \text{ nm} \times 5 \text{ nm}$  supercell of the crystalline DFT structure from Ref. [28]. (b) PDH on the basis of atomic positions that were manually determined from the DFT structure. (c) PDH on the basis of atomic positions that were manually determined from a  $5 \text{ nm} \times 5 \text{ nm}$  STM image of a crystalline region in the silica film (cutout shown in Figure 5.1c).

## DDO Evaluation of Multiple Images

To find out, whether the wavy structure in the O–O NN DDO distribution from Figure 5.2e is real or an artifact, we evaluated six other atomically resolved images of vitreous areas of the thin silica film. The total area sums up to over  $150 \text{ nm}^2$ . The summed histogram of O–O NN DDOs of these images is shown in Figure A.3. The plot reveals a completely random distribution of DDO values. Therefore, the little peaks in Figure 5.2e are an artifact of the small image size evaluated.

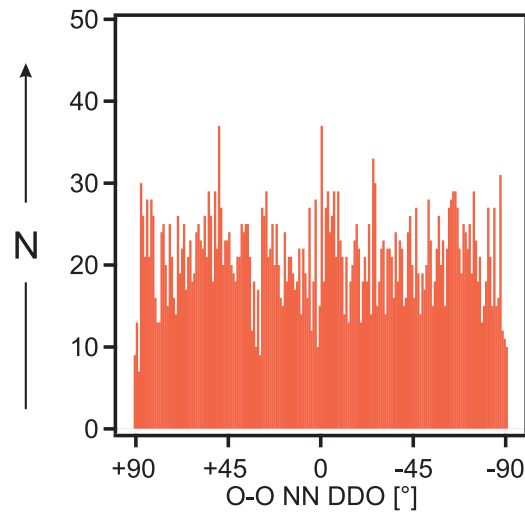


**Figure A.3:** O–O NN DDOs from six SPM images of vitreous regions of the silica film (scan area  $> 150 \text{ nm}^2$ ).

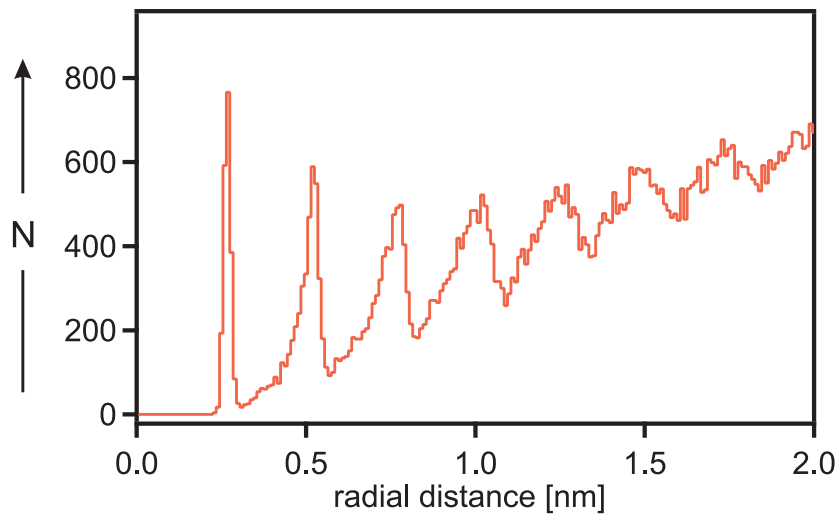


**Figure A.4:** PDF of an extended 2D Zachariasen scheme from [79]. The triangle edges were taken as the O positions and the mean O–O NN distance was set to 0.263 nm [53].

## PDF of an Extended 2D Zachariasen Scheme

To compare range III order in 2D vitreous networks, we evaluated an extended 2D Zachariasen scheme from Ref. [79]. This structure consists of corner-sharing triangles that are arranged in a random way. By assigning the edge positions to O atoms, we can translate this structure to the silica

case. Furthermore, we scaled the figure by choosing a mean O–O NN distance of 0.263 nm, which was measured in an ND study of bulk vitreous silica [53]. The O–O PDH can be seen in Figure A.4. Clearly, peaks can be identified up to a radial distance of at least 2 nm.



# Bibliography

- [1] R. Zallen. *The Physics of Amorphous Solids*. Wiley-VCH Verlag GmbH & Co. KGaA, Weinheim (1983).
- [2] N. Seljakow, L. Strutinski and A. Krasnikow. *Zur Frage nach der Struktur des Glases*. Z. Phys. A **33**, 53 (1925).
- [3] W. H. Zachariasen. *The Atomic Arrangement in Glass*. J. Am. Chem. Soc. **54**, 3841 (1932).
- [4] B. E. Warren. *X-Ray Determination of the Structure of Glass*. J. Am. Ceram. Soc. **17**, 249 (1934).
- [5] A. C. Wright. *Neutron scattering from vitreous silica. V. The structure of vitreous silica: What have we learned from 60 years of diffraction studies?* J. Non-Cryst. Solids **179**, 84 (1994).
- [6] G. N. Greaves and S. Sen. *Inorganic glasses, glass-forming liquids and amorphizing solids*. Adv. Phys. **56**, 1 (2007).
- [7] G. Binnig and H. Rohrer. *Scanning tunneling microscopy*. Helv. Phys. Acta **52**, 726 (1982).
- [8] G. Binnig and H. Rohrer. *Scanning tunneling microscopy – from birth to adolescence*. Rev. Mod. Phys. **59**, 615 (1987).
- [9] G. Binnig, C. F. Quate and C. Gerber. *Atomic Force Microscope*. Phys. Rev. Lett. **56**, 930 (1986).
- [10] W. Raberg, V. Lansmann, M. Jansen and K. Wandelt. *Atomically Resolved Structure of Fracture Surfaces of a Ba/Si/O/C Glass with Atomic Force Microscopy*. Angew. Chem. Int. Ed. **36**, 2646 (1997).
- [11] W. Raberg and K. Wandelt. *Atomically resolved AFM investigations of an amorphous barium silicate surface*. Appl. Phys. A: Mater. Sci. Process. **66**, 1143 (1998).

- [12] H. Schlenz, A. Kirfel, K. Schulmeister, N. Wartner, W. Mader, W. Raberg, K. Wandelt, C. Oligschleger, S. Bender, R. Franke, J. Hormes, W. Hoffbauer, V. Lansmann, M. Jansen, N. Zotov, C. Mariani, H. Putz and J. Neufeind. *Structure analyses of Ba-silicate glasses*. J. Non-Cryst. Solids **297**, 37 (2002).
- [13] J.-F. Poggemann, G. Heide and G. Frischat. *Direct view of the structure of different glass fracture surfaces by atomic force microscopy*. J. Non-Cryst. Solids **326-327**, 15 (2003).
- [14] G. Frischat, J.-F. Poggemann and G. Heide. *Nanostructure and atomic structure of glass seen by atomic force microscopy*. J. Non-Cryst. Solids **345-346**, 197 (2004).
- [15] W. Raberg, A. Ostadrahimi, T. Kayser and K. Wandelt. *Atomic scale imaging of amorphous silicate glass surfaces by scanning force microscopy*. J. Non-Cryst. Solids **351**, 1089 (2005).
- [16] D. E. Bürgler, C. M. Schmidt, D. M. Schaller, F. Meisinger, T. M. Schaub, A. Baratoff and H.-J. Güntherodt. *Atomic-scale scanning tunneling microscopy of amorphous surfaces*. Phys. Rev. B **59**, 10895 (1999).
- [17] T. Schroeder, M. Adelt, B. Richter, M. Naschitzki, M. Bäumer and H.-J. Freund. *Epitaxial Growth of SiO<sub>2</sub> on Mo(112)*. Surf. Rev. Lett. **7**, 7 (2000).
- [18] J. Weissenrieder, S. Kaya, J.-L. Lu, H.-J. Gao, S. Shaikhutdinov, H.-J. Freund, M. Sierka, T. K. Todorova and J. Sauer. *Atomic Structure of a Thin Silica Film on a Mo(112) Substrate: A Two-Dimensional Network of SiO<sub>4</sub> Tetrahedra*. Phys. Rev. Lett. **95**, 076103 (2005).
- [19] S. Wendt, E. Ozensoy, T. Wei, M. Frerichs, Y. Cai, M. S. Chen and D. W. Goodman. *Electronic and vibrational properties of ultrathin SiO<sub>2</sub> films grown on Mo(112)*. Phys. Rev. B **72**, 115409 (2005).
- [20] S. Kaya, M. Baron, D. Stacchiola, J. Weissenrieder, S. Shaikhutdinov, T. Todorova, M. Sierka, J. Sauer and H.-J. Freund. *On the geometrical and electronic structure of an ultra-thin crystalline silica film grown on Mo(1 1 2)*. Surf. Sci. **601**, 4849 (2007).
- [21] T. K. Todorova, M. Sierka, J. Sauer, S. Kaya, J. Weissenrieder, J.-L. Lu, H.-J. Gao, S. Shaikhutdinov and H.-J. Freund. *Atomic structure*

- of a thin silica film on a Mo(112) substrate: A combined experimental and theoretical study.* Phys. Rev. B **73**, 165414 (2006).
- [22] J. F. Jerratsch, N. Nilius, H.-J. Freund, U. Martinez, L. Giordano and G. Pacchioni. *Lithium incorporation into a silica thin film: Scanning tunneling microscopy and density functional theory.* Phys. Rev. B **80**, 245423 (2009).
- [23] U. Martinez, J.-F. Jerratsch, N. Nilius, L. Giordano, G. Pacchioni and H.-J. Freund. *Tailoring the Interaction Strength between Gold Particles and Silica Thin Films via Work Function Control.* Phys. Rev. Lett. **103**, 056801 (2009).
- [24] S. Ulrich, N. Nilius, H.-J. Freund, U. Martinez, L. Giordano and G. Pacchioni. *Modifying the Adsorption Characteristic of Inert Silica Films by Inserting Anchoring Sites.* Phys. Rev. Lett. **102**, 016102 (2009).
- [25] S. Ulrich, N. Nilius, H.-J. Freund, U. Martinez, L. Giordano and G. Pacchioni. *Realization of an atomic sieve: Silica on Mo(1 1 2).* Surf. Sci. **603**, 1145 (2009).
- [26] J.-F. Jerratsch, N. Nilius, D. Topwal, U. Martinez, L. Giordano, G. Pacchioni and H.-J. Freund. *Stabilizing Monomeric Iron Species in a Porous Silica/Mo(112) Film.* ACS Nano **4**, 863 (2010).
- [27] D. J. Stacchiola, M. Baron, S. Kaya, J. Weissenrieder, S. Shaikhutdinov and H.-J. Freund. *Growth of stoichiometric subnanometer silica films.* Appl. Phys. Lett. **92**, 011911 (2008).
- [28] D. Löffler, J. J. Uhlrich, M. Baron, B. Yang, X. Yu, L. Lichtenstein, L. Heinke, C. Büchner, M. Heyde, S. Shaikhutdinov, H.-J. Freund, R. Włodarczyk, M. Sierka and J. Sauer. *Growth and Structure of Crystalline Silica Sheet on Ru(0001).* Phys. Rev. Lett. **105**, 146104 (2010).
- [29] L. Lichtenstein, C. Büchner, B. Yang, S. Shaikhutdinov, M. Heyde, M. Sierka, R. Włodarczyk, J. Sauer and H.-J. Freund. *The Atomic Structure of a Metal-Supported Vitreous Thin Silica Film.* Angew. Chem. Int. Ed. **51**, 404 (2012).
- [30] L. Lichtenstein, C. Büchner, S. Stuckenholtz, M. Heyde and H.-J. Freund. *Enhanced atomic corrugation in dynamic force microscopy—The role of repulsive forces.* Appl. Phys. Lett. **100**, 123105 (2012).

- [31] L. Lichtenstein, M. Heyde and H.-J. Freund. *Atomic Arrangement in Two-Dimensional Silica: From Crystalline to Vitreous Structures*. J. Phys. Chem. C **116**, 20426 (2012).
- [32] L. Lichtenstein, M. Heyde, S. Ulrich, N. Nilius and H.-J. Freund. *Probing the properties of metal-oxide interfaces: silica films on Mo and Ru supports*. J. Phys. Condens. Matter **24**, 354010 (2012).
- [33] L. Lichtenstein, M. Heyde and H.-J. Freund. *Crystalline–Vitreous Interface in Two Dimensional Silica*. Phys. Rev. Lett. **109**, 106101 (2012).
- [34] B. Yang, W. E. Kaden, X. Yu, J. A. Boscoboinik, Y. Martynova, L. Lichtenstein, M. Heyde, M. Sterrer, R. Włodarczyk, M. Sierka, J. Sauer, S. Shaikhutdinov and H.-J. Freund. *Thin silica films on Ru(0001): monolayer, bilayer and three-dimensional networks of SiO<sub>4</sub> tetrahedra*. Phys. Chem. Chem. Phys. **14**, 11344 (2012).
- [35] P. Y. Huang, S. Kurasch, A. Srivastava, V. Skakalova, J. Kotakoski, A. V. Krasheninnikov, R. Hovden, Q. Mao, J. C. Meyer, J. Smet, D. A. Muller and U. Kaiser. *Direct Imaging of a Two-Dimensional Silica Glass on Graphene*. Nano Lett. **12**, 1081 (2012).
- [36] X. Yu, B. Yang, J. A. Boscoboinik, S. Shaikhutdinov and H.-J. Freund. *Support effects on the atomic structure of ultrathin silica films on metals*. Appl. Phys. Lett. **100**, 151608 (2012).
- [37] J. A. Bucaro and H. D. Dardy. *High-temperature Brillouin scattering in fused quartz*. J. Appl. Phys. **45**, 5324 (1974).
- [38] R. Brüning. *On the glass transition in vitreous silica by differential thermal analysis measurements*. J. Non-Cryst. Solids **330**, 13 (2003).
- [39] R. Brüning and K. Samwer. *Glass transition on long time scales*. Phys. Rev. B **46**, 11318 (1992).
- [40] J. H. Gibbs and E. A. DiMarzio. *Nature of the Glass Transition and the Glassy State*. J. Chem. Phys. **28**, 373 (1958).
- [41] P. G. Debenedetti and F. H. Stillinger. *Supercooled liquids and the glass transition*. Nature **410**, 259 (2001).
- [42] Q. Mei, C. J. Benmore and J. K. R. Weber. *Structure of Liquid SiO<sub>2</sub>: A Measurement by High-Energy X-Ray Diffraction*. Phys. Rev. Lett. **98**, 057802 (2007).



- [43] D. Levine and P. J. Steinhardt. *Quasicrystals. I. Definition and structure*. Phys. Rev. B **34**, 596 (1986).
- [44] D. Shechtman, I. Blech, D. Gratias and J. W. Cahn. *Metallic Phase with Long-Range Orientational Order and No Translational Symmetry*. Phys. Rev. Lett. **53**, 1951 (1984).
- [45] J. G. Berryman. *Random close packing of hard spheres and disks*. Phys. Rev. A **27**, 1053 (1983).
- [46] A. L. Greer. *Metallic Glasses*. Science **267**, 1947 (1995).
- [47] J. Schroers. *Processing of Bulk Metallic Glass*. Adv. Mater. **22**, 1566 (2010).
- [48] E. Riedel. *Anorganische Chemie*. De Gruyter, Berlin (2004).
- [49] J. T. Randall, H. P. Rooksby and B. S. Cooper. *X-Ray Diffraction and the Structure of Vitreous Solids—I*. Z. Krist. **75**, 196 (1930).
- [50] V. M. Goldschmidt. *Geochemische Verteilungsgesetze der Elemente, VIII – Untersuchungen Über Bau und Eigenschaften von Krystallen*. Skrifter Utgitt Av Det Norske-Videnskaps-Akademi I Oslo I. Matem.-Naturvid. Klasse **8**, 1 (1926).
- [51] J. M. Ziman. *Models of disorder: the theoretical physics of homogeneously disordered systems*. Cambridge Univ. Pr. (1979).
- [52] A. C. Wright. *Neutron and X-ray amorphography*. J. Non-Cryst. Solids **106**, 1 (1988).
- [53] D. I. Grimley, A. C. Wright and R. N. Sinclair. *Neutron scattering from vitreous silica IV. Time-of-flight diffraction*. J. Non-Cryst. Solids **119**, 49 (1990).
- [54] S. R. Elliott. *Medium-range structural order in covalent amorphous solids*. Nature **354**, 445 (1991).
- [55] J. H. Konnert and J. Karle. *The computation of radial distribution functions for glassy materials*. Acta Cryst. A **29**, 702 (1973).
- [56] S. R. Elliott. *Physics of Amorphous Materials*. Longman, London and New York (1983).
- [57] H. S. Peiser, H. P. Rooksby and A. J. C. Wilson (Eds.). *X-ray diffraction by polycrystalline materials*. Inst. of Physics, London (1955).

- [58] B. E. Warren, H. Krutter and O. Morningstar. *Fourier Analysis of X-Ray Patterns of Vitreous  $\text{SiO}_2$  and  $\text{B}_2\text{O}_3$* . J. Am. Ceram. Soc. **19**, 202 (1936).
- [59] R. L. Mozzi and B. E. Warren. *The structure of vitreous silica*. J. Appl. Crystallogr. **2**, 164 (1969).
- [60] J. R. G. Da Silva, D. G. Pinatti, C. E. Anderson and M. L. Rudee. *A refinement of the structure of vitreous silica*. Philos. Mag. **31**, 713 (1975).
- [61] A. C. Wright, A. G. Clare, D. I. Grimley and R. N. Sinclair. *Neutron scattering studies of network glasses*. J. Non-Cryst. Solids **112**, 33 (1989).
- [62] A. C. Wright, R. N. Sinclair and A. J. Leadbetter. *Effect of preparation method on the structure of amorphous solids in the system As-S*. J. Non-Cryst. Solids **71**, 295 (1985).
- [63] S. R. Elliott. *Origin of the first sharp diffraction peak in the structure factor of covalent glasses*. Phys. Rev. Lett. **67**, 711 (1991).
- [64] S. R. Elliott. *The origin of the first sharp diffraction peak in the structure factor of covalent glasses and liquids*. J. Phys. Condens. Matter **4**, 7661 (1992).
- [65] C. T. Kirk. *Quantitative analysis of the effect of disorder-induced mode coupling on infrared absorption in silica*. Phys. Rev. B **38**, 1255 (1988).
- [66] J. E. Olsen and F. Shimura. *Infrared spectroscopy of thin silicon dioxide on silicon*. Appl. Phys. Lett. **53**, 1934 (1988).
- [67] F. L. Galeener, A. J. Leadbetter and M. W. Stringfellow. *Comparison of the neutron, Raman, and infrared vibrational spectra of vitreous  $\text{SiO}_2$ ,  $\text{GeO}_2$ , and  $\text{BeF}_2$* . Phys. Rev. B **27**, 1052 (1983).
- [68] S. K. Sharma, J. F. Mammone and M. F. Nicol. *Raman investigation of ring configurations in vitreous silica*. Nature **292**, 140 (1981).
- [69] A. Pasquarello and R. Car. *Identification of Raman Defect Lines as Signatures of Ring Structures in Vitreous Silica*. Phys. Rev. Lett. **80**, 5145 (1998).
- [70] J. V. Smith and C. S. Blackwell. *Nuclear magnetic resonance of silica polymorphs*. Nature **303**, 223 (1983).

- [71] L. F. Gladden, T. A. Carpenter and S. R. Elliott.  $^{29}\text{Si}$  MAS NMR studies of the spin-lattice relaxation time and bond-angle distribution in vitreous silica. *Philos. Mag. B* **53**, 81 (1986).
- [72] T. M. Clark, P. J. Grandinetti, P. Florian and J. F. Stebbins. *Correlated structural distributions in silica glass*. *Phys. Rev. B* **70**, 064202 (2004).
- [73] H.-J. Freund and G. Pacchioni. *Oxide ultra-thin films on metals: new materials for the design of supported metal catalysts*. *Chem. Soc. Rev.* **37**, 2224 (2008).
- [74] R. J. Bell and P. Dean. *Properties of Vitreous Silica: Analysis of Random Network Models*. *Nature* **212**, 1354 (1966).
- [75] D. L. Evans and S. V. King. *Random Network Model of Vitreous Silica*. *Nature* **212**, 1353 (1966).
- [76] R. J. Bell and P. Dean. *The Structure and Spectra of Glasses: The Construction and Properties of a Model of Vitreous Silica*. NPL Mathematics Rept. Ma 62 (1967).
- [77] R. J. Bell and P. Dean. *The structure of vitreous silica: Validity of the random network theory*. *Philos. Mag.* **25**, 1381 (1972).
- [78] J. F. Shackelford and B. D. Brown. *The lognormal distribution in the random network structure*. *J. Non-Cryst. Solids* **44**, 379 (1981).
- [79] J. F. Shackelford. *Triangle rafts - extended Zachariasen schematics for structure modeling*. *J. Non-Cryst. Solids* **49**, 19 (1982).
- [80] T. F. Soules. *Computer simulation of glass structures*. *Journal of Non-Crystalline Solids* **123**, 48 (1990).
- [81] M. Duffy, D. Boudreaux and D. Polk. *Systematic generation of random networks*. *J. Non-Cryst. Solids* **15**, 435 (1974).
- [82] L. Gladden. *Medium-range order in  $v\text{-SiO}_2$* . *J. Non-Cryst. Solids* **119**, 318 (1990).
- [83] B. J. Alder and T. E. Wainwright. *Studies in Molecular Dynamics. I. General Method*. *J. Chem. Phys.* **31**, 459 (1959).
- [84] L. V. Woodcock, C. A. Angell and P. Cheeseman. *Molecular dynamics studies of the vitreous state: Simple ionic systems and silica*. *J. Chem. Phys.* **65**, 1565 (1976).

- [85] T. F. Soules. *A molecular dynamic calculation of the structure of sodium silicate glasses*. J. Chem. Phys. **71**, 4570 (1979).
- [86] S. K. Mitra, M. Amini, D. Fincham and R. W. Hockney. *Molecular dynamics simulation of silicon dioxide glass*. Philos. Mag. B **43**, 365 (1981).
- [87] F. Wooten, K. Winer and D. Weaire. *Computer Generation of Structural Models of Amorphous Si and Ge*. Phys. Rev. Lett. **54**, 1392 (1985).
- [88] J. P. Rino, I. Ebbsjö, R. K. Kalia, A. Nakano and P. Vashishta. *Structure of rings in vitreous SiO<sub>2</sub>*. Phys. Rev. B **47**, 3053 (1993).
- [89] K. Vollmayr, W. Kob and K. Binder. *Cooling-rate effects in amorphous silica: A computer-simulation study*. Phys. Rev. B **54**, 15808 (1996).
- [90] K. Binder, J. Baschnagel, W. Kob, K. Okun, W. Paul, K. Vollmayr and M. Wolfgardt. *Complex Behaviour of Glassy Systems* **492**, 22 (1997).
- [91] A. Roder, W. Kob and K. Binder. *Structure and dynamics of amorphous silica surfaces*. J. Chem. Phys. **114**, 7602 (2001).
- [92] X. Yuan and A. Cormack. *Local structures of MD-modeled vitreous silica and sodium silicate glasses*. J. Non-Cryst. Solids **283**, 69 (2001).
- [93] A. Tilocca, N. H. de Leeuw and A. N. Cormack. *Shell-model molecular dynamics calculations of modified silicate glasses*. Phys. Rev. B **73**, 104209 (2006).
- [94] A. Omeltchenko, T. J. Campbell, R. K. Kalia, X. Liu, A. Nakano and P. Vashishta. *Scalable I/O of large-scale molecular dynamics simulations: A data-compression algorithm*. Comput. Phys. Commun. **131**, 78 (2000).
- [95] D. A. Keen and R. L. McGreevy. *Structural modelling of glasses using reverse Monte Carlo simulation*. Nature **344**, 423 (1990).
- [96] R. O. Jones and O. Gunnarsson. *The density functional formalism, its applications and prospects*. Rev. Mod. Phys. **61**, 689 (1989).
- [97] W. Koch and M. C. Holthausen. *A Chemist's Guide to Density Functional Theory*. Wiley-VCH Verlag GmbH (2001).

- [98] P. Geerlings, F. De Proft and W. Langenaeker. *Conceptual Density Functional Theory*. Chem. Rev. **103**, 1793 (2003).
- [99] J. Sarnthein, A. Pasquarello and R. Car. *Origin of the High-Frequency Doublet in the Vibrational Spectrum of Vitreous SiO<sub>2</sub>*. Science **275**, 1925 (1997).
- [100] R. M. Van Ginhoven, H. Jónsson and L. R. Corrales. *Silica glass structure generation for ab initio calculations using small samples of amorphous silica*. Phys. Rev. B **71**, 024208 (2005).
- [101] M. Corno, A. Pedone, R. Dovesi and P. Ugliengo. *B3LYP Simulation of the Full Vibrational Spectrum of 45S5 Bioactive Silicate Glass Compared to v-Silica*. Chem. Mater. **20**, 5610 (2008).
- [102] R. Car and M. Parrinello. *Unified Approach for Molecular Dynamics and Density-Functional Theory*. Phys. Rev. Lett. **55**, 2471 (1985).
- [103] J. Sarnthein, A. Pasquarello and R. Car. *Structural and Electronic Properties of Liquid and Amorphous SiO<sub>2</sub>: An Ab Initio Molecular Dynamics Study*. Phys. Rev. Lett. **74**, 4682 (1995).
- [104] M. Benoit, S. Ispas, P. Jund and R. Jullien. *Model of silica glass from combined classical and ab initio molecular-dynamics simulations*. Eur. Phys. J. B **13**, 631 (2000).
- [105] M. P. Seah and W. A. Dench. *Quantitative electron spectroscopy of surfaces: A standard data base for electron inelastic mean free paths in solids*. Surf. Interface Anal. **1**, 2 (1979).
- [106] G. Ertl and J. Küppers. *Low energy electrons and surface chemistry*. Verlag Chemie, Weinheim (1974).
- [107] K. Christmann. *Introduction to surface physical chemistry*. Steinkopff, Darmstadt (1991).
- [108] M. A. Van Hove and S. Y. Tong. *Surface crystallography by LEED: theory, computation and structural results*. Springer, Berlin (1979).
- [109] M. A. Van Hove, W. H. Weinberg and C.-M. Chan. *Low-energy electron diffraction: experiment, theory and surface structure determination*. Springer, Berlin (1986).
- [110] P. W. Palmberg, G. K. Bohn and J. C. Tracy. *High Sensitivity Auger Electron Spectrometer*. Appl. Phys. Lett. **15**, 254 (1969).

- [111] J. W. Niemantsverdriet. *Spectroscopy in Catalysis*. Wiley-VCH Verlag GmbH & Co. KGaA, Weinheim (2007).
- [112] P. Auger. *Sur l'effet photoélectrique composé*. J. Phys. Radium **6**, 205 (1925).
- [113] L. E. Davis, N. C. MacDonald, P. W. Palmberg, G. E. Riach and R. E. Weber. *Handbook of Auger electron spectroscopy, 2. ed.* Phys. Electr. Div., Perkin-Elmer Co., Eden Prairie, Minn. (1976).
- [114] M. Morgenstern, A. Schwarz and U. Schwarz. *Springer Handbook of Nanotechnology*. Springer Berlin Heidelberg (2007).
- [115] F. J. Giessibl. *Atomic resolution on Si(111)-(7 × 7) by noncontact atomic force microscopy with a force sensor based on a quartz tuning fork*. Appl. Phys. Lett. **76**, 1470 (2000).
- [116] H.-P. Rust, M. Heyde and H.-J. Freund. *Signal electronics for an atomic force microscope equipped with a double quartz tuning fork sensor*. Rev. Sci. Instrum. **77**, 043710 (2006).
- [117] M. Heyde, M. Sterrer, H.-P. Rust and H.-J. Freund. *Atomic resolution on MgO(001) by atomic force microscopy using a double quartz tuning fork sensor at low-temperature and ultrahigh vacuum*. Appl. Phys. Lett. **87**, 083104 (2005).
- [118] M. Heyde, G. H. Simon, H.-P. Rust and H.-J. Freund. *Probing adsorption sites on thin oxide films by dynamic force microscopy*. Appl. Phys. Lett. **89**, 263107 (2006).
- [119] G. H. Simon. *Dynamic Force Microscopy on Ultrathin Alumina*. Dissertation, Technische Universität Berlin (2011).
- [120] T. R. Albrecht, P. Grütter, D. Horne and D. Rugar. *Frequency modulation detection using high-Q cantilevers for enhanced force microscope sensitivity*. J. Appl. Phys. **69**, 668 (1991).
- [121] S. Morita, F. J. Giessibl and R. Wiesendanger (Eds.). *Noncontact Atomic Force Microscopy*. Springer Berlin Heidelberg (2009).
- [122] G. Binnig and H. Rohrer. *Scanning tunneling microscopy*. Surf. Sci. **126**, 236 (1983).
- [123] C. J. Chen. *Introduction to scanning tunneling microscopy*. Oxford Univ. Pr., New York (1993).

- [124] J. Bardeen. *Tunnelling from a Many-Particle Point of View*. Phys. Rev. Lett. **6**, 57 (1961).
- [125] J. Tersoff and D. R. Hamann. *Theory of the scanning tunneling microscope*. Phys. Rev. B **31**, 805 (1985).
- [126] N. D. Lang. *Spectroscopy of single atoms in the scanning tunneling microscope*. Phys. Rev. B **34**, 5947 (1986).
- [127] M. Guggisberg, M. Bammerlin, C. Loppacher, O. Pfeiffer, A. Abdurixit, V. Barwich, R. Bennowitz, A. Baratoff, E. Meyer and H.-J. Güntherodt. *Separation of interactions by noncontact force microscopy*. Phys. Rev. B **61**, 11151 (2000).
- [128] J. N. Israelachvili. *Intermolecular and surface forces, 2. ed.* Acad. Pr., London (1992).
- [129] J. E. Sader and S. P. Jarvis. *Accurate formulas for interaction force and energy in frequency modulation force spectroscopy*. Appl. Phys. Lett. **84**, 1801 (2004).
- [130] Y. Kuk. *Scanning tunneling microscopy 1: General principles and applications to clean and adsorbate-covered surfaces*. Springer Berlin (1992).
- [131] R. M. Feenstra. *Scanning tunneling spectroscopy*. Surf. Sci. **299-300**, 965 (1994).
- [132] J. Kliewer and R. Berndt. *Scanning tunneling spectroscopy of Na on Cu(111)*. Phys. Rev. B **65**, 035412 (2001).
- [133] A. J. Heinrich, J. A. Gupta, C. P. Lutz and D. M. Eigler. *Single-Atom Spin-Flip Spectroscopy*. Science **306**, 466 (2004).
- [134] F. E. Olsson, S. Paavilainen, M. Persson, J. Repp and G. Meyer. *Multiple Charge States of Ag Atoms on Ultrathin NaCl Films*. Phys. Rev. Lett. **98**, 176803 (2007).
- [135] D. E. Barlow and K. W. Hipps. *A Scanning Tunneling Microscopy and Spectroscopy Study of Vanadyl Phthalocyanine on Au(111): the Effect of Oxygen Binding and Orbital Mediated Tunneling on the Apparent Corrugation*. J. Phys. Chem. B **104**, 5993 (2000).

- [136] P. Liljeroth, J. Repp and G. Meyer. *Current-Induced Hydrogen Tautomerization and Conductance Switching of Naphthalocyanine Molecules*. *Science* **317**, 1203 (2007).
- [137] B. C. Stipe, M. A. Rezaei and W. Ho. *Single-Molecule Vibrational Spectroscopy and Microscopy*. *Science* **280**, 1732 (1998).
- [138] L. J. Lauhon and W. Ho. *Single-molecule vibrational spectroscopy and microscopy: CO on Cu(001) and Cu(110)*. *Phys. Rev. B* **60**, R8525 (1999).
- [139] S. Kitamura and M. Iwatsuki. *High-resolution imaging of contact potential difference with ultrahigh vacuum noncontact atomic force microscope*. *Appl. Phys. Lett.* **72**, 3154 (1998).
- [140] A. Sasahara, C. L. Pang and H. Onishi. *Local Work Function of Pt Clusters Vacuum-Deposited on a TiO<sub>2</sub> Surface*. *J. Phys. Chem. B* **110**, 17584 (2006).
- [141] T. König, G. H. Simon, H.-P. Rust and M. Heyde. *Work Function Measurements of Thin Oxide Films on Metals: MgO on Ag(001)*. *J. Phys. Chem. C* **113**, 11301 (2009).
- [142] L. Heinke, L. Lichtenstein, G. H. Simon, T. König, M. Heyde and H.-J. Freund. *Local Work Function Differences at Line Defects in Aluminium Oxide on NiAl(110)*. *ChemPhysChem* **11**, 2085 (2010).
- [143] L. Gross, F. Mohn, P. Liljeroth, J. Repp, F. J. Giessibl and G. Meyer. *Measuring the Charge State of an Adatom with Noncontact Atomic Force Microscopy*. *Science* **324**, 1428 (2009).
- [144] T. König, G. H. Simon, H.-P. Rust, G. Pacchioni, M. Heyde and H.-J. Freund. *Measuring the Charge State of Point Defects on MgO/Ag(001)*. *J. Am. Chem. Soc.* **131**, 17544 (2009).
- [145] M. Nonnenmacher, M. P. O'Boyle and H. K. Wickramasinghe. *Kelvin probe force microscopy*. *Appl. Phys. Lett.* **58**, 2921 (1991).
- [146] H. O. Jacobs, P. Leuchtman, O. J. Homan and A. Stemmer. *Resolution and contrast in Kelvin probe force microscopy*. *J. Appl. Phys.* **84**, 1168 (1998).
- [147] U. Zerweck, C. Loppacher, T. Otto, S. Grafström and L. M. Eng. *Accuracy and resolution limits of Kelvin probe force microscopy*. *Phys. Rev. B* **71**, 125424 (2005).



- [148] G. H. Enevoldsen, T. Glatzel, M. C. Christensen, J. V. Lauritsen and F. Besenbacher. *Atomic Scale Kelvin Probe Force Microscopy Studies of the Surface Potential Variations on the  $\text{TiO}_2(110)$  Surface*. Phys. Rev. Lett. **100**, 236104 (2008).
- [149] F. Mohn, L. Gross, N. Moll and G. Meyer. *Imaging the charge distribution within a single molecule*. Nat. Nano. **7**, 227 (2012).
- [150] L. Bartels, G. Meyer and K.-H. Rieder. *Controlled vertical manipulation of single CO molecules with the scanning tunneling microscope: A route to chemical contrast*. Appl. Phys. Lett. **71**, 213 (1997).
- [151] N. Nilius. *Properties of oxide thin films and their adsorption behavior studied by scanning tunneling microscopy and conductance spectroscopy*. Surf. Sci. Rep. **64**, 595 (2009).
- [152] J. E. Sader and Y. Sugimoto. *Accurate formula for conversion of tunneling current in dynamic atomic force spectroscopy*. Appl. Phys. Lett. **97**, 043502 (2010).
- [153] K.-I. Fukui, H. Onishi and Y. Iwasawa. *Atom-Resolved Image of the  $\text{TiO}_2(110)$  Surface by Noncontact Atomic Force Microscopy*. Phys. Rev. Lett. **79**, 4202 (1997).
- [154] C. Barth and M. Reichling. *Imaging the atomic arrangements on the high-temperature reconstructed  $\alpha\text{-Al}_2\text{O}_3(0001)$  surface*. Nature **414**, 54 (2001).
- [155] G. H. Simon, T. König, H.-P. Rust, M. Heyde and H.-J. Freund. *Atomic structure of the ultrathin alumina on  $\text{NiAl}(110)$  and its antiphase domain boundaries as seen by frequency modulation dynamic force microscopy*. New J. Phys. **11**, 093009 (2009).
- [156] J. V. Lauritsen and M. Reichling. *Atomic resolution non-contact atomic force microscopy of clean metal oxide surfaces*. J. Phys. Condens. Matter **22**, 263001 (2010).
- [157] F. Mohn, L. Gross and G. Meyer. *Measuring the short-range force field above a single molecule with atomic resolution*. Appl. Phys. Lett. **99**, 053106 (2011).
- [158] X. Xu and D. W. Goodman. *New approach to the preparation of ultrathin silicon dioxide films at low temperatures*. Appl. Phys. Lett. **61**, 774 (1992).

- [159] X. Xu and D. Goodman. *The preparation and characterization of ultrathin silicon dioxide films on a Mo(110) surface*. Surf. Sci. **282**, 323 (1993).
- [160] T. Schroeder, J. B. Giorgi, M. Bäumer and H.-J. Freund. *Morphological and electronic properties of ultrathin crystalline silica epilayers on a Mo(112) substrate*. Phys. Rev. B **66**, 165422 (2002).
- [161] J.-L. Lu, S. Kaya, J. Weissenrieder, T. Todorova, M. Sierka, J. Sauer, H.-J. Gao, S. Shaikhutdinov and H.-J. Freund. *Formation of one-dimensional crystalline silica on a metal substrate*. Surf. Sci. **600**, L164 (2006).
- [162] P. Eckerlin and H. Kandler. *Landolt-Börnstein - Group III Condensed Matter*, Bd. 6. Springer Materials, Landolt-Börnstein Database.
- [163] D. Mullins, P. Radulovic and S. Overbury. *Ordered cerium oxide thin films grown on Ru(0001) and Ni(111)*. Surf. Sci. **429**, 186 (1999).
- [164] J.-L. Lu, H.-J. Gao, S. Shaikhutdinov and H.-J. Freund. *Gold supported on well-ordered ceria films: nucleation, growth and morphology in CO oxidation reaction*. Catalysis Letters **114**, 8 (2007).
- [165] T. E. Madey, H. Albert Engelhardt and D. Menzel. *Adsorption of oxygen and oxidation of CO on the ruthenium (001) surface*. Surf. Sci. **48**, 304 (1975).
- [166] D. M. Eigler and E. K. Schweizer. *Positioning Single Atoms With A Scanning Tunneling Microscope*. Nature **344**, 524 (1990).
- [167] T. K. Shimizu, A. Mugarza, J. I. Cerda, M. Heyde, Y. Qi, U. D. Schwarz, D. F. Ogletree and M. Salmeron. *Surface Species Formed by the Adsorption and Dissociation of Water Molecules on a Ru(0001) Surface Containing a Small Coverage of Carbon Atoms Studied by Scanning Tunneling Microscopy*. J. Phys. Chem. C **112**, 7445 (2008).
- [168] K. Kostov, M. Gsell, P. Jakob, T. Moritz, W. Widdra and D. Menzel. *Observation of a novel high density 3O(2×2) structure on Ru(001)*. Surf. Sci. **394**, L138 (1997).
- [169] M. Gsell, M. Stichler, P. Jakob and D. Menzel. *Formation and geometry of a high-coverage oxygen adlayer on Ru(001), the p(2 × 2)-3O phase*. Isr. J. Chem. **38**, 339 (1998).

- [170] C. Stampfl, S. Schwegmann, H. Over, M. Scheffler and G. Ertl. *Structure and Stability of a High-Coverage (1×1) Oxygen Phase on Ru(0001)*. Phys. Rev. Lett. **77**, 3371 (1996).
- [171] H. K. Hansen, T. Worren, E. Lægsgaard, F. Besenbacher and I. Stensgaard. *Bias dependent apparent height of an Al<sub>2</sub>O<sub>3</sub> thin film on NiAl(110), and of supported Pd clusters*. Surf. Sci. **475**, 96 (2001).
- [172] R. Włodarczyk, M. Sierka, J. Sauer, D. Löffler, J. J. Uhlrich, X. Yu, B. Yang, I. M. N. Groot, S. Shaikhutdinov and H.-J. Freund. *Tuning the electronic structure of ultrathin crystalline silica films on Ru(0001)*. Phys. Rev. B **85**, 085403 (2012).
- [173] F. Musso, M. Sodupe, M. Corno and P. Ugliengo. *H-Bond Features of Fully Hydroxylated Surfaces of Crystalline Silica Polymorphs: A Periodic B3LYP Study*. J. Phys. Chem. C **113**, 17876 (2009).
- [174] J. R. Hill and J. Sauer. *Molecular mechanics potential for silica and zeolite catalysts based on ab initio calculations. 1. Dense and microporous silica*. J. Phys. Chem. **98**, 1238 (1994).
- [175] V. Moravetski, J.-R. Hill, U. Eichler, A. K. Cheetham and J. Sauer. *<sup>29</sup>Si NMR Chemical Shifts of Silicate Species: Ab Initio Study of Environment and Structure Effects*. J. Am. Chem. Soc. **118**, 13015 (1996).
- [176] X. Yuan and A. Cormack. *Si-O-Si bond angle and torsion angle distribution in vitreous silica and sodium silicate glasses*. J. Non-Cryst. Solids **319**, 31 (2003).
- [177] K. Trachenko and M. T. Dove. *Compressibility, kinetics, and phase transition in pressurized amorphous silica*. Phys. Rev. B **67**, 064107 (2003).
- [178] S. Kohara and K. Suzuya. *Intermediate-range order in vitreous SiO<sub>2</sub> and GeO<sub>2</sub>*. J. Phys. Condens. Matter **17**, S77 (2005).
- [179] S. V. King. *Ring Configurations in a Random Network Model of Vitreous Silica*. Nature **213**, 1112 (1967).
- [180] A. A. Green and M. C. Hersam. *Solution Phase Production of Graphene with Controlled Thickness via Density Differentiation*. Nano Lett. **9**, 4031 (2009).
- [181] L. Levien, C. T. Prewitt and D. J. Weidner. *Structure and Elastic Properties of Quartz At Pressure*. Am. Mineral. **65**, 920 (1980).

- [182] K. Kihara. *An X-ray study of the temperature dependence of the quartz structure*. Eur. J. Mineral. **2**, 63 (1990).
- [183] A. Wright and M. Lehmann. *The structure of quartz at 25 and 590° C determined by neutron diffraction*. J. Solid State Chem. **36**, 371 (1981).
- [184] M. G. Tucker, D. A. Keen and M. T. Dove. *A detailed structural characterization of quartz on heating through the a-b phase transition*. Mineral. Mag. **65**, 489 (2001).
- [185] J. Purton, R. Jones, C. R. A. Catlow and M. Leslie. *Ab initio potentials for the calculation of the dynamical and elastic properties of  $\alpha$ -quartz*. Phys. Chem. Miner. **19**, 392 (1993).
- [186] B. Civalleri, C. Zicovich-Wilson, P. Ugliengo, V. Saunders and R. Dovesi. *A periodic ab initio study of the structure and relative stability of silica polymorphs*. Chemical Physics Letters **292**, 394 (1998).
- [187] H. Jónsson. *Private communication* .
- [188] F. Spaepen. *A structural model for the interface between amorphous and crystalline Si or Ge*. Acta Metall. **26**, 1167 (1978).
- [189] N. Borgardt, B. Plikat, M. Seibt and W. Schröter. *Analysis of high resolution transmission electron microscope images of crystalline-amorphous interfaces*. Ultramicroscopy **90**, 241 (2002).
- [190] N. I. Borgardt, B. Plikat, W. Schröter, M. Seibt and T. Wagner. *Atomic structure of the interface between silicon (111) and amorphous germanium*. Phys. Rev. B **70**, 195307 (2004).
- [191] N. Bernstein, M. J. Aziz and E. Kaxiras. *Amorphous-crystal interface in silicon: A tight-binding simulation*. Phys. Rev. B **58**, 4579 (1998).
- [192] L. Houben, M. Luysberg, P. Hapke, R. Carius, F. Finger and H. Wagner. *Structural properties of microcrystalline silicon in the transition from highly crystalline to amorphous growth*. Philos. Mag. A **77**, 1447 (1998).
- [193] Y. Tu, J. Tersoff, G. Grinstein and D. Vanderbilt. *Properties of a Continuous-Random-Network Model for Amorphous Systems*. Phys. Rev. Lett. **81**, 4899 (1998).

- [194] C. R. S. da Silva and A. Fazio. *Formation and structural properties of the amorphous-crystal interface in a nanocrystalline system*. Phys. Rev. B **64**, 075301 (2001).
- [195] S. Blonski and S. H. Garofalini. *Atomistic Structure of Calcium Silicate Intergranular Films in Alumina Studied by Molecular Dynamics Simulations*. J. Am. Ceram. Soc. **80**, 1997 (1997).
- [196] W. Walkosz, R. F. Klie, S. Ögüt, B. Mikijelj, S. J. Pennycook, S. T. Pantelides and J. C. Idrobo. *Crystal-induced effects at crystal/amorphous interfaces: The case of  $\text{Si}_3\text{N}_4/\text{SiO}_2$* . Phys. Rev. B **82**, 081412 (2010).
- [197] D. E. Aspnes and J. B. Theeten. *Spectroscopic Analysis of the Interface Between Si and Its Thermally Grown Oxide*. J. Electrochem. Soc. **127**, 1359 (1980).
- [198] I. Ohdomari, T. Mihara and K. Kai. *Computer simulation of high-resolution transmission electron microscopy images of Si-SiO<sub>2</sub> interfaces*. J. Appl. Phys. **59**, 2798 (1986).
- [199] A. Ourmazd, D. W. Taylor, J. A. Rentschler and J. Bevk. *Si-SiO<sub>2</sub> transformation: Interfacial structure and mechanism*. Phys. Rev. Lett. **59**, 213 (1987).
- [200] F. J. Himpsel, F. R. McFeely, A. Taleb-Ibrahimi, J. A. Yarmoff and G. Hollinger. *Microscopic structure of the SiO<sub>2</sub>-Si interface*. Phys. Rev. B **38**, 6084 (1988).
- [201] A. Pasquarello, M. S. Hybertsen and R. Car. *Structurally relaxed models of the Si(001)-SiO<sub>2</sub> interface*. Appl. Phys. Lett. **68**, 625 (1996).
- [202] D.-A. Luh, T. Miller and T.-C. Chiang. *Statistical Cross-Linking at the Si(111)-SiO<sub>2</sub> Interface*. Phys. Rev. Lett. **79**, 3014 (1997).
- [203] A. Pasquarello, M. S. Hybertsen and R. Car. *Interface structure between silicon and its oxide by first-principles molecular dynamics*. Nature **396**, 58 (1998).
- [204] Y. Tu and J. Tersoff. *Structure and Energetics of the Si-SiO<sub>2</sub> Interface*. Phys. Rev. Lett. **84**, 4393 (2000).
- [205] N. Ikarashi, K. Watanabe and Y. Miyamoto. *High-resolution transmission electron microscopy of an atomic structure at a Si(001) oxidation front*. Phys. Rev. B **62**, 15989 (2000).

- [206] R. Buczko, S. J. Pennycook and S. T. Pantelides. *Bonding Arrangements at the Si-SiO<sub>2</sub> and SiC-SiO<sub>2</sub> Interfaces and a Possible Origin of their Contrasting Properties*. Phys. Rev. Lett. **84**, 943 (2000).
- [207] M. C. Cheynet and T. Epicier. *Structural and chemical analysis of a model Si-SiO<sub>2</sub> interface using spatially resolved electron-energy-loss spectroscopy*. Philos. Mag. **84**, 1753 (2004).
- [208] N. Nakanishi, Y. Kikuchi, T. Yamazaki, E. Okunishi, K. Watanabe and I. Hashimoto. *Quantitative evaluation of SiO<sub>2</sub>-Si interfaces using high-resolution high-angle annular dark field scanning transmission electron microscopy*. Phys. Rev. B **70**, 165324 (2004).
- [209] M. Kulawik, H.-P. Rust and H.-J. Freund. *Defect-induced gap states in Al<sub>2</sub>O<sub>3</sub> thin films on NiAl(110)*. Phys. Rev. B **69**, 121401 (2004).
- [210] A. Stone and D. Wales. *Theoretical studies of icosahedral C<sub>60</sub> and some related species*. Chem. Phys. Lett. **128**, 501 (1986).
- [211] P. W. Rabideau and A. Sygula. *Buckybowls: Polynuclear Aromatic Hydrocarbons Related to the Buckminsterfullerene Surface*. Acc. Chem. Res. **29**, 235 (1996).
- [212] K. Suenaga, H. Wakabayashi, M. Koshino, Y. Sato, K. Urita and S. Iijima. *Imaging active topological defects in carbon nanotubes*. Nat. Nano. **2**, 358 (2007).
- [213] A. Hashimoto, K. Suenaga, A. Gloter, K. Urita and S. Iijima. *Direct evidence for atomic defects in graphene layers*. Nature **430**, 870 (2004).
- [214] J. C. Meyer, C. Kisielowski, R. Erni, M. D. Rossell, M. F. Crommie and A. Zettl. *Direct Imaging of Lattice Atoms and Topological Defects in Graphene Membranes*. Nano Lett. **8**, 3582 (2008).
- [215] P. Y. Huang, C. S. Ruiz-Vargas, A. M. van der Zande, W. S. Whitney, M. P. Levendorf, J. W. Kevek, S. Garg, J. S. Alden, C. J. Hustedt, Y. Zhu, J. Park, P. L. McEuen and D. A. Muller. *Grains and grain boundaries in single-layer graphene atomic patchwork quilts*. Nature **469**, 389 (2011).
- [216] F. Yang, Y. Choi, P. Liu, D. Stacchiola, J. Hrbek and J. A. Rodriguez. *Identification of 5-7 Defects in a Copper Oxide Surface*. J. Am. Chem. Soc. **133**, 11474 (2011).

- 
- [217] J. Hwang, Z. H. Melgarejo, Y. E. Kalay, I. Kalay, M. J. Kramer, D. S. Stone and P. M. Voyles. *Nanoscale Structure and Structural Relaxation in  $Zr_{50}Cu_{45}Al_5$  Bulk Metallic Glass*. *Phys. Rev. Lett.* **108**, 195505 (2012).





# Résumé

Der Lebenslauf ist in der Online-Version aus Gründen des Datenschutzes nicht enthalten.



# List of Publications

1. **L. Lichtenstein**, M. Heyde and H.-J. Freund. *Atomic Arrangement in Two-Dimensional Silica: From Crystalline to Vitreous Structures*. J. Phys. Chem. C **116**, 20426 (2012).
2. **L. Lichtenstein**, M. Heyde and H.-J. Freund. *Crystalline–Vitreous Interface in Two Dimensional Silica*. Phys. Rev. Lett. **109**, 106101 (2012).
3. **L. Lichtenstein**, M. Heyde, S. Ulrich, N. Nilius and H.-J. Freund. *Probing the properties of metal-oxide interfaces: silica films on Mo and Ru supports*. J. Phys. Condens. Matter **24**, 354010 (2012).
4. B. Yang, W. E. Kaden, X. Yu, J. A. Boscoboinik, Y. Martynova, **L. Lichtenstein**, M. Heyde, M. Sterrer, R. Włodarczyk, M. Sierka, J. Sauer, S. Shaikhutdinov and H.-J. Freund. *Thin silica films on Ru(0001): monolayer, bilayer and three-dimensional networks of SiO<sub>4</sub> tetrahedra*. Phys. Chem. Chem. Phys. **14**, 11344 (2012).
5. **L. Lichtenstein**, C. Büchner, S. Stuckenholtz, M. Heyde and H.-J. Freund. *Enhanced atomic corrugation in dynamic force microscopy—The role of repulsive forces*. Appl. Phys. Lett. **100**, 123105 (2012).
6. **L. Lichtenstein**, C. Büchner, B. Yang, S. Shaikhutdinov, M. Heyde, M. Sierka, R. Włodarczyk, J. Sauer and H.-J. Freund. *The Atomic Structure of a Metal-Supported Vitreous Thin Silica Film*. Angew. Chem. Int. Ed. **51**, 404 (2012).
7. G. H. Simon, T. König, L. Heinke, **L. Lichtenstein**, M. Heyde and H.-J. Freund. *Atomic structure of surface defects in alumina studied by dynamic force microscopy: strain-relief-, translation- and reflection-related boundaries, including their junctions*. New J. Phys. **13**, 123028 (2011).

8. T. König, G. H. Simon, L. Heinke, **L. Lichtenstein** and M. Heyde. *Defects in oxide surfaces studied by atomic force and scanning tunneling microscopy*. Beilstein J. Nanotechnol. **2**, 1 (2011).
9. D. Löffler, J. J. Uhlrich, M. Baron, B. Yang, X. Yu, **L. Lichtenstein**, L. Heinke, C. Büchner, M. Heyde, S. Shaikhutdinov, H.-J. Freund, R. Włodarczyk, M. Sierka and J. Sauer. *Growth and Structure of Crystalline Silica Sheet on Ru(0001)*. Phys. Rev. Lett. **105**, 146104 (2010).
10. L. Heinke, **L. Lichtenstein**, G. H. Simon, T. König, M. Heyde and H.-J. Freund. *Structure and electronic properties of step edges in the aluminum oxide film on NiAl(110)*. Phys. Rev. B **82**, 075430 (2010).
11. L. Heinke, **L. Lichtenstein**, G. H. Simon, T. König, M. Heyde and H.-J. Freund. *Local Work Function Differences at Line Defects in Aluminium Oxide on NiAl(110)*. ChemPhysChem **11**, 2085 (2010).

# Danksagung

Mein besonderer Dank gilt Professor Dr. Hans-Joachim Freund für ein herausragendes Forschungsprojekt sowie zahlreiche wissenschaftliche Diskussionen, für ausgezeichnete Arbeitsbedingungen, für ein fruchtbares multikulturelles Umfeld, und für die Möglichkeit, meine Ergebnisse auf internationalen Konferenzen vorstellen zu können.

Bei Professor Dr. Paul Fumagalli möchte ich mich ganz herzlich für die Betreuung meiner Dissertation, für die Möglichkeit, meine Ergebnisse im Rahmen von Seminarvorträgen präsentieren zu können, sowie für sehr konstruktive Anregungen und Diskussionen bedanken.

Dr. Markus Heyde bin ich zutiefst dankbar für die engagierte Unterstützung meiner Arbeit, für sehr gute Ideen bezüglich der Messung und Auswertung, für das tolle Arbeitsklima in seiner Arbeitsgruppe, sowie für eine Messapparatur auf höchstem internationalen Niveau.

Mein weiterer Dank gilt Gero Thielsch, Christin Büchner, Stefanie Stuckenholz, Dr. Lars Heinke, Dr. Thomas König und Dr. Georg Simon für hilfreiche und interessante Diskussionen, technische Unterstützung und eine freundliche und produktive Atmosphäre.

Bei Professor Dr. Joachim Sauer, Professor Dr. Marek Sierka, und Radosław Włodarczyk bedanke ich mich sehr herzlich für die theoretische Unterstützung des Forschungsprojekts sowie für lehrreiche und interessante Diskussionen.

Ebenfalls gilt mein Dank allen Arbeitsgruppen der Abteilung Chemische Physik des Fritz-Haber-Instituts, die an dem Silikapjekt beteiligt waren. Nur durch diese Synergie konnten maßgebliche Fortschritte erzielt werden.

Ganz herzlich bedanken möchte ich mich bei allen bisher nicht erwähnten

Mitgliedern der Abteilung Chemische Physik des Fritz-Haber-Instituts für das nette Arbeitsklima und ein freundschaftliches Umfeld.

Zu guter Letzt möchte ich mich bei meinen Eltern Irina und Alexander Lichtenstein, meinen Großeltern Adelia Lichtenstein, Ivetta Goldina und Rodion Goldin, meiner Schwester Ekaterina Koch-Lichtenstein und meiner Ehefrau Christine Lichtenstein für die moralische Unterstützung während der gesamten Dissertationsperiode bedanken. Ihr wart alle eine sehr große Hilfe für mich.

# Selbständigkeitserklärung

Hiermit erkläre ich, dass ich die vorliegende Arbeit selbständig und nur unter Verwendung der angegebenen Quellen und Hilfsmittel angefertigt habe.

Berlin, den 09. Oktober 2012

Leonid Lichtenstein